2009

Improved seismic isolation for the Laser Interferometer Gravitational Wave Observatory with hydraulic external pre-isolator system

Shyang Wen
Louisiana State University and Agricultural and Mechanical College

IMPROVED SEISMIC ISOLATION FOR THE LASER INTERFEROMETER GRAVITATIONAL WAVE OBSERVATORY WITH HYDRAULIC EXTERNAL PRE-ISOLATOR SYSTEM

A Dissertation

Submitted to the Graduate Faculty of the
Louisiana State University and
Agricultural and Mechanical College
in partial fulfillment of the
requirements for the degree of
Doctor of Philosophy

in

The Department of Physics and Astronomy

by
Shyang Wen
B.S., National Taiwan University, 1998
May, 2009

ACKNOWLEDGEMENTS

I would like to thank all people involved in the LIGO experiment in the past and at present. Without them writing this thesis would not have been possible.

TABLE OF CONTENTS

ABSTRACT

LIGO hosts the world's most sensitive GW detectors capable of detecting strain of $h=10^{-22}/\sqrt{Hz}$ at 100-200Hz. To maximize the amount of useful scientific results LIGO generates, it is necessary to operate the instrument uninterruptedly. However, for ground-based detectors, this is not possible without isolating it from the environmental disturbances, which in most cases is predominated by seismic noise. We examined the recent seismic noise records at LLO and LHO, and found the seismic noise at both sites had decreased from Oct. 1, 2003 to Oct. 1, 2006. No long term trend can be derived from the there-year data studied, however it is clear that the LLO seismic environment has been consistently noisier than that of LHO, from 0.1 to 3Hz, by a factor of 2.4 to 9.0. To cope with noisier ground conditions at LLO, an additional stage of seismic isolation system external to the LLO vacuum tanks was developed. The system is called the Hydraulic External Pre-Isolator (HEPI), which uses position and geophone sensors, ground seismometers, and hydraulic actuators to suppress payload motion. HEPI prototype was designed and tested in 2003 and installed on site in 2004. The first stage of HEPI commissioning was finished by the LLO's fifth science run (S5). The design, control strategy, performance, as well as the problems of the HEPI system at LLO are described in Chapter 3. Based on the isolation HEPI provided, we were able to achieve an operational duty factor of 66.7% and maximum detection range of 15.8Mpc for 1.4 binary neutron star inspiral at LLO in S5. While the current HEPI configuration is stable, it is by no means finalized. Several possible improvements to HEPI are introduced in Chapter 5. These enhancements require minimal to moderate addition and iteration to existing hardware and software, and should improve the isolation performance and stability of the HEPI system.

CHAPTER 1: INTRODUCTION

1.1 Gravitational Wave

One of the predictions of general relativity is the curvature of space-time due to the presence of mass-energy, and the existence of gravitational waves (GW) due to time-varying mass-energy distribution. As a result of conservation of mass-energy, momentum, and angular momentum, a minimum of non-static quadruple mass-energy distribution is required to generate gravitational waves. While the space-time distortion can be complex near the radiating source, sufficiently far away from the source the space time can be described by small perturbations to a flat Minkowski space-time,

$$g_{\mu\nu} = \eta_{\mu\nu} + h_{\mu\nu},\ |h_{\mu\nu}| << 1.$$

Assuming the wave propagates in the Z direction and with proper choice of gauge conditions, the solution of $h_{\mu\nu}$ is in the form of,

$$h_{\mu\nu} = \begin{pmatrix} 0 & 0 & 0 & 0 \\ 0 & -h_{+} & h_{\times} & 0 \\ 0 & h_{\times} & h_{+} & 0 \\ 0 & 0 & 0 & 0 \end{pmatrix} \cos(k_z z - \omega t),$$

and has two independent polarizations h_{+} and $h_{\times}$ [1].

Suppose a simple Michelson interferometer (see Figure 1.1, but with ITMX, ITMY, and RM removed) is used to detect the h_{+} polarized gravitational wave, light traveling from the beam splitter to the X end mirror follows the geodesic,

$$ds^2 = -c^2dt^2 + (1 - h_{+}\cos(k_z z - \omega t))dx^2 = 0.$$

Assume the distance between the X end mirror and the beam splitter is L, the time elapsed during this journey is,

$$\Delta t_x = \int_0^L dt = \int_0^L \frac{1}{c}(1 + h_{+}\cos(k_z z - \omega t))^{1/2} dx \sim \frac{L}{c}\left(1 + \frac{h_{+}}{2}\cos(\omega t)\right).$$

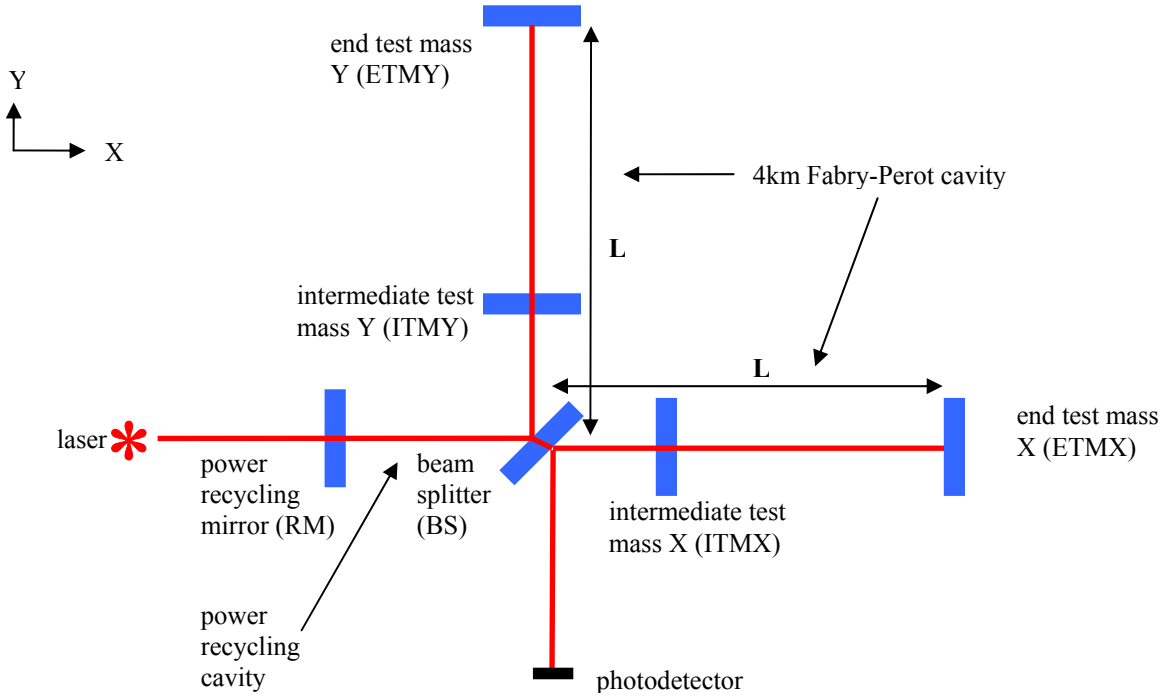

Figure 1.1. Schematic diagram of LIGO

The last approximation is based on the assumption that the period of the gravitational wave, $2\pi/\omega$, is much larger than the total travel time Δt. One can derive similar equation for light traveling towards the Y end mirror,

$$\Delta t_y \sim \frac{L}{c}\left(1-\frac{h_+}{2}\cos(\omega t)\right).$$

After returning from the end mirrors and arriving at the photodetector, the two light beams will have a phase difference of $2Lh_+\cos(\omega t)(2\pi f)$, where f is the frequency of the laser, and hence produced an interference pattern. They will also have traveled different distances and the difference being $2Lh_+\cos(\omega t)$. It is customary to divide this quantity by the total distance traveled by each beam, 2L, to define the strain, $h_+\cos(\omega t)$.

To an observer at a distance of r from the source, the strength of h produced by an equal mass (M) binary system with separation R is,

$$h \sim \left(\frac{2MG}{c^2}\right)^2\left(\frac{1}{rR}\right).$$

One of the reasons gravitational wave has not been directly observed is the miniscule (G^2/c^4) factor. To produce any measurable effect one needs a source with huge mass at close distance, or a very long interferometer arm L. Massive and compact celestial systems are ideal candidates for producing measurable h on earth. With the technological advances in the last few decades, direct measurement is now feasible.

1.2 Laser Interferometer Gravitational Wave Observatory

The Laser Interferometer Gravitational wave Observatory (LIGO) hosts three of the seven Michelson interferometric GW detectors around the world. Two (4km and 2km arm length) are located in Hanford, Washington (LHO) and one (4km arm length) in Livingston, Louisiana (LLO). The two 4km detectors are also the world's most sensitive GW detectors. The two sites are separated by a distance of approximately 3000km, which allows us to reject false local detection events originating from local disturbances, and constrain the direction of the source once coincidental detection of GW is found at two or more sites.

The initial LIGO is designed with GW sensitivity of $h_{rms}=10^{-21}$ integrated over the ~100-200Hz minimum noise region, for continuous day and night time operation. To achieve this, several modifications to a simple Michelson interferometer are necessary. Two intermediate test masses, which are partially transmissive mirrors, are placed between the beam splitter and the end test masses. The surfaces of the intermediate and end test masses facing each other are slight spherical concaved surfaces, and the cavities in-between form two 4km Fabry-Perot cavities. Light entering the cavities is briefly stored in the cavities as it reflects back and forth approximately 100 times before exiting the cavities, thus increases the effective distance the light travels and the differential phase of the two light beams interfering at the photodetector. The positions of the mirrors are controlled in a way such that in the absence of GW, the two light beams coming back from the intermediate test masses interfere constructively in the direction

going back to the laser, and destructively in the direction towards the photodetector. If GW is present, any differential phase change the light picks up in the two arms allows a small amount of light to travel towards the photodetector where the interference is turned into GW signal. A power recycling mirror is placed between the beam splitter and the laser. The light going back in the direction of the laser is reflected back into the interferometer by this mirror and constructively interferes with the laser light. This increases the effective input power, lowers the photon shot noise and improves the sensitivity of the interferometer (Figure 1.1). The interferometer is said to be 'locked' when the alignment and position of the mirrors are controlled well enough to achieve the above state.

For ground-based GW detectors the largest disturbance comes from seismic noise. The main optics and large part of the input support optics of LIGO are suspended in vacuum by pendulums and cascaded stages of mass-spring stacks that provide passive isolation [2, 3, 4]. At the pendulum level, the motion of each suspended optic is sensed and damped by optical shadow sensors and electromagnetic actuators. The main interferometer optics also assisted by optical levers for additional angular motion sensing and damping.

Small fraction of the interferometer light is extracted from a number of places, directed to auxiliary photodetectors, and is used for various cavity lengths and optics angular alignment sensing and control. The electromagnetic actuators mentioned above also serve as servos for these controls.

1.3 LLO Duty Cycle Problem

The LIGO Livingston (LLO) facility was built near to the Gulf of Mexico, logging industries, and town of Livingston. Oceanic and human activities periodically and aperiodically provide large ground disturbances at the observatory at the 0.1 to 0.35 Hz and the 1 to 3 Hz bands, respectively [5]. While these frequency bands do not lie in LIGO's GW detection band, they are

found to affect the instrument's operational time (or duty cycle). The initial passive seismic isolation design does not provide isolation below the lowest stack and suspension resonant frequencies, which lies between 0.5-3Hz. During commissioning of LIGO, it became evident that the limited control loop gain of various interferometer cavity lengths and optics alignment control system were not sufficient to compensate excessive input optics and test mass motion during periods of elevated seismic activities. Also the electromagnetic actuators for the suspended optics have 1mm dynamic range which was insufficient to maintain constant interferometer resonant cavities length on the time scale of few hours at a time. An active seismic isolation system was necessary for uninterrupted operation of the observatory.

The Hydraulic External Pre-Isolator (HEPI) was developed for this purpose, first by collaborators of LIGO at Stanford University [6], and later tested at Massachusetts Institute of Technology [7]. HEPI is able to provide seismic isolation from 0.1Hz to roughly 10Hz. It was installed at LLO site following the end of the third science run, S3[1], and incorporated into the instrument's normal operation since the fourth science run, S4[2]. For S3 the instrument's duty cycle was 21.8%, after the installation of HEPI we achieved duty cycle of 74.5% for S4, and 66.7% for S5[3].

1.4 S5 LLO Sensitivity Level

The actual LIGO is far from being the simple Michelson interferometer shown in Figure 1.1, and is never perfectly isolated from environmental disturbances. Beside the noise sources associated with its intrinsic design, its own supporting mechanical structure, optical components, sensors and actuators, laser, electronics, etc., all contribute noise to the gravitation wave signal though various coupling mechanism. The core of LIGO commissioning activities is essentially

[1] S3 run: Oct. 31, 2003 at 10:00 CST to Jan. 9, 2004 at 10:00 CST
[2] S4 run: Feb. 22, 2005 at 12:00 CST to Mar. 23, 2005 at 24:00 CST
[3] S5 run: Nov. 15, 2005 at 12:00 CST to Sep. 30, 2007 at 19:00 CST

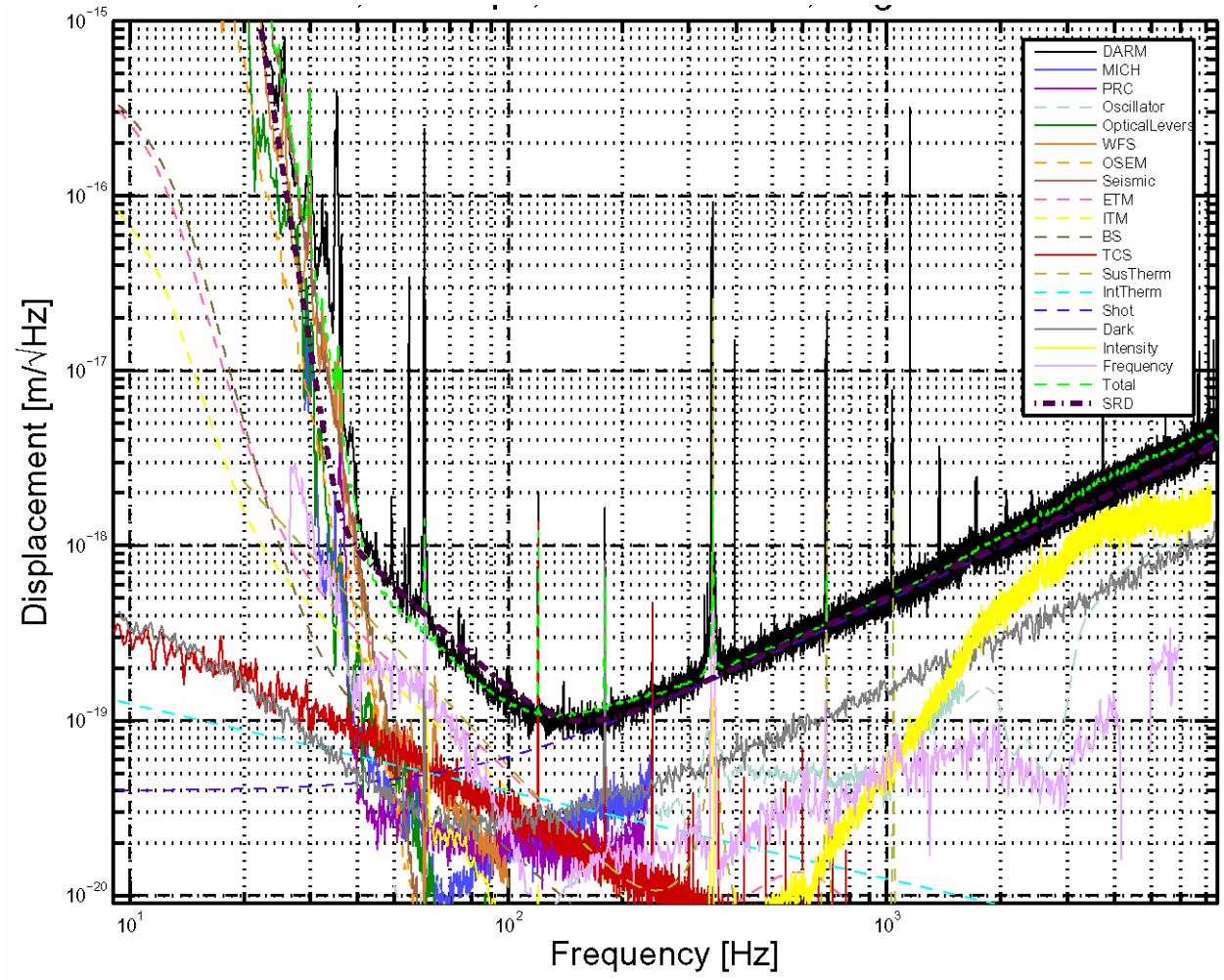

Figure 1.2. Best LLO performance during S5, occurred roughly at Aug 29 2007 09:31 UTC, with detection range of 15.8Mpc for 1.4 solar mass binary neutron star inspiral. Plot is extracted from LIGO Project S5 archive webpage.

identifying and suppressing these noise sources. Figure 1.2 shows the best noise level (or sensitivity) of the LLO during S5, in terms of displacement noise density. The line marked "SRD" is the designed sensitivity for initial LIGO, while the line marked "DARM" is the actual measured sensitivity of the interferometer. Also shown in Figure 1.2 are the main noisecontributors, which includes the noise of the servo controlling the intermediate test masses (MICH) and the power recycling cavity (PRC), local oscillator noise (Oscillator), optical lever noise (OpticalLevers), noise of local damping sensors of the optics (OSEM), noise of the wave

front sensors controlling the angle of the optics (WFS), seismic noise (Seismic), actuator noise of end test masses, intermediate test masses and beam splitter (ETM, ITM and BS), noise from the thermal compensation system (TCS) for the intermediate test masses, noise from thermally excited motion of the test mass suspension wires (SusTherm) and internal resonant modes the of the test masses (IntTherm), shot noise (Shot), noise of the main detection electronics chain (Dark), intensity (Intensity) and frequency (Frequency) noise of the laser, and root sum square of all of the noise (Total).

The measured sensitivity above 200 Hz is at the designed level, and the noise is dominated by photon shot noise which is fairly well understood. Between 50 and 100 Hz the sensitivity is slightly above the designed level. Since this band is of great importance to some astronomical source, such as binary black hole coalescence, it is crucial to understand the noise source so it is possible to lower the total noise in future LIGO upgrades. Theoretical and experimental work is currently underway to explain the excess noise. Below 40Hz the noise is the least understood. The total noise is well above the designed curve and seismic noise is believed to be the main contributor. When the interferometer is operating at the designed sensitivity at around 100-200Hz, it is said to enter 'science mode'.

1.5 Astronomical Sources

There are several types of astronomical sources that are of interest to LIGO community: periodic, binary inspiral, bursts, and stochastic. Periodic sources, such as massive compact binary systems long before they are in the merger state, and non-symmetric pulsars, changes their frequency and amplitude relatively slowly. Binary inspiral sources refer to compact binary systems just before the merger state; examples are binary neutron stars and binary black holes coalescence. Bursts sources include non-symmetric collapse of supernovae, merging sate of binary systems, and other mechanisms of unknown nature. Stochastic source originates from the

cosmological background that has evolved from early phase of the universe: big bang, inflation, transition, etc. It can also be a collection of large number of point sources of the three previously described types that are too distant to be resolved individually.

Data obtained in the past five science runs has been analyzed by LIGO research groups to look for these signals. Two of the science runs, S4 and S5, was aided by HEPI, and data quality was improved compared to previous runs. No GW detection has been claimed yet, however, upper limits for various sources have been set. Discoveries from S4 and S5 are extracted below.

In a targeted search of periodic GW sources from 78 known radio pulsars, strain upper limit of 2.6×10^{-25} for PSRJ1603-7202 and ellipticity of 10^{-6} for PSRJ2124-3358 were determined with 95% confidence level from S3 and S4 data [8]. A non-targeted all-sky search was conducted using S4 data, for periodic gravitational waves in the frequency range 50-1000Hz and with the frequency's time derivative in the range -10^{-8} Hz/s to zero. The upper limit on the gravitational wave strain amplitude for simulated sources distributed isotropically across the sky and with isotropically distributed spin-axes, is 4.23×10^{-24} near 140 Hz with 95% confidence level [9]. The search was also conducted using the first eight month of S5 data in the same frequency range, and with the frequency's time derivative in the range -5×10^{-9} Hz/s to zero. Strain amplitude was derived to be 1×10^{-24} over a 200Hz band with 95% confidence level [10].

Upper limits for compact binary inspiral event rates were derived from S3 and S4 data to be $4.9/\mathrm{yr}/L_{10}$ for primordial black hole binaries in the mass range of 0.35 to 1 solar masses, $1.2/\mathrm{yr}/L_{10}$ for neutron star binaries in the range of 1 to 3 solar masses, and $0.5/\mathrm{yr}/L_{10}$ for stellar black hole binaries in the range of 3 to 80 solar masses with 90% confidence level, where L_{10} is 10^{10} times the blue luminosity of the Sun [11]. From the first year of S5 data, upper limits for neutron star, black hole, and black hole-neutron star binaries with Gaussian mass distributions were derived to be $3.8\times10^{-2}/\mathrm{yr}/L_{10}$, $2.2\times10^{-3}/\mathrm{yr}/L_{10}$, and $1.6\times10^{-2}/\mathrm{yr}/L_{10}$, respectively, with 90%

confidence level. These limits assume that the Gaussian distributions are 1.35 solar mass pairs with 0.04 solar mass standard deviation for neutron star binaries, 5 solar mass pairs with 1 solar mass standard deviation for black hole binaries, and (5, 1.35) solar mass pairs with (1, 0.04) solar mass standard deviation for black hole-neutron star binaries [12].

A search for short-duration gravitational wave bursts with arbitrary waveform in the 64-1600Hz band was conducted using S4 data from all three LIGO interferometers. For sources with large enough amplitudes to be detected reliably, a burst rate upper limit of 0.15 per day was established at 90% confidence level. The distances at which representative supernova and binary black hole merger signals could be detected with 50% efficiency was also estimated in this analysis [13].

An amplitude upper limit of $\Omega_{GW} < 6.5 \times 10^{-5}$ was placed on the stochastic gravitational waves using S4 data, assuming a frequency independent spectrum in the most sensitive frequency range 51–150Hz [14]. Ω_{GW} is the energy density spectrum of GW normalized by the critical energy density of the universe.

All-sky strain upper limit maps for two sources of different strain power spectrum models were generated with 90% confidence level using S4 data. For an f^{-3} power law, the upper limits is between 1.2×10^{-48} $Hz^{-1}(100Hz/f)^3$ and $1.2\times10^{-47}Hz^{-1}(100Hz/f)^3$ from 50Hz to 1.8 kHz, depending on the position in the sky. For constant strain power spectrum, the upper limit is between 8.5×10^{-49}/Hz and 6.1×10^{-48}/Hz [15].

1.6 Contribution of This Thesis

There are two levels of contributions to the LIGO community from the work described in the thesis.

The first level is more technical, which is the successful implementation of HEPI control methods and characterization of its isolation performance at LLO. Although some of the control

methods were originally developed and tested for the full-scale HEPI prototype at MIT, it did not deliver the same level of isolation as the current HEPI installed at LLO. Current HEPI performance was realized only after some intensive refinement was done to its control methods just before S5. It is proven to provide up to factor of 10 seismic noise reduction at the optics table in the 0.1-3Hz band. In some cases a factor of few 10s are reported, especially in the Z direction. The content in Chapter 3 encompasses what was done to bring HEPI to its current performance level.

This achievement of this technology is also of some importance to the general science community. While commercially available isolation products are abundant, seldom do they achieve isolation below 1Hz, and rarely do they achieve isolation down to 0.1Hz. Of those who claim to achieve isolation below 1Hz, the performance is often limited as their natural frequency lies just below 1Hz. Being an active isolation system, HEPI easily surpasses them in this regard. In principle, the current HEPI design is able to isolate the ground motion below 0.1Hz once the ground tilting and sensor noise is removed from the feed-forward part of the system (see Chapters 3 and 5).

The second level, which is directly related to the first and also one of the goals of installing HEPI, is to increase the LLO duty cycle. Before the installation of HEPI at LLO, attempting to lock the interferometer during the day time was a constant challenge, as large disturbance from the town of Livingston would easily destroy the alignment of the suspended optics. To compensate the large range of ground travel at low frequency, many of the servos loop that control the position and alignment of the optics and various interferometer cavity lengths are often less optimized, as one or more of their control parameters such as sensitivity, loop gain, and dynamic range must be compromised. After the large disturbance was over, depending on

the remaining seismic noise level, often half to few hours was required for the interferometer to go through the entire locking process and finally re-operate at the designed sensitivity level.

After the installation of HEPI, the constraints were less stringent on these controls. The interferometer was able to maintain lock even with relatively large disturbance near by, at the expense of lowering the interferometer sensitivity by roughly two orders of magnitude. An example is the daily cargo trains passing through downtown Livingston, which have always been the largest ground disturbance in the 1-10Hz band. After the train passes the interferometer could re-operate at the designed sensitivity level in a relatively short period of time. This capability was further assisted by the resonant gain filters described in Section 3.2.2 that reduces 1-3Hz band rms motion furthermore at the optics table.

Reduction in the mount of time the interferometer spends in acquiring lock increases the total amount of time LLO operates at the designed sensitivity level. It also increases the chance LLO and the other two interferometers at LHO operate at the designed sensitivity level simultaneously (triple-coincident). One of the goals of S5 was to gather one year's worth of triple-coincident data with an effective range of 10Mpc or better for the 4km interferometers, and 5Mpc or better for the 2km interferometer. The increase in duty cycle by a factor of 3 allowed us to achieve this in ~23 months instead of ~70 months, which was a dramatic improvement.

CHAPTER 2: A THREE-YEAR SEISMIC NOISE STUDY AT THE TWO LIGO SITES

The motivation of building the HEPI system was partially based on the pioneering local seismic environment studies by E. Daw et al. [5], which spanned 613 days from April 2, 2001 to December 10, 2002. In their study, the seismic noise level at LLO was at least few times higher than that of LHO in the 0.1-3Hz band. By the end of 2006, which was roughly half-way into S5 run, the LLO duty cycle was 60.4%. There was rising concern within the LIGO community about whether the seismic noise at LLO was increasing and whether HEPI would be effective enough to suppress it. Furthermore, if there had been an increase in the seismic noise, whether a redesign of the external seismic isolator would be necessary for the Advanced LIGO (AdLIGO) project. Such doubts originated from visible nearby logging activities and Livingston town development that occurred during HEPI commissioning and its first year of operation, and also from the large microseism motions seen during hurricane seasons.

In this new study we investigated the seismic noise data from Oct. 1, 2003 to Oct. 1, 2006 at both sites. We showed that on yearly averages, the seismic noise level at LHO in the 0.1~1Hz bands had been fairly stable, and had decreased in the 1-30Hz bands. Contrary to speculation, the seismic noise level at LLO decreased in the 0.03~3Hz band, most noticeable in the 0.1-1Hz microseism bands from the first to the second year. Nearby logging activities and traffic might have been attention-catching but the percentage of time they occupied probably was small or did not change large enough to impact the overall seismic noise profile. Comparing with Daw's results, we found the ground velocity percentile profiles for both sites remained largely unchanged, and many of his interesting findings remain true. No definite long term trend can be safely derived from the limited there-year data studied; however, it is clear that the LLO seismic environment has been consistently noisier than that of LHO. Given the known isolation performance provided by HEPI (described in Chapter 3), the importance of this study is to

Table 2.1.DMT data channels.

	LLO STS-2	LLO Guralp	LHO Guralp
Station	Corner, EX, EY	Corner, EX, EY	Corner, EX, EY, MX, MY
Direction	X, Y	X, Y, Z	X, Y, Z
Band	0.03~0.1Hz 0.1~0.2Hz 0.2~0.35Hz 0.35~1Hz 1~3Hz	0.1~0.3Hz 0.3~1Hz 1~3Hz 3~10Hz 10~30Hz	0.1~0.3Hz 0.3~1Hz 1~3Hz 3~10Hz 10~30Hz

understand the ground condition under which HEPI is able to assist LLO in achieving the S5 duty cycle. The result also serves as reference point for longer seismic noise trend study in the future. Should the seismic environment at LLO becomes noisier in the long run, an upgrade to the existing HEPI system may be necessary.

STS-2 [16] and Guralp [17] seismometers were used in this study. STS-2 and Guralp seismometers were installed in each one of the three LLO stations, and Guralp seismometers were installed in each one of the five LHO stations. All seismometers were placed on the concrete floor, adjacent to the beam tubes. The STS-2 and Guralp seismometers in each LLO station were within one meter from each another. Station interiors were temperature-controlled, so thermal fluctuation in the seismometers was limited. Both types of seismometers measure velocity and deliver data in X, Y, and Z directions. Raw data recorded from the seismometers was processed into band-limited minute-rms data by the seismic division of LIGO real-time Data Monitoring Tool (DMT) [18, 19]. Table 2.1 lists the data generated by DMT. The precise time periods inspected are,

LLO STS-2: Oct. 1, 2004~Oct. 1, 2006 (GPS time 780624013 to 843696014).

LLO Guralp: Oct. 1, 2003~Oct. 1, 2006 (GPS time 749001613 to 843696014).

LHO Guralp: Oct. 1, 2003~Oct. 1, 2006 (GPS time 749001613 to 843696014).

Band-limited minute-rms data from these time periods was then used to construct yearly ground velocity percentile profiles.

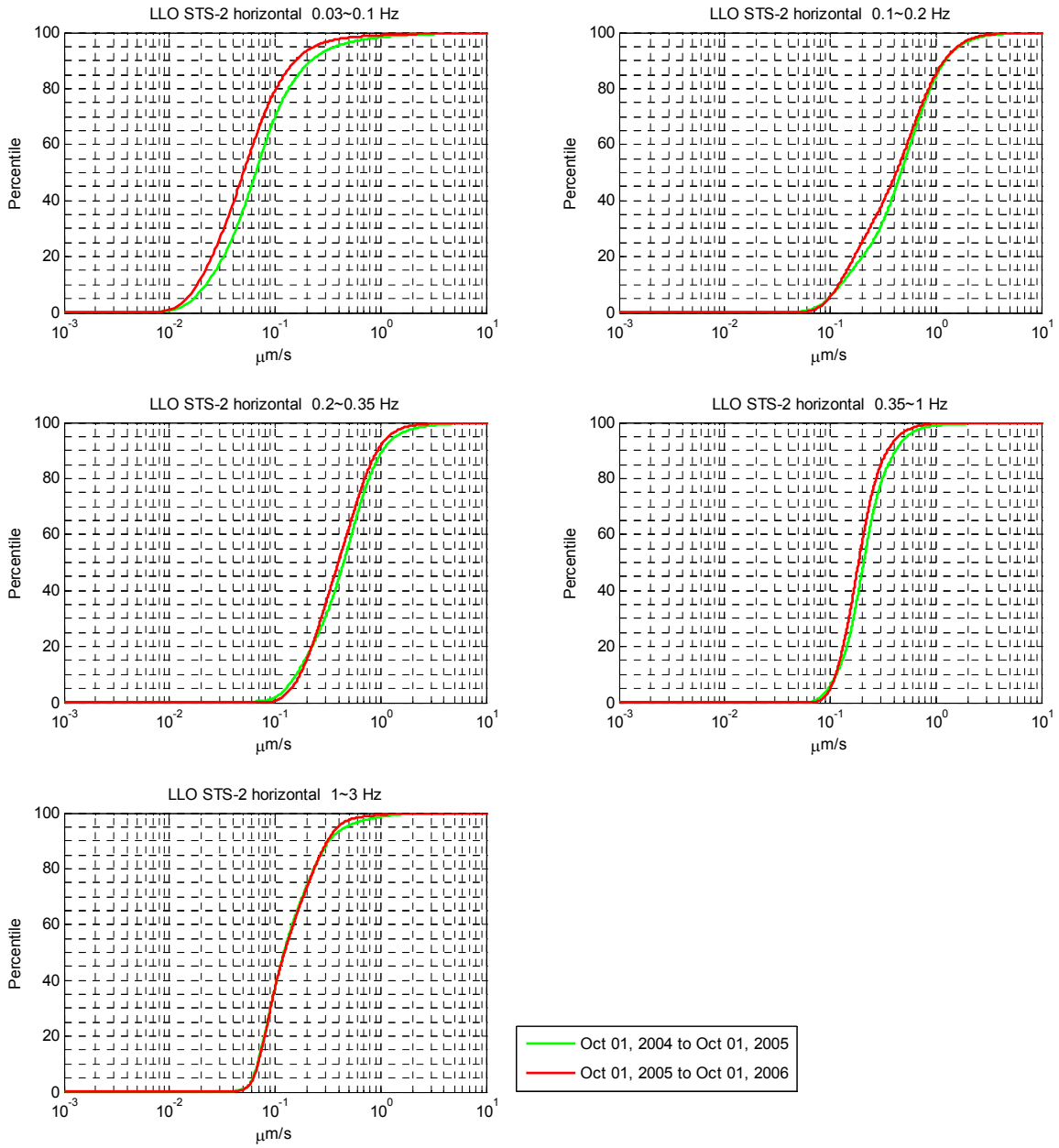

Figure 2.1. Mean (average over all stations) horizontal rms-velocity percentile profile in each year and band, measured by LLO STS-2 seismometers.

The result of our study is presented below. This study is strictly not a controlled experiment. Detailed description of how the data was acquired and processed, and obvious data quality issues, is in appendix A.

Table 2.2. Mean rms-velocity percentile values in each year and band.

LLO STS-2, horizontal direction					
Band	Time span	Velocity percentile (μm/s)			
		50%	75%	90%	95%
0.03~0.1Hz	Oct 1 2004 to Oct 1 2005	0.07	0.12	0.22	0.38
	Oct 1 2005 to Oct 1 2006	0.05	0.09	0.16	0.24
0.1~0.2Hz	Oct 1 2004 to Oct 1 2005	0.47	0.79	1.23	1.67
	Oct 1 2005 to Oct 1 2006	0.42	0.75	1.21	1.62
0.2~0.35Hz	Oct 1 2004 to Oct 1 2005	0.45	0.70	1.05	1.40
	Oct 1 2005 to Oct 1 2006	0.40	0.64	0.94	1.20
0.35~1Hz	Oct 1 2004 to Oct 1 2005	0.21	0.29	0.42	0.54
	Oct 1 2005 to Oct 1 2006	0.19	0.25	0.35	0.44
1~3Hz	Oct 1 2004 to Oct 1 2005	0.12	0.21	0.33	0.48
	Oct 1 2005 to Oct 1 2006	0.12	0.21	0.31	0.40

Table 2.3. Noisiest channel in each band from Oct. 1, 2004 to Oct. 1, 2006.

LLO STS-2, horizontal direction					
Band	Noisiest channel	Velocity percentile (μm/s)			
		50%	75%	90%	95%
0.03~0.1Hz	L1:DMT-BRMS_SEI_LVEA_STS-2_X	0.06	0.11	0.20	0.32
0.1~0.2Hz	L1:DMT-BRMS_SEI_LVEA_STS-2_Y	0.45	0.79	1.25	1.68
0.2~0.35Hz	L1:DMT-BRMS_SEI_LVEA_STS-2_X	0.43	0.69	1.02	1.33
0.35~1Hz	L1:DMT-BRMS_SEI_EY_STS-2_Y	0.22	0.30	0.42	0.54
1~3Hz	L1:DMT-BRMS_SEI_EY_STS-2_Y	0.16	0.29	0.43	0.60

2.1 LLO

The LLO seismic environment became quieter from Oct. 1, 2004 to Oct. 1, 2006, according to the data measured by all the STS-2 seismometer channels. See Figure 2.1. The data are summarized in Table 2.2, which lists the mean (average over all stations) rms-velocity percentile values in each year and band. Table 2.3 lists the noisiest channel in each band averaged over two years, as well as its recorded rms-velocity percentile values. The noisiest channel is selected if all four of its rms-velocity percentile values are the greatest among all channels.

The data measured by the Guralp seismometers suggests that the LLO seismic environment had become quieter from 0.1-3Hz, from Oct. 1, 2003 to Oct. 1, 2006, see Figure 2.2. Table 2.4 and 2.5 list the mean rms-velocity percentile values of horizontal signals in each year and band, and the mean (average over all stations) rms-velocity percentile values of horizontal signals in

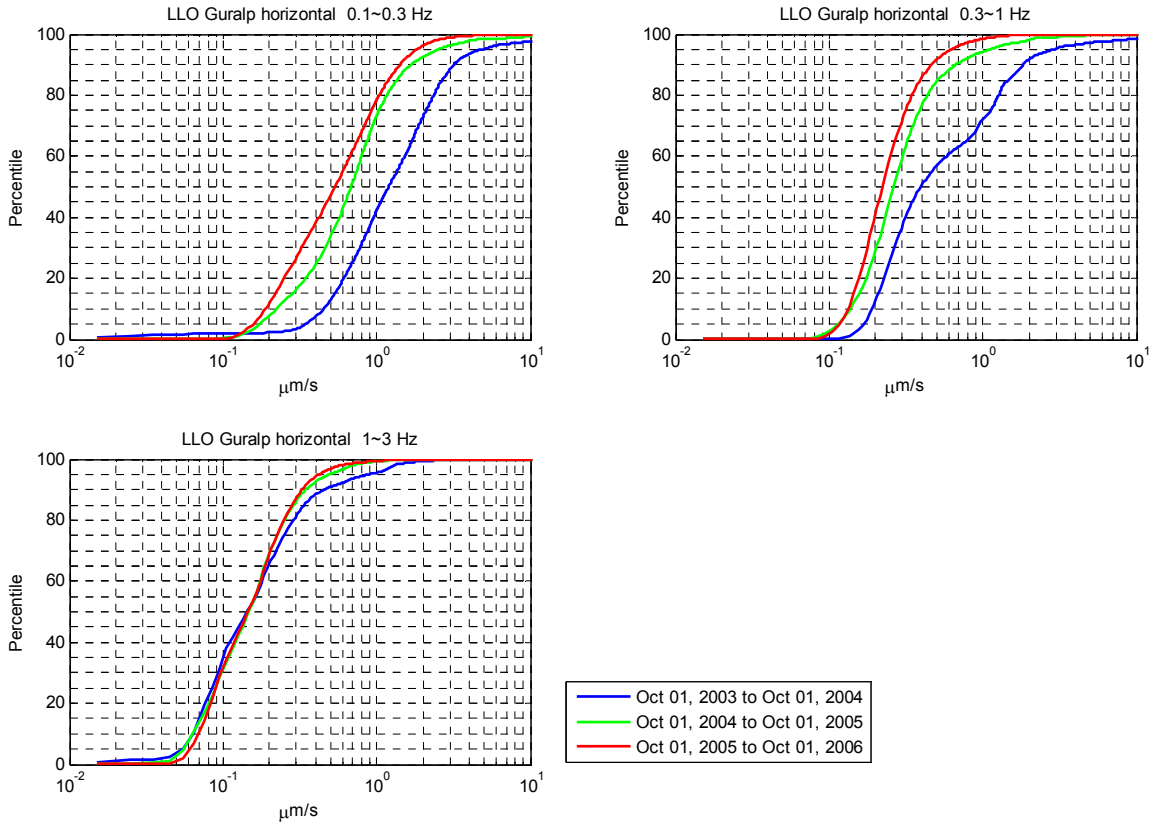

Figure 2.2. Mean horizontal rms-velocity percentile profile in each year and band, measured by LLO Guralp seismometers.

Table 2.4. Mean rms-velocity percentile values in each year and band.

LLO Guralp, horizontal direction					
Band	Time span	Velocity percentile (μm/s)			
		50%	75%	90%	95%
0.1~0.3Hz	Oct 1 2003 to Oct 1 2004	1.19	2.11	3.19	4.90
	Oct 1 2004 to Oct 1 2005	0.69	1.05	1.68	2.54
	Oct 1 2005 to Oct 1 2006	0.55	0.94	1.42	1.85
0.3~1Hz	Oct 1 2003 to Oct 1 2004	0.41	1.14	1.84	2.92
	Oct 1 2004 to Oct 1 2005	0.27	0.40	0.68	1.14
	Oct 1 2005 to Oct 1 2006	0.22	0.32	0.47	0.63
1~3Hz	Oct 1 2003 to Oct 1 2004	0.15	0.26	0.46	0.90
	Oct 1 2004 to Oct 1 2005	0.16	0.24	0.36	0.50
	Oct 1 2005 to Oct 1 2006	0.15	0.22	0.34	0.43

each band averaged over three years, respectively, and Table 2.7 and 2.8 list those of vertical signals. Over the course of three years, the rms-velocity values had decreased more than a factor of 2 at the 50th, 75th, 90th, and 95th percentile in the 0.1-0.3Hz band, and had decreased more than a factor of 3.5 at the 75th, 90th, and 95th percentile in the 0.3-1Hz band, in both horizontal

Table 2.5. LLO seismic noise level. Mean rms-velocity percentile values in each band, from Oct. 1, 2003 to Oct. 1, 2006.

LLO Guralp, horizontal direction				
Band	Velocity percentile (μm/s)			
	50%	75%	90%	95%
0.1~0.3Hz	0.73	1.24	2.19	2.98
0.3~1Hz	0.28	0.44	1.07	1.58
1~3Hz	0.16	0.24	0.37	0.54

Table 2.6. Noisiest channel in each band, from Oct. 1, 2003 to Oct. 1, 2006.

LLO Guralp, horizontal direction					
Band	Noisiest channel	Velocity percentile (μm/s)			
		50%	75%	90%	95%
0.1~0.3Hz	L0:PEM-EY_SEISX	0.75	1.36	3.55	9.76
0.3~1Hz	L0:PEM-EY_SEISX	0.31	0.51	1.76	5.56
1~3Hz	L0:PEM-EY_SEISX	0.19	0.35	0.67	1.06

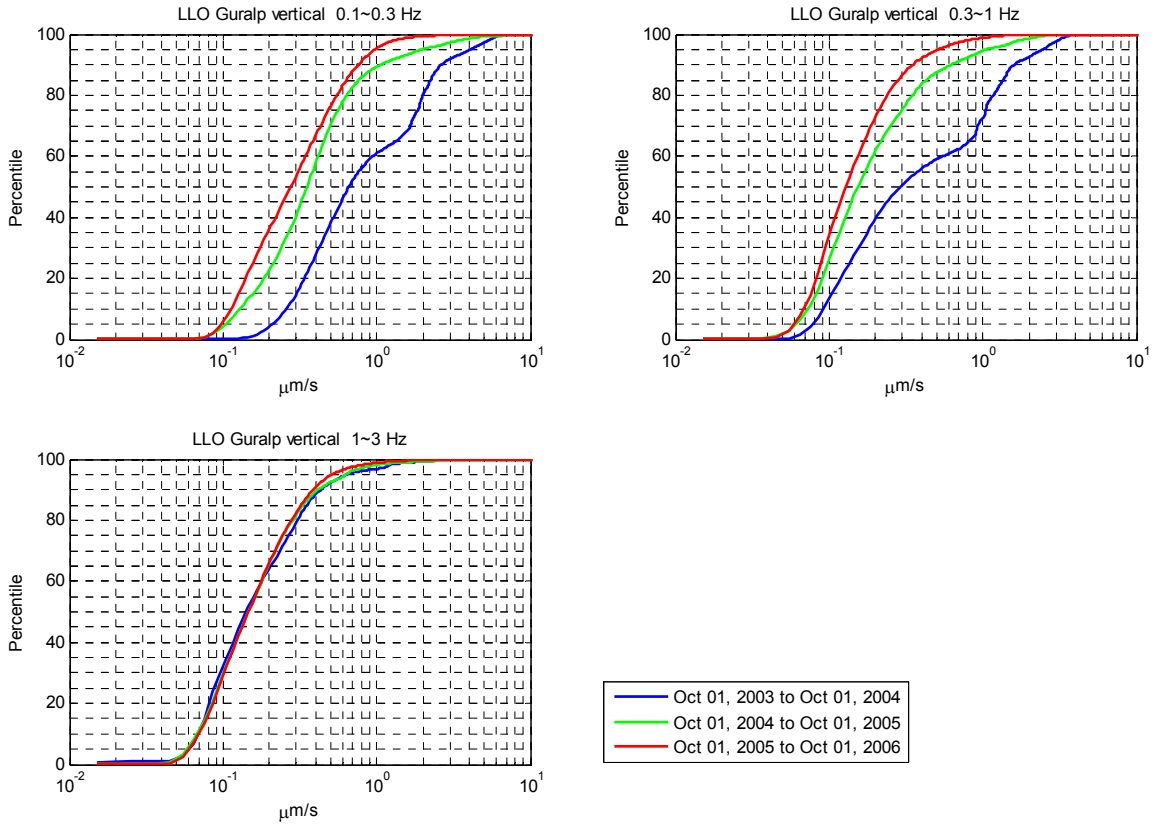

Figure 2.3. Mean vertical rms-velocity percentile profile in each year and band, measured by LLO Guralp seismometers.

Table 2.7. Mean rms-velocity percentile values in each year and band.

LLO Guralp, z direction					
Band	Time span	Velocity percentile (μm/s)			
		50%	75%	90%	95%
0.1~0.3Hz	Oct 1 2003 to Oct 1 2004	0.67	1.85	2.66	4.11
	Oct 1 2004 to Oct 1 2005	0.36	0.57	1.07	1.98
	Oct 1 2005 to Oct 1 2006	0.29	0.50	0.77	0.99
0.3~1Hz	Oct 1 2003 to Oct 1 2004	0.30	1.06	1.62	2.49
	Oct 1 2004 to Oct 1 2005	0.16	0.30	0.63	1.06
	Oct 1 2005 to Oct 1 2006	0.14	0.22	0.36	0.52
1~3Hz	Oct 1 2003 to Oct 1 2004	0.15	0.28	0.44	0.65
	Oct 1 2004 to Oct 1 2005	0.16	0.26	0.43	0.64
	Oct 1 2005 to Oct 1 2006	0.16	0.26	0.40	0.52

Table 2.8. LLO seismic noise level. Mean rms-velocity percentile values in each band, from Oct. 1, 2003 to Oct. 1, 2006.

LLO Guralp, z direction				
Band	Velocity percentile (μm/s)			
	50%	75%	90%	95%
0.1~0.3Hz	0.39	0.68	1.75	2.39
0.3~1Hz	0.16	0.34	1.01	1.42
1~3Hz	0.15	0.26	0.42	0.60

Table 2.9. Noisiest channel in each band, from Oct. 1, 2003 to Oct. 1, 2006.

LLO Guralp, z direction					
Band	Noisiest channel	Velocity percentile (μm/s)			
		50%	75%	90%	95%
0.1~0.3Hz	L0:PEM-EY_SEISZ	0.39	0.72	1.98	4.06
0.3~1Hz	L0:PEM-EY_SEISZ	0.18	0.37	1.18	2.34
1~3Hz	L0:PEM-EY_SEISZ	0.21	0.33	0.51	0.77

and vertical directions. The 1-3Hz band had been more stable. The rms-velocity values had decreased less than a factor of 1.2 at the 50th and 75th percentile in the horizontal direction, and had decreased less than a factor of 1.1 at the 50th, 75th, and 90th percentile in the vertical direction. The Guralp and STS-2 seismometers delivered coarsely consistent data in the 1-3Hz band, with measured rms-velocity values within 25% of each other at the 50th and 75th percentile, and within 50% at the 90th percentile. Any of the data quality issues described in Appendix A could have contributed to this discrepancy, and a more careful selection of the data

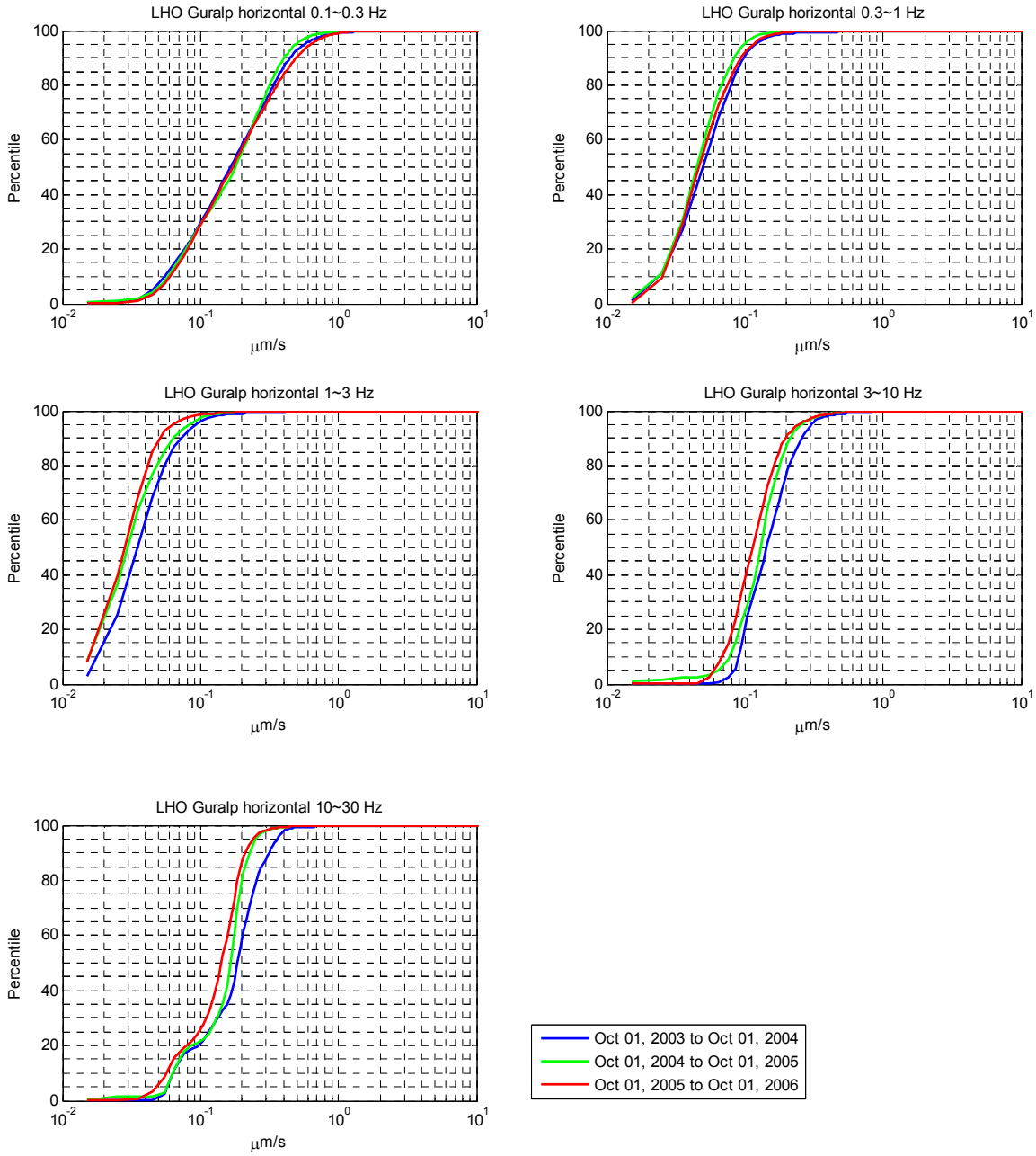

Figure 2.4. Mean horizontal rms-velocity percentile profile in each year and band, measured by LHO Guralp seismometers.

will be needed before attempting to correct it. On average, the horizontal ground motion was about 69% noisier in the 0.1~0.3Hz band, 46% noisier in the 0.3~1Hz band, and 9% quieter in the 1~3Hz band than the vertical motion, as shown in Table 2.5 and 2.8. Above 3Hz the yearly noise trend varied from channel to channel and is best discussed individually, for more details see [20]. Below 3Hz, LLO EY remained the noisiest station, as shown in Table 2.6 and 2.9.

Table 2.10. Mean rms-velocity percentile values in each year and band.

LHO Guralp, horizontal direction					
Band	Time span	Velocity percentile (μm/s)			
		50%	75%	90%	95%
0.1~0.3Hz	Oct 1 2003 to Oct 1 2004	0.16	0.31	0.45	0.58
	Oct 1 2004 to Oct 1 2005	0.19	0.30	0.41	0.50
	Oct 1 2005 to Oct 1 2006	0.18	0.32	0.50	0.64
0.3~1Hz	Oct 1 2003 to Oct 1 2004	0.06	0.08	0.11	0.13
	Oct 1 2004 to Oct 1 2005	0.05	0.07	0.09	0.11
	Oct 1 2005 to Oct 1 2006	0.06	0.08	0.10	0.12
1~3Hz	Oct 1 2003 to Oct 1 2004	0.04	0.06	0.08	0.10
	Oct 1 2004 to Oct 1 2005	0.04	0.05	0.07	0.09
	Oct 1 2005 to Oct 1 2006	0.04	0.05	0.06	0.07
3~10Hz	Oct 1 2003 to Oct 1 2004	0.15	0.21	0.27	0.31
	Oct 1 2004 to Oct 1 2005	0.14	0.16	0.22	0.27
	Oct 1 2005 to Oct 1 2006	0.12	0.16	0.21	0.26
10~30Hz	Oct 1 2003 to Oct 1 2004	0.20	0.25	0.32	0.37
	Oct 1 2004 to Oct 1 2005	0.16	0.20	0.24	0.26
	Oct 1 2005 to Oct 1 2006	0.15	0.19	0.22	0.25

Table 2.11. LHO seismic noise level. Mean rms-velocity percentile values in each band, from Oct. 1, 2003 to Oct. 1, 2006.

LHO Guralp, horizontal direction				
Band	Velocity percentile (μm/s)			
	50%	75%	90%	95%
0.1~0.3Hz	0.18	0.31	0.46	0.58
0.3~1Hz	0.06	0.08	0.10	0.12
1~3Hz	0.04	0.05	0.07	0.09
3~10Hz	0.12	0.15	0.20	0.28
10~30Hz	0.14	0.19	0.22	0.25

Table 2.12. Noisiest channel in each band, from Oct. 1, 2003 to Oct. 1, 2006.

LHO Guralp, horizontal direction					
Band	Noisiest channel	Velocity percentile (μm/s)			
		50%	75%	90%	95%
0.1~0.3Hz	H0:DMT-BRMS_PEM_EX_SEISY	0.21	0.37	0.56	0.72
0.3~1Hz	H0:DMT-BRMS_PEM_EX_SEISX	0.08	0.10	0.13	0.16
1~3Hz	H0:DMT-BRMS_PEM_LVEA_SEISX	0.05	0.06	0.08	0.10
3~10Hz	----------				
10~30Hz	H0:DMT-BRMS_PEM_MX_SEISX	0.22	0.27	0.37	0.40

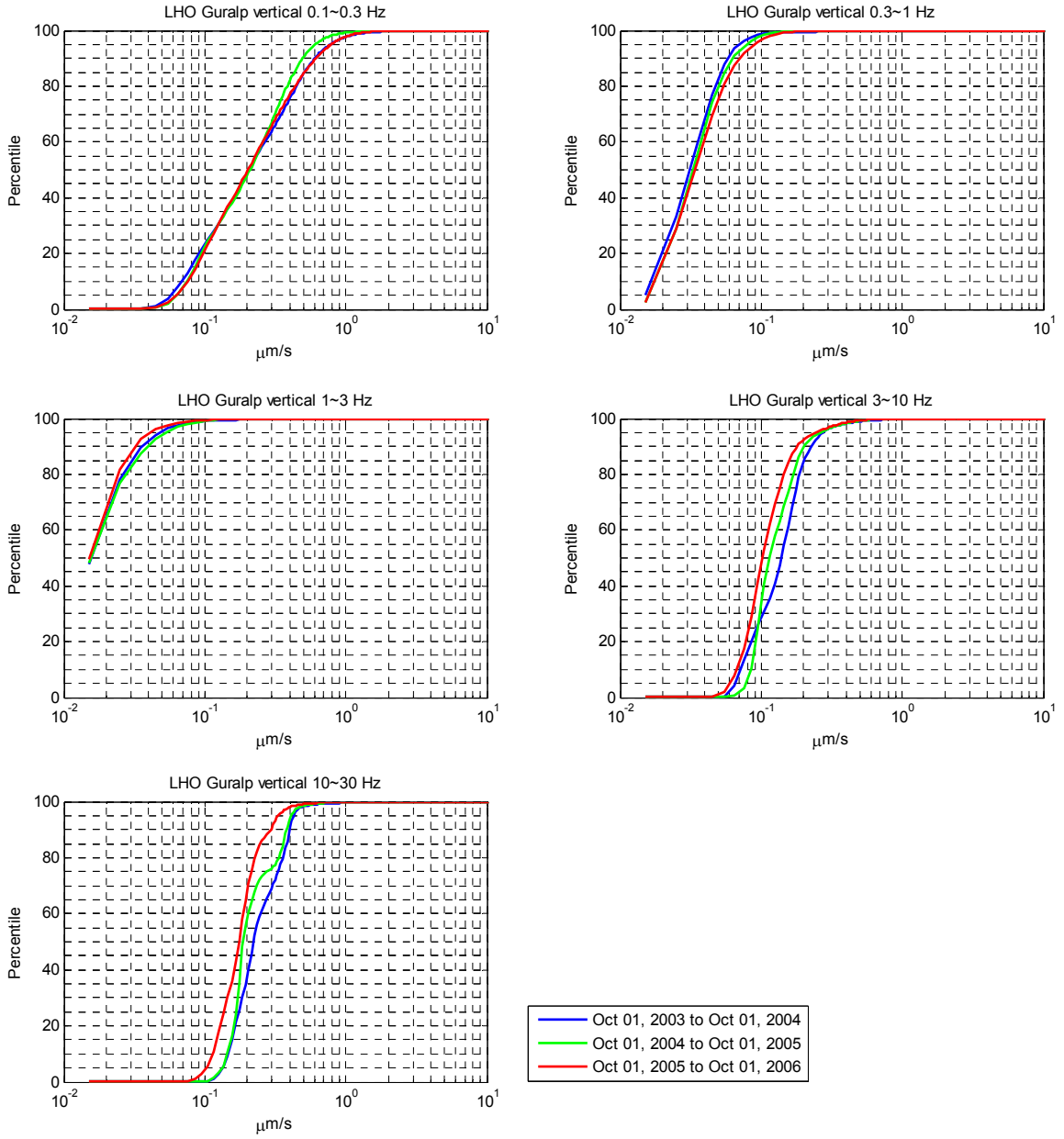

Figure 2.5. Mean vertical rms-velocity percentile profile in each year and band, measured by LHO Guralp seismometers.

2.2 LHO

Table 2.10, 2.11, and 2.12 list the mean rms-velocity percentile values of horizontal signals in each year and band, the mean rms-velocity percentile values of horizontal signals in each band averaged over three years, and the noisiest channel in each band in the three years, respectively,

Table 2.13. Mean rms-velocity percentile values in each year and band.

LHO Guralp, z direction					
Band	Time span	Velocity percentile (μm/s)			
		50%	75%	90%	95%
0.1~0.3Hz	Oct 1 2003 to Oct 1 2004	0.22	0.41	0.61	0.79
	Oct 1 2004 to Oct 1 2005	0.22	0.36	0.51	0.62
	Oct 1 2005 to Oct 1 2006	0.21	0.39	0.62	0.80
0.3~1Hz	Oct 1 2003 to Oct 1 2004	0.04	0.05	0.07	0.08
	Oct 1 2004 to Oct 1 2005	0.04	0.06	0.07	0.09
	Oct 1 2005 to Oct 1 2006	0.04	0.06	0.08	0.10
1~3Hz	Oct 1 2003 to Oct 1 2004	0.03	0.03	0.05	0.06
	Oct 1 2004 to Oct 1 2005	0.03	0.03	0.05	0.06
	Oct 1 2005 to Oct 1 2006	0.03	0.03	0.04	0.05
3~10Hz	Oct 1 2003 to Oct 1 2004	0.15	0.19	0.24	0.28
	Oct 1 2004 to Oct 1 2005	0.12	0.16	0.21	0.27
	Oct 1 2005 to Oct 1 2006	0.11	0.15	0.19	0.25
10~30Hz	Oct 1 2003 to Oct 1 2004	0.22	0.34	0.41	0.44
	Oct 1 2004 to Oct 1 2005	0.20	0.28	0.39	0.42
	Oct 1 2005 to Oct 1 2006	0.18	0.22	0.30	0.34

Table 2.14. LHO seismic noise level. Mean rms-velocity percentile values in each band, from Oct 1 2003 to Oct 1 2006.

LHO Guralp, z direction				
Band	Velocity percentile (μm/s)			
	50%	75%	90%	95%
0.1~0.3Hz	0.21	0.37	0.56	0.71
0.3~1Hz	0.04	0.06	0.08	0.10
1~3Hz	0.03	0.03	0.05	0.06
3~10Hz	0.13	0.18	0.24	0.32
10~30Hz	0.20	0.34	0.41	0.43

Table 2.15. Noisiest channel in each band, from Oct. 1, 2003 to Oct. 1, 2006

LHO Guralp, z direction					
Band	Noisiest channel	Velocity percentile (μm/s)			
		50%	75%	90%	95%
0.1~0.3Hz	H0:DMT-BRMS_PEM_MX_SEISZ	0.22	0.41	0.62	0.79
0.3~1Hz	H0:DMT-BRMS_PEM_EX_SEISZ	0.06	0.08	0.10	0.12
1~3Hz	H0:DMT-BRMS_PEM_EX_SEISZ	0.03	0.04	0.06	0.07
3~10Hz	----------				
10~30Hz	H0:DMT-BRMS_PEM_LVEA_SEISZ	0.36	0.40	0.43	0.46

Table 2.16. Mean rms-velocity values in each band at both sites, Oct. 1 2003 to Oct. 1 2006.

Mean rms-velocity (μm/s)				
Band	LLO Guralp		LHO Guralp	
	Horizontal	Vertical	Horizontal	Vertical
0.1~0.3Hz	1.18	0.70	0.23	0.29
0.3~1Hz	0.54	0.37	0.06	0.05
1~3Hz	0.21	0.23	0.05	0.03

and Table 2.13, 2.14, and 2.15 list those of vertical channels. Over the course of three years, rms-velocity at the 50th, 75th, 90th, and 95th percentile did not vary more than a factor of 1.3 in the 0.1~0.3Hz and 0.3~1Hz bands, in both horizontal and vertical directions. Above 1Hz, the ground gradually got quieter, and rms-velocity at the 50th, 75th, 90th, and 95th percentile did not vary more than a factor of 1.6, in both horizontal and vertical directions. On average, the horizontal ground motion was about 21% quieter in the 0.1~0.3Hz band, 20% noisier in the 0.3~1Hz band, and 67% noisier in the 1~3Hz band than the vertical motion, as shown in Table 2.11 and 2.14.

2.3 Comparing the Two Sites

Table 2.16 compares the mean (average over all stations and all years) rms-velocity in each band recorded by Guralp seismometers at both sites. In the horizontal direction, LLO was noisier by a factor of 5 in the 0.1~0.3Hz band, noisier by a factor of 9 in the 0.3~1Hz band, and noisier by a factor of 4 in the 1~3Hz band than LHO. In the vertical direction, LLO was noisier by a factor of 2.4 in the 0.1~0.3Hz band, noisier by a factor of 7.4 in the 0.3~1Hz band, and noisier by a factor of 7.7 in the 1~3Hz band than LHO.

In the 0.1~0.3Hz band, the LLO horizontal ground motion was about 69% noisier than vertical, whereas at LHO the horizontal was 21% quieter than the vertical. In the 1~3Hz band the situation is reversed, the LLO horizontal ground motion was about 9% quieter than vertical, whereas at LHO the horizontal was 67% noiser than the vertical. Similar result was also reported in Daw's study.

CHAPTER 3: THE HEPI SYSTEM AND ITS ISOLATION PERFORMANCE

The HEPI system was installed to support the in-vacuum payloads within LLO's five Basic Symmetric Chambers (BSC) and four Horizontal Access Modules (HAM). There are four HEPI actuator-sensor units per vacuum tank, located between the top of the four support piers and the ends of the two support beams, see Figure 3.1, 3.2, and 3.3. Each actuator-sensor unit consists of two off-load springs, one vertical and one horizontal hydraulic actuator, one vertical and one horizontal position sensor, and one vertical and one horizontal geophone. See Figure 3.4. All components are bolted inside or around a structural housing. The actuators, geophones, and off-load springs also connect to a common block, which serves as an interface between HEPI and the support beam. Position sensors are located at the top of each actuator. The off-load springs support the static payload and are also used to coarsely position the suspended payload. The actuators operate using viscous hydraulic fluid, which is distributed from central pumps to them and maintained at a constant pressure. The position sensors sense the relative displacement between the top of the each actuator and the mounting block in vertical and horizontal directions, and the geophones sense the velocity in vertical and horizontal directions.

Each HEPI actuator-sensor unit can provide an actuation range of +/-1mm in both vertical and horizontal directions. On BSC tanks, the horizontal actuator and sensor axis is 45 degree relative to the light beamline. On HAM tanks, the angle is 30 degrees. See Figure 3.5. Correct combinations of the forces delivered by the horizontal actuators and signals sensed by the horizontal sensors will provide actuation and sensed motion of the payload in the X, Y, rotational about the Z axis (RZ), and the horizontal over-constrained (HO) degrees of freedom (DOF). Correct combinations of the forces delivered by the vertical actuators and signals sensed by the vertical sensors will provide actuation and sensed motion in the Z, RX, RY, and the vertical

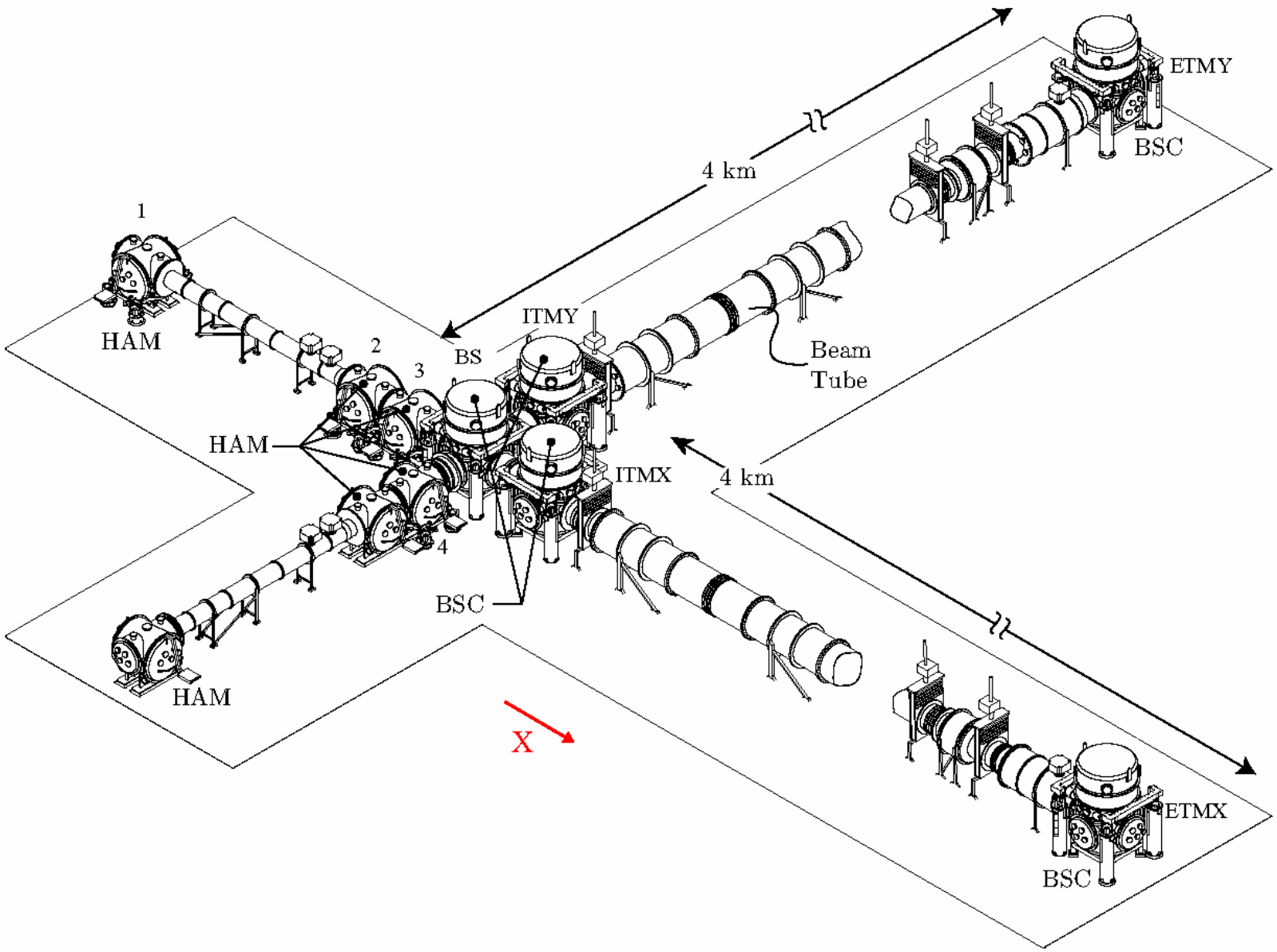

Figure 3.1. Chambers with HEPI installed: BS, ITMX, ITMY, ETMX, ETMY, and HAM1~4. Figure courtesy of Oddvar Spjeld.

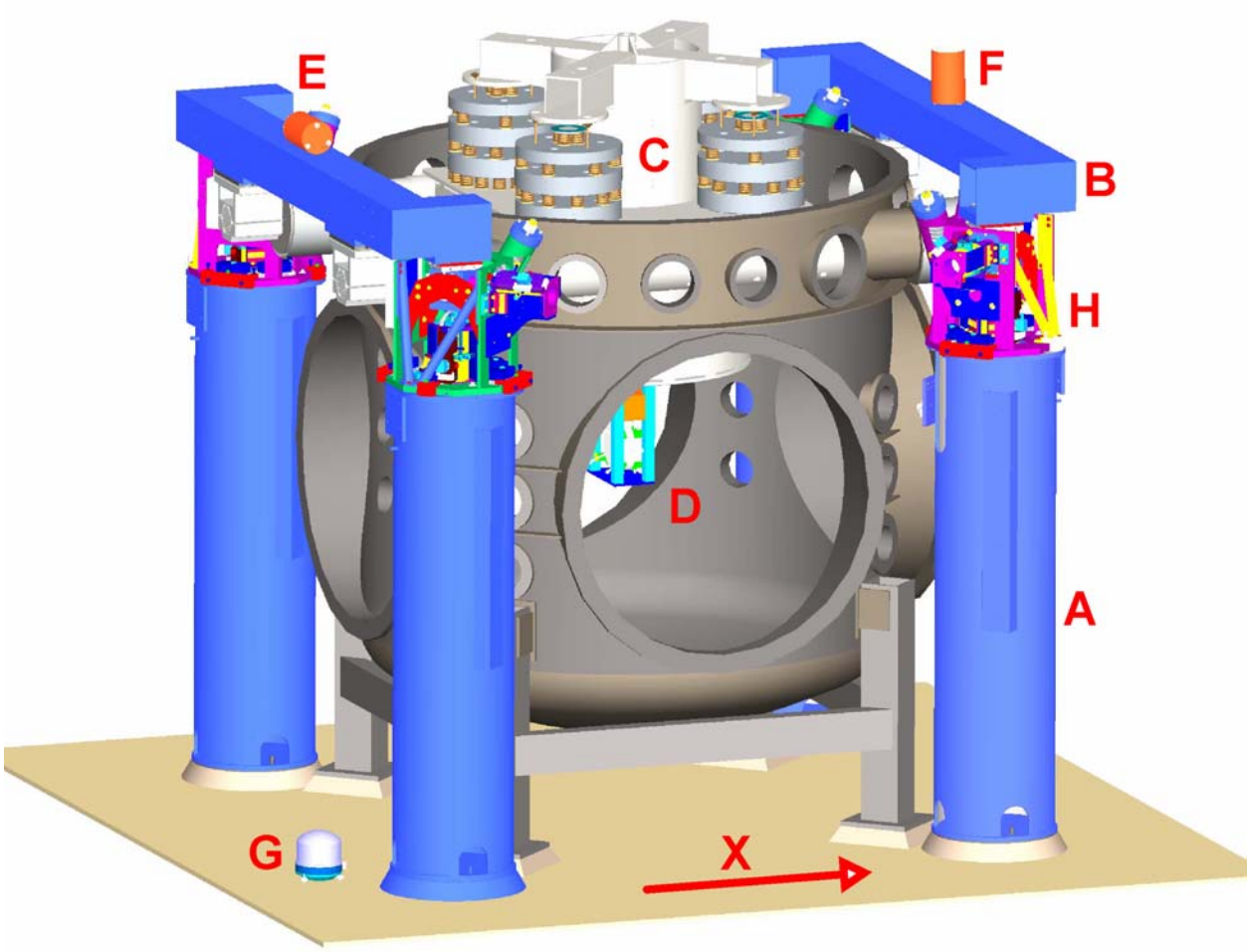

Figure 3.2. BSC and HAM (see Figure 3.3) chambers with four HEPI sensor-actuator assemblies (H), installed between the top of the four support piers (A) and the ends of the two support beams (B). Also visible are the in-vacuum isolation stacks (C), suspended optic (D), horizontal (E) and vertical (F) witness GS-13 geophones, and STS-2 seismometer (G). General LLO X direction relative to each chamber is marked by the arrow, except for ETMY, ITMX, and HAM4, for which the arrow marks the Y direction.

over-constrained (VO) DOF. The two over-constrained DOFs are associated with the fact that there are only six DOF but eight actuator and eight sensors per tank, and the fact that the entire structure is not infinitely rigid and can be physically deformed. See Figure 3.5.

Analog signals of the payload motion sensed by the geophones are converted to digital signals. The signals are then digitally filtered, converted to analog signals and used to command the actuators, resulting in forces on the payload. This forms a feed-back loop which suppresses the motion of the payload.

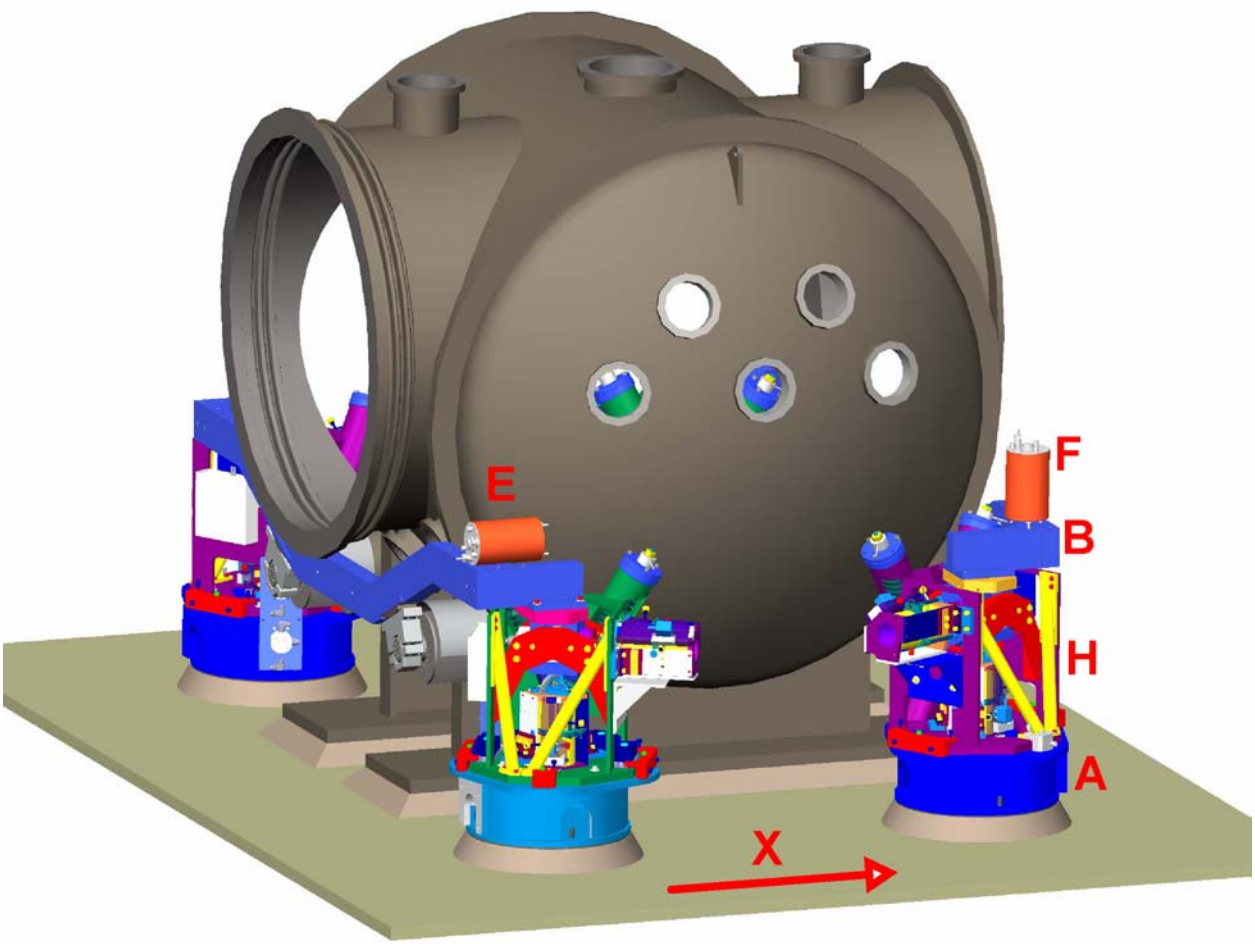

Figure 3.3.

Position signal of the payload is processed in the same fashion, resulting in a feed-back loop which accurately positions the payload with respect to the pier top. Ground motion sensed by STS-2 seismometers is then feed-forwarded (subtraction) into the error point of the position feed-back loop. The goal is to command the motion of the payload by the same amount but in opposite direction as the ground motion, more effectively lowering the ground motion to payload motion transfer function. Also, see the control diagram of BSC HEPI system shown in Figure 3.8.

In the HEPI system we use a signal sampling rate of 2048Hz, which is sufficient to resolve most low order mechanical resonances and transfer functions, and use those to design stable control loops. The analog to digital converter and the digital to analog converter used are 16 bit.

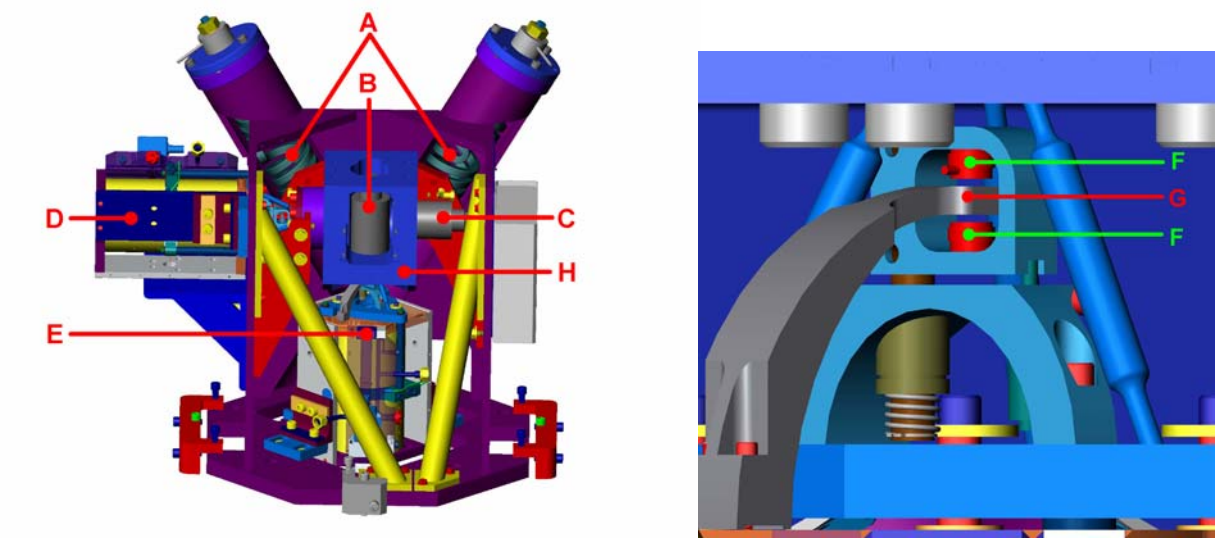

Figure 3.4. Left panel: HEPI actuator-sensor assembly, showing the off-load springs (A), vertical (B) and horizontal (C) geophones, vertical (E) and horizontal (D) actuators, and interfacing block (H). Part of the support structure has been removed from the plot to reveal the geophones. Right panel: position sensors are located at the top of the actuator assembly, picture shows the inductance coil (F) and the target (G).

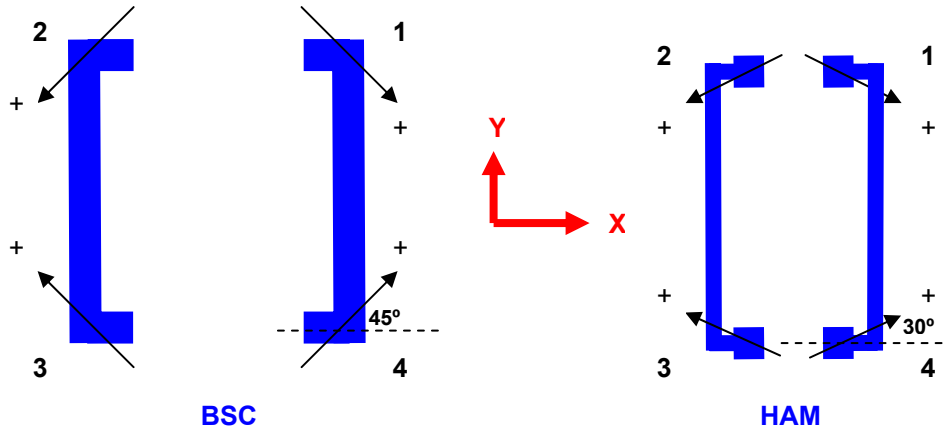

Figure 3.5 Naming convention for the BSC (BS, ETMX, and ITMY) and HAM (1 to 3) HEPI units. Figure shows the top view of the BSC and HAM support beam assemblies. LLO X and Y directions are shown by the red arrows. Vertical direction Z points out of paper. Horizontal actuators and sensors are prefixed with an H, while the vertical ones with a V. For example actuator V1 means vertical actuator at position 1. Positive horizontal actuation and positive horizontal sensor readings by each HEPI unit are defined by the plus signs. Rotational DOFs are defined with the usual right-hand rule. HO DOF is achieved when all four corners are actuated in the positive or negative direction simultaneously. VO DOF is achieved when 1 and 3 corners are actuated in the +Z direction while 2 and 4 corners are actuated in the -Z direction, or vice versa. For ETMY, ITMX, rotate the blue support beams by 90 degrees while keeping everything else fixed. For HAM4, do the same thing but change the angle to 60 degree.

3.1 HEPI Actuator and Sensors

Servo Valve Controlled Hydraulic Actuators

Each HEPI actuator applies a force by creating differential hydraulic pressure between its two bellows which act as pistons. An actuation plate is situated between the bellows so the differential pressure at two sides delivers a net force which can be used to move the payload. The differential pressure is controlled by a modified Parker DYP2SC servo valve, which is a hydraulic Wheatstone bridge, and the differential pressure (and hence the delivered force) has near-linear response to electrical control current. The center actuation plate between the bellows connects to the payload via a tripod. Two sides of the center actuation plate also connect to its adjacent support structure via two flexible joints, each with two rotational DOFs. The flexibility of the bellows, tripod, and the side flexible joints allow a pair of vertical and horizontal actuators at each corner to operate individually or simultaneously without over-constraining the actuator-to-payload attachment points (Figure 3.6a). Below a certain frequency (<0.1Hz), called the *channel frequency*, the actuator is essentially a force actuator. The force delivered by the actuator is used to overcome the weight of the payload or the forces of the off-load springs, and the payload's displacement and is proportional to control current. Above this frequency the actuator behaves as a velocity actuator, and the payload's displacement responds to control current with 1/f relationship. The actuator is designed to have an actuation range of +/-1mm, a bandwidth more than 20Hz, noise roughly $10^{-10}\,\mathrm{m}/\sqrt{\mathrm{Hz}}$ from 1 to 10Hz, and a payload capacity of 2000 kg [6].

Kaman Measuring Systems, DIT-5200 Position Sensor

DIT-5200 is an inductance type position sensor. With HEPI's 2048 Hz sampling rate and +/-1mm range, it delivers effective resolution of 18 nm. With +/- 2^{15} digital counts available, the position sensor readouts saturates at +/-0.59mm, which limits HEPI's usable range [21].

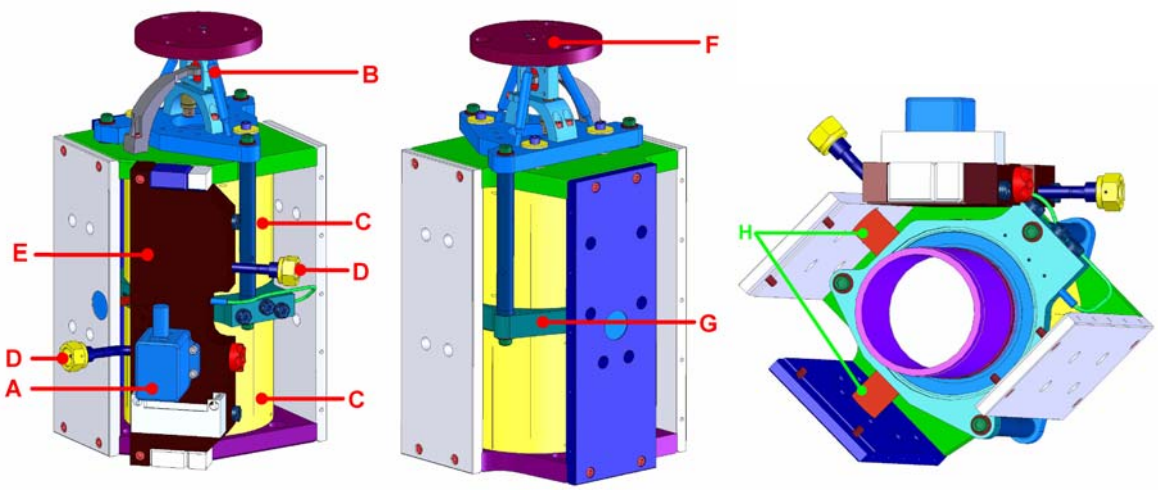

Figure 3.6a. HEPI actuator, showing the Parker DYP2SC valve (A), tripod (B), bellows housing (C) (bellows are inside), fluid inlet and outlet (D), manifold (E), payload attachment plate (F), actuation plate (G). Bottom view is shown on the right, showing the side flexible joints (H). Lower structural plate and bellow are removed from the plot for better visibility.

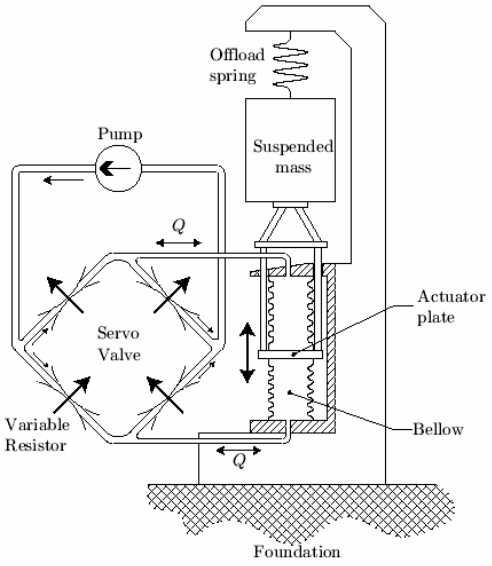

Figure 3.6b. A schematic diagram of the HEPI actuator. Courtesy of Corwin Hardham.

Mark Products, L-4C 1Hz Geophone

L-4C is a velocity transducer type geophone which has a near flat response of 276 Volt/(m/s) above 1 Hz, below 1 Hz the response fall off as f^2. We Use them in horizontal and vertical configurations in the HEPI system [22].

Streckeisen, STS-2 Seismometer

STS-2 is a broad band, low noise, 3-axis seismometer. Relative ground to test-mass motion is measured by a capacitive displacement transducer, producing a signal that is fed-back to force the test mass to move with the ground. Instrument output signal is proportional to the feed-back signal. It has near-flat response of 1500 Volt/(m/s) from 10 mHz to 10 Hz, and phase change less than 10 degree from 100 mHz to 10Hz. The broad band capability is made possible by suspended test mass of very low resonant frequency [16].

Geotech Instruments, GS-13 Geophone

The GS-13 geophone is not part of the HEPI system. However, it is used for measuring the motion of the payload, obtaining feed-forward data, measuring the isolation performance, and various other diagnoses. The geophone has an electromagnetically damped mass-spring design with velocity transducer attached to the test mass. It has a near-flat response of 500 Volt/(m/s^2) from 0.1 to 10 Hz with phase change less than 10 degree, and convertible to horizontal and vertical configurations [23].

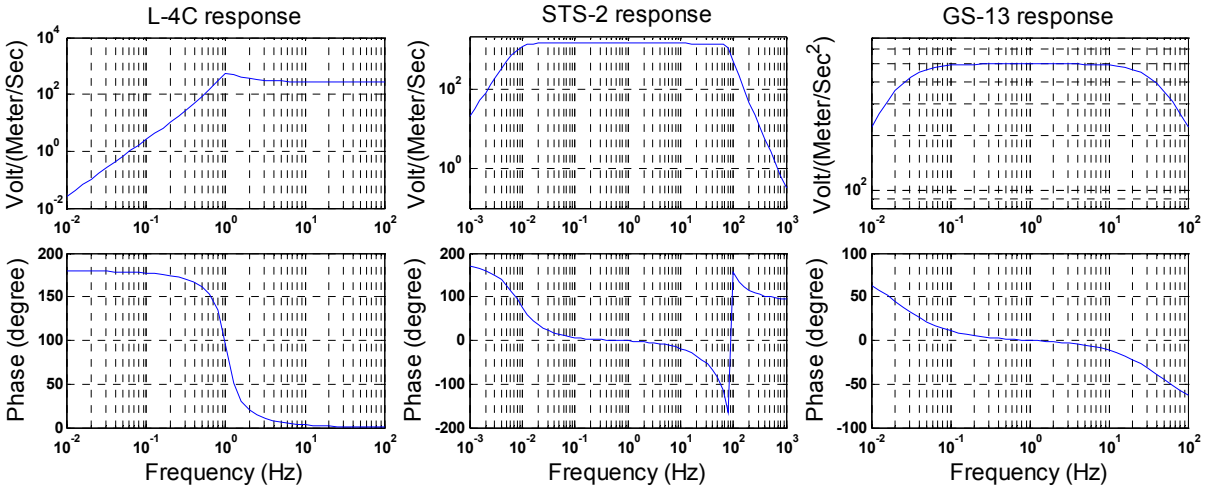

Figure 3.7 Sensor responses.

3.2 Control Scheme of Basic Symmetric Chambers (BSC)

In order to design a stable control system for the BSC HEPI, we first measure its response to actuator forces. This is called system identification. We start by driving each individual actuator with sinusoidal signal at frequencies ranging from 0.01 to 800Hz, and looking at the response signal of each sensor. The ratio of the two signals, or transfer function (TF), provides us the mechanical and electric response of components of the HEPI system and the payload it supports, and determines or limits how well they can be controlled altogether. Since there are 8×8 actuator-sensor combinations for both the position and geophone sensors, there is equal number of transfer functions. See the block diagram in Figure 3.8. The transfer functions obtained here are equivalent to driving at point **a,** and measuring the responses at point **b** and **c**, while breaking the loops immediately after **b** and **c**. We define $TF_{ab,}$ and TF_{ac} as the actuator to position and geophone sensor transfer function matrices. Also, see Figure 3.9 for an example.

We next determine the normalization factors, **N**, for the actuators. For a given actuator, **N** is inversely proportional to the mean actuator to co-located position sensor response from 0.5 to 2Hz. The intention is to compensate for any variation in the actuators, so that regardless of which actuator is chosen, the same actuator drive signal, after passing through **N** in the software, delivers the same actuation.

To sense the position and motion of the payload, signals from each position and geophone sensors, arranged in 1 by 8 row vector form, [H1 H2 H3 H4 V1 V2 V3 V4], are multiplied by an 8 by 8 sensor-to-mode matrix to form modal position and geophone sensor signals, which are also in row vector form, [X Y RZ HO Z RX RY VO]. This is equivalent to going from point **b** to **e** and point **c** to **f** in Figure 3.8. The 8 by 8 matrix is,

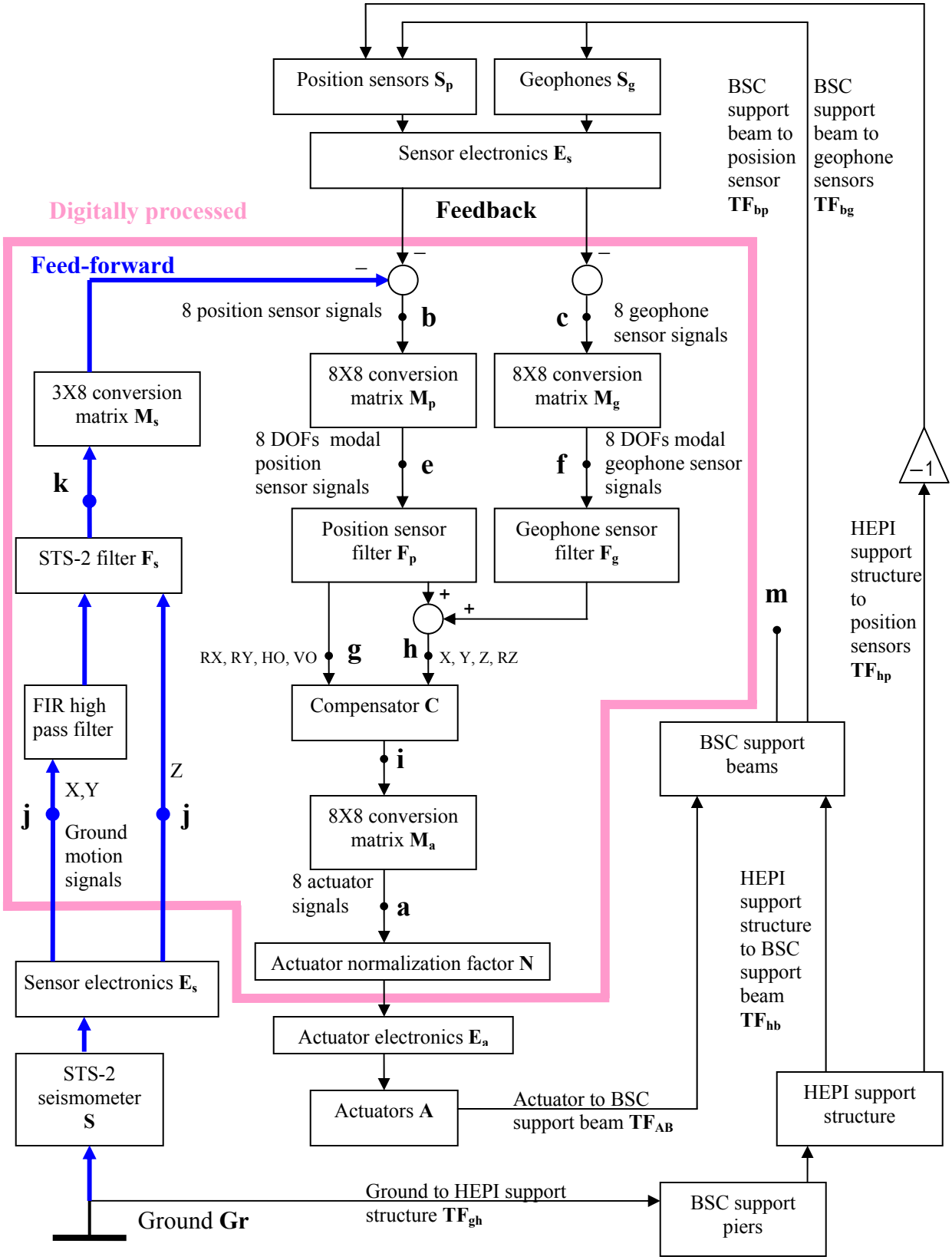

Figure 3.8. Schematic diagram of BSC HEPI system

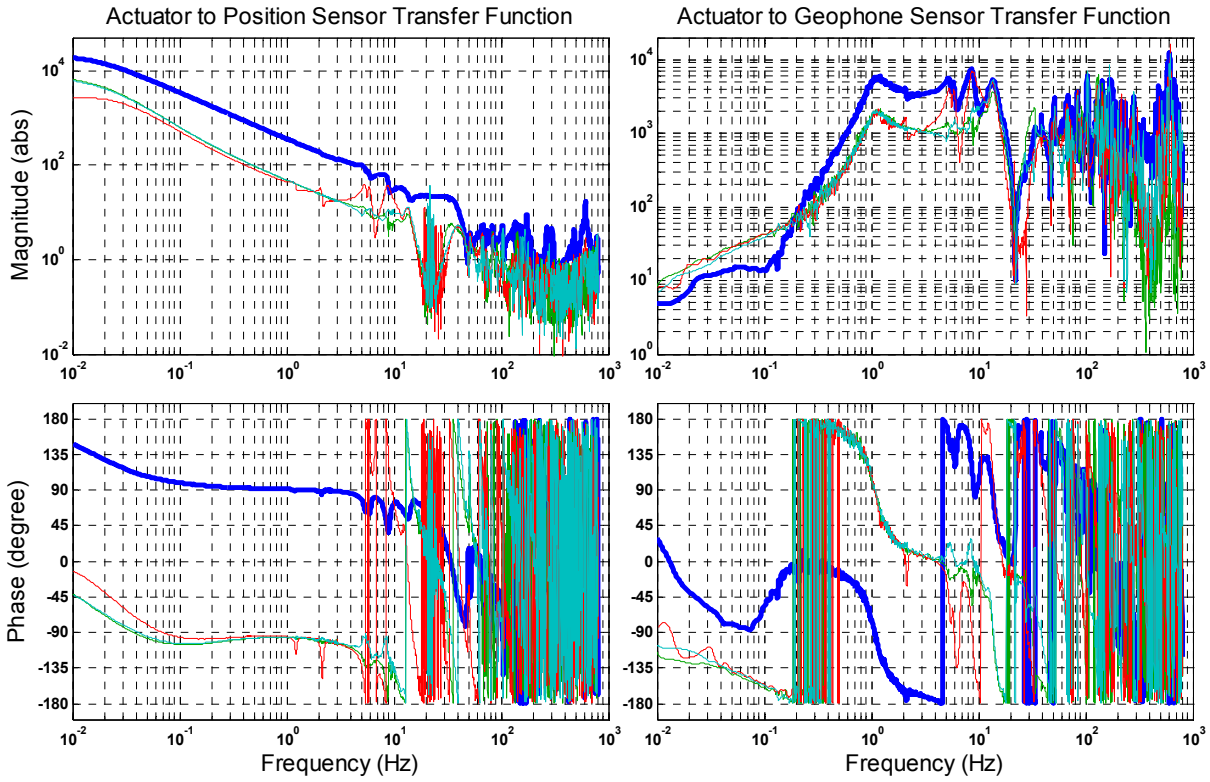

Figure 3.9. Measured ETMX H1 actuator to horizontal position and geophone sensor transfer functions. See Figure 3.8, the transfer functions obtained here are equivalent to driving at point **a** and measuring the responses at points **b** and **c**, while breaking the loops immediately after **b** and **c**. The transfer functions of co-located actuator-sensor pairs have highest responses, shown as bolded blue traces, as the actuator and sensors are closest to each other. Since actuator and sensor signals are converted into digital counts, the magnitude of the transfer functions shown here are not in real unit but in digital counts as well. As described in Section 3.1, the actuator to position sensor transfer functions should have ~1/f dependence. Also visible in the actuator to position sensor transfer functions at just below 0.1Hz is the channel frequency where the response starts flattened-out.

$$M_p = M_g = \frac{1}{4}\begin{bmatrix} 1 & -1 & -1 & 1 & 0 & 0 & 0 & 0 \\ -1 & -1 & 1 & 1 & 0 & 0 & 0 & 0 \\ -1 & 1 & -1 & 1 & 0 & 0 & 0 & 0 \\ 1 & 1 & 1 & 1 & 0 & 0 & 0 & 0 \\ 0 & 0 & 0 & 0 & 1 & 1 & -1 & 1 \\ 0 & 0 & 0 & 0 & 1 & 1 & 1 & -1 \\ 0 & 0 & 0 & 0 & 1 & -1 & 1 & 1 \\ 0 & 0 & 0 & 0 & 1 & -1 & -1 & -1 \end{bmatrix}$$, for BS, ETMX, and ITMY, or

$$M_p=M_g=\frac{1}{4}\begin{bmatrix} -1 & 1 & 1 & -1 & 0 & 0 & 0 & 0 \\ 1 & 1 & -1 & -1 & 0 & 0 & 0 & 0 \\ 1 & -1 & 1 & -1 & 0 & 0 & 0 & 0 \\ -1 & -1 & -1 & -1 & 0 & 0 & 0 & 0 \\ 0 & 0 & 0 & 0 & 1 & 1 & -1 & 1 \\ 0 & 0 & 0 & 0 & 1 & 1 & 1 & -1 \\ 0 & 0 & 0 & 0 & 1 & -1 & 1 & 1 \\ 0 & 0 & 0 & 0 & 1 & -1 & -1 & -1 \end{bmatrix}$$, for ETMY and ITMX.

The 4 by 4 sub-matrix in the upper-left quadrant transforms horizontal sensor signals, and the one in the lower-right transforms vertical.

To move the payload in certain direction, a command signal passes through a mode-to-actuator matrix M_a, which is exactly M_p^{-1} ($=M_g^{-1}$), to generate signals that drive the appropriate actuators to move the payload in the desired DOF. The is equivalent to going from point **i** to **a** in Figure 3.8.

To form the modal actuator to modal position and geophone sensor transfer function matrices, $TF_{ab,}$ and TF_{ac} are pre-multiplied by the mode-to-actuator matrix and multiplied by the sensor-to-mode matrices, or similarity transformations $M_a(TF_{ab})M_p$ and $M_a(TF_{ac})M_g$. The transfer functions synthesized here are equivalent to driving at point **i** and measuring the responses at point **e** and **f**, while breaking the loops immediately after **e** and **f** in Figure 3.8. For perfectly symmetric mechanical structure with perfectly normalized actuators and identical sensors, TF_{ab} and TF_{ac} are symmetric matrices, the column vectors of M_p and M_g form the eigenvectors of TF_{ab} and TF_{ac}, and the matrices M_p and M_g diagonalize TF_{ab} and TF_{ac} via the similarity transformation. In reality, TF_{ab} and TF_{ac} are asymmetric, and 8×8 pairs of modal actuator to modal position and geophone sensor transfer functions are generated by the transformation. The diagonal terms are associated with same-DOF modal actuator to sensor transfer functions, and the off-diagonal terms are with cross-coupling modes. To keep the system control design simple, we only used the diagonal terms. Off-diagonal terms were

not used since we expected the cross-coupling modes are less prominent in HEPI. It is possible to diagonalize the real-world TF_{ab} and TF_{ac}, however this posses extra challenges as in reality M_p and M_g will be complex and different at different frequencies.

On BSC tanks we employ four types of control schemes. They are the control of translational DOFs, X,Y, and Z, the control of rotational DOF, RZ, the control of rotational DOFs, RX, and RY, and the control of over-constrained DOFs, HO, and VO.

X, Y, and Z DOFs

For these DOFs, we utilize the geophone sensors, position sensors in the feedback, and feed-forward to suppress payload motion.

After the modal position and geophone sensor signals are formed (see Figure 3.10 for example), the modal position sensor signal passes through a low pass position sensor filter, and the modal geophone sensor signal passes through a high pass geophone sensor filter. The gain of the modal position sensor signal is adjusted so that the frequency where it has equal magnitude as the modal geophone sensor signal is 0.5Hz. We customarily call this frequency the *Blend frequency*. The two signals are then added together to form a modal super sensor signal and filtered by a compensator further downstream. The filtered super sensor signal then pass through the actuator matrix and generates signals that drive the appropriate actuators to move the payload in the DOF same as the DOF of motion sensed by the super sensor. Finally payload motion gets sensed by the individual sensors, completing a feed back loop (Figure 3.11)

Ground motion sensed by the STS-2 seismometer, after being filtered by the STS-2 filter, transformed by the 3 by 8 matrix, forms the feed-forward signal which is fed into the error point of the position sensor loop at point **b**.

Assuming the only disturbance is from the ground, we next derive the ground motion to payload motion transfer function. The motion at the support beam for a given DOF is,

$$
\begin{aligned}
m = &(Gr\ TF_{gh}\ TF_{hp} - m\ TF_{bp}\ S_p\ E_s)\ M_p\ F_p\ C\ M_a\ N\ E_a\ A\ TF_{AB} \\
&- m\ TF_{bg}\ S_g\ E_s\ M_g\ F_g\ C\ M_a\ N\ E_a\ A\ TF_{AB} \\
&+ Gr\ TF_{gh} TF_{hb} \\
&- Gr\ S\ E_s\ F_s\ M_s\ M_p\ F_p\ C\ M_a\ N\ E_a\ A\ TF_{AB}
\end{aligned}
$$

The first term is from the position sensor feedback loop, bearing in mind that the sensors measure the relative displacement between the support beam and the HEPI support structure. The second term is from the geophone sensor feedback loop. Each multiplicative factor in the first two terms is picked-up as one starts from point **m** in Figure 3.8, goes counter-clockwise, and ends at point **m** to complete the loops. The third term is from ground motion propagating through the support piers and HEPI structure to the support beams. The forth term is from the feed-forward signal injected into the error point of the position sensor loop, and then from the error point, the signal propagates down-stream along the position sensor signal path until it reaches point **m**.

Define the following parameters:

The position sensor loop gain $G_p = TF_{bp}\ S_p\ E_s\ M_p\ F_p\ C\ M_a\ N\ E_a\ A\ TF_{AB}$.

The geophone sensor loop gain $G_g = TF_{bg}\ S_g\ E_s\ M_g\ F_g\ C\ M_a\ N\ E_a\ A\ TF_{AB}$.

Feed-forward gain $G_s = S\ E_s\ F_s\ M_s$.

Ground to BSC support beam transfer function $TF_{gb} = TF_{gh} TF_{hb}$.

The derivation above can be simplified to,

$$m = (Gr\ TF_{gh}\ TF_{hp}\ G_p / TF_{bp}) - m\ G_p - m\ G_g + Gr\ TF_{gb} - Gr\ G_s\ G_p / (TF_{bp}\ E_s\ S_p) .$$

Due to the way the position sensors are mounted and the mechanical stiffness of the involved mounting hardware, TF_{hp} and TF_{bp} can be set to one for good low frequency approximation. We further assume all the sensor electronics E have gain of one.

$$m = (Gr\ TF_{gh}\ G_p) - m\ G_p - m\ G_g + Gr\ TF_{gb} - Gr\ G_s\ G_p / (S_p)$$

Then, the ground motion to support beam motion transfer function is,

$$\frac{m}{Gr} = \frac{TF_{gb} + TF_{gh}G_p - G_s(G_p/S_p)}{1 + G_g + G_p}. \qquad \text{(Equation 3.1)}$$

The higher G_g is, the more suppression is provided by the system since G_g is in the denominator. If the feed-forward were absent, $G_s = 0$,

$$\frac{m}{Gr} = \frac{TF_{gb} + TF_{gh}G_p}{1 + G_g + G_p}. \qquad \text{(Equation 3.2)}$$

The position sensor loop attempts to lock the payload motion to the motion of the HEPI support structure, as G_p is in both the denominator and the nominator. The presence of the position sensor loop interferes with the suppression obtained from the geophone loop. However, with the feed-forward path, a proper choice of G_s minimizes the numerator and hence |m/Gr| [24, 25].

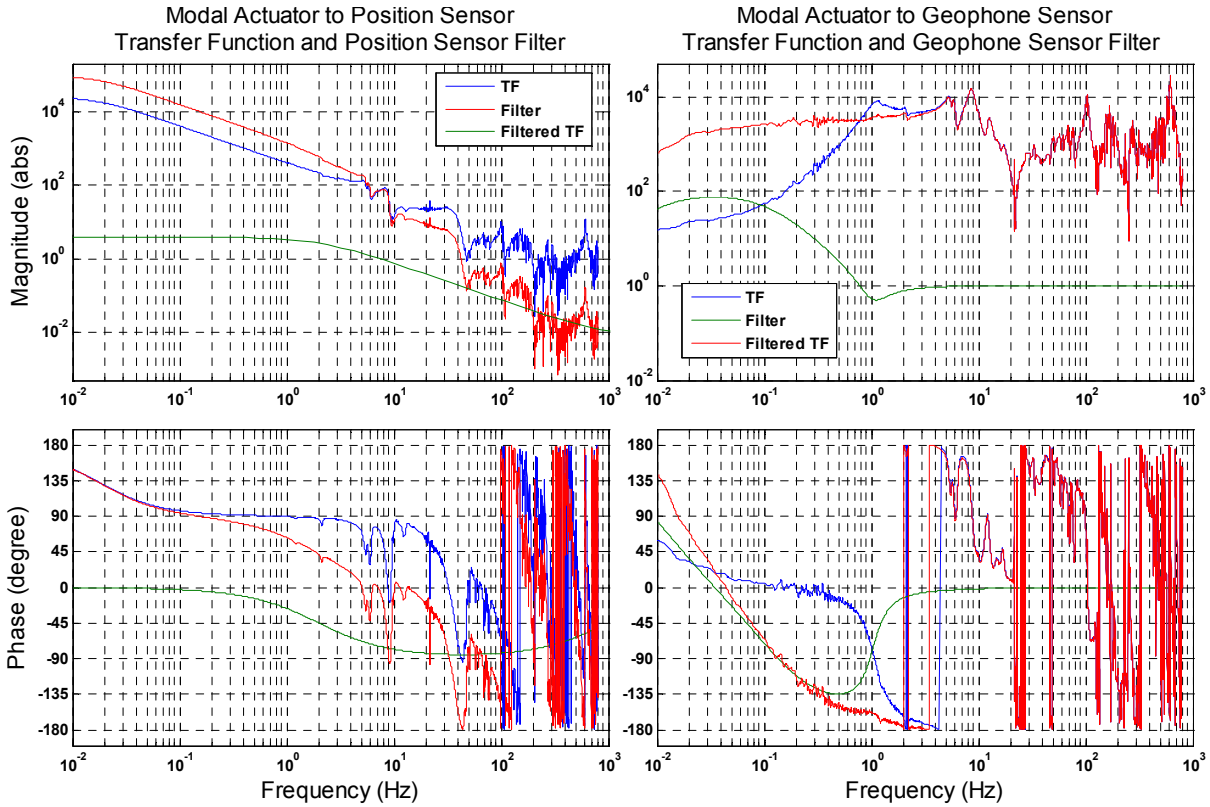

Figure 3.10. Synthesized ETMX X DOF modal actuator to position and geophone sensor transfer functions. See Figure 3.8, the transfer functions obtained here are equivalent to driving at point **i** and measuring the responses at points **e** and **f**, while breaking the loops immediately after **e** and **f**. Transfer functions are then reshaped by sensor filters, shown in green, and the filtered transfer functions are shown in red.

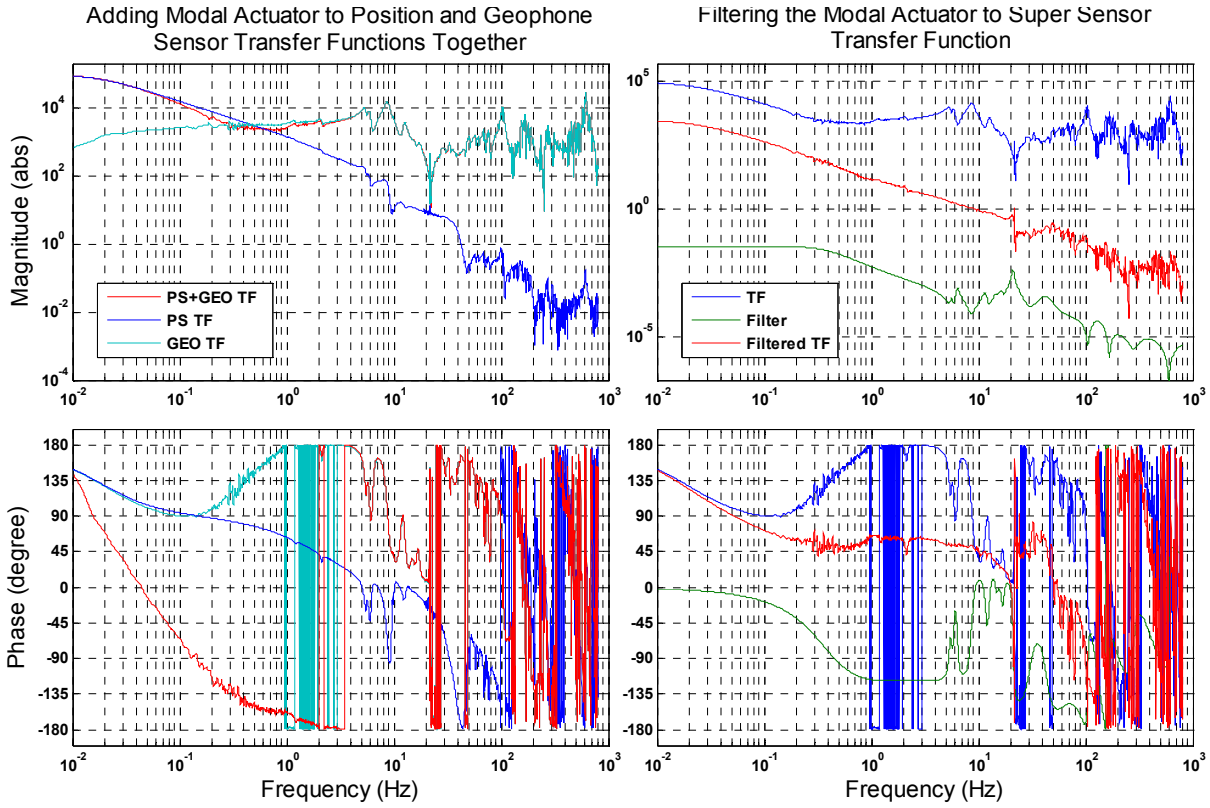

Figure 3.11 Left two panels: Synthesized ETMX X DOF modal actuator to super sensor transfer function, formed after the filtered modal actuator to position and geophone sensor transfer functions are added together. Also see Figure 3.8, the equivalent transfer function obtained here is equivalent to driving at point **i** and measuring the responses at **h**, while breaking the loop immediately after **h**. Right two panels: The transfer function is then reshaped by the compensator, shown in green. The filtered transfer function, shown in red, is equivalent to point **i** to **i**, or a complete loop transfer function.

System stability is obtained if

$$\frac{1}{1+G} < \infty, \qquad \text{(Equation 3.3)}$$

where $G=G_p+G_g$, the overall loop gain. The rule of thumb we applied is allowing 45 degree of phase margin at and below the unity gain frequency (ugf), and a factor of 3 of gain margin above the ugf. This puts the slope of the loop gain below ugf roughly $1/f^{1.5}$.

The geophone sensitivity drops as f^2 below 1Hz. The geophone filter is shaped in a way that utilizes the geophone signal between 0.5 and 1Hz, where there is still sufficient sensitivity, to provide some ground motion suppression in that frequency range. The filter also high passes the

signal below 0.1Hz, where the there is little sensitivity, to prevent sensor noise from entering the HEPI system.

The position sensor feed back loop works with feed-forward to provide isolation. From our experience the isolation obtained from feed-forward starts to degrade and adds noise to the system above 1Hz, hence we choose to low passes the position sensor signal at ~1Hz.

The compensation filter mainly provides three functions: it compensates for mechanical resonance; it augments the control loop gain while providing sufficient gain and phase margins; and it attenuates high frequency resonance to prevent system oscillation or instability. Looking at the actuator to modal super sensor transfer functions, the lower order modes of the LIGO stacks below 10Hz are easily identified and can be compensated by a pair of complex poles and zeros. These are the horizontal-horizontal transfer modes at roughly 1.2, 2.1, 5.5, and 10Hz, and vertical-vertical transfer modes at roughly 2.7, 6.5, and 10Hz. At 20 to 60 Hz, there is a broad-band feature which includes the actuator bellow expansion mode, actuator tripod compression mode, support beam flexing mode, support pier horizontal vibration mode (Figure 3.12) [6, 26, 27, 28, 29, 30], and many other fine mechanical resonances. While the quality of the actuator bellow expansion mode has been reduced by adding internal flow resistors, other modes remained untouched. In practice it is very hard to compensate those perfectly and this is the primary limitation of setting the control loop ugf above 20Hz. We conservatively set the ugf at around 10Hz. Above 60Hz various resonances are seldom well resolved, we attenuate signal above 60Hz enough without loosing phase margin at ugf. All of this is done while satisfying Equation 3.3.

RZ DOF

The control scheme for RZ is the same as previously described in X, Y, and Z, except the absence of feed-forward signal going into the position sensor loop error point. The RZ motion at

Mode number	Frequency (Hz)
1	29.0198
2	29.8968
3	217.2563
4	221.7740
5	232.3236

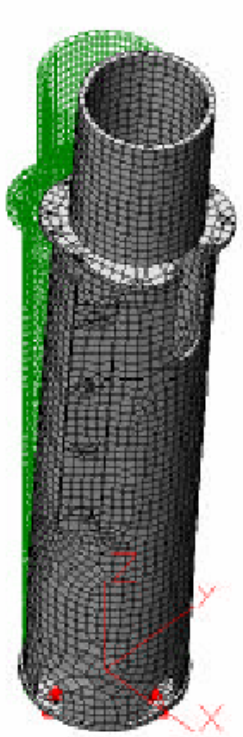

Figure 3.12a. Finite element analysis of the pier vibration. Work by Ken Mason.

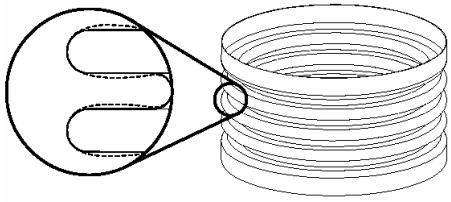

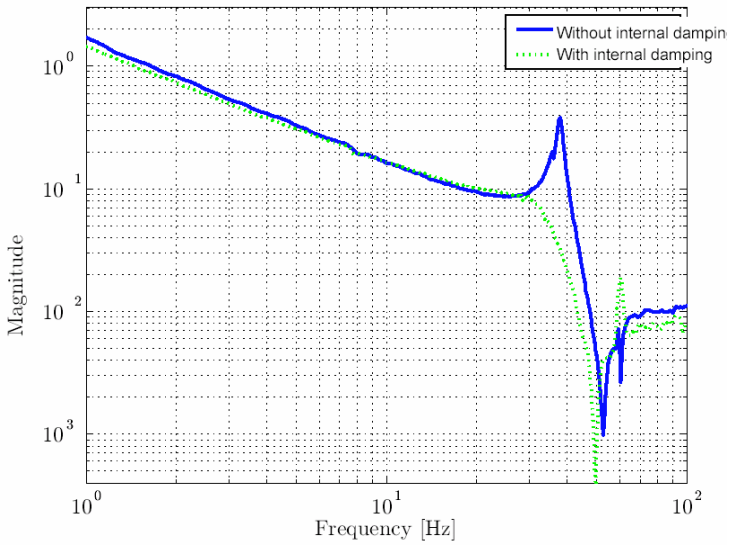

Figure 3.12b. Bellow expansion mode near 40Hz due to internal fluid pressure. Right: transfer functions of actuator to position sensor with and without actuator internal damping mechanism (resistors) to dampen the mode. The first zero at ~50Hz is believed to be the tripod compression mode. Work by Corwin Hardham.

the HEPI stage transfers to the optics table in the same DOF, and affects the suspended optic yaw alignment. It is intended that above the blend frequency the geophone loop suppresses the payload motion, and below it the position sensor loop keeps the relative position between the support piers and payload fixed. Loop stability is still described by Equation 3.3

RX and RY DOFs

For the RX and RY DOFs, we only use the position sensors in the feed-back loop. The position sensor filter $\mathbf{F_p}$ is merely 1, and the compensator is essentially a position sensor filter (Figure 3.13). The effect is to keep the relative position between the support piers and payload fixed. There is no intended motion suppression in these two DOFs. Loop stability is still described by Equation 3.3 but with G_g=0.

The strategy not to incorporate RX and RY geophone signals into motion control was based on the group's experience that the RX RY ground motion is quiet enough for our needs, and quieter than the X, Y, and Z DOFs, and we intended to keep the control system as simple as possible. Because, the consensus is not based on hard data, we experiment on this later, after HEPI was stabilized. See Section 5.1. For S4, S5 science runs we kept the RX and RY under control of position sensor loops only.

HO and VO DOFs

These two DOF are less well studied. The control scheme for HO and VO DOFs is the same as previously described in RX and RY, except for an extra high pass component in the compensator which essentially consists of a real pole at ~0.1Hz and zero at 0Hz (Figure 3.13). Due to the flexibility of the support piers and support beams, these modes were suppressed inAC to prevent the motion in these two modes from propagating to other DOFs. Ideally one would constrain these two modes down to DC, but for the following reason we did not do so:

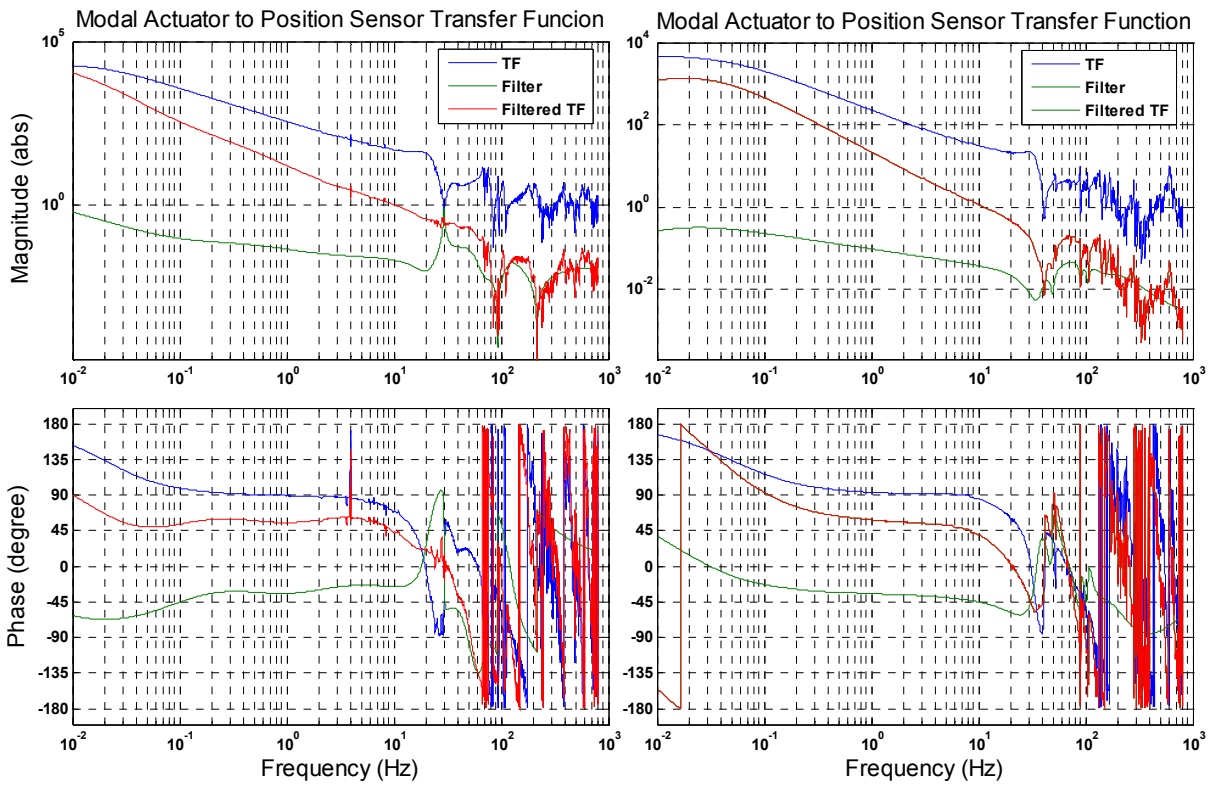

Figure 3.13. Synthesized ETMX RX (left) and VO (right) modal actuator to position sensor transfer functions. Also see Figure 3.8, the equivalent transfer functions obtained here are from point **i** to **g**, while breaking the loop immediately after **g**. The transfer functions are then reshaped by compensators, shown in green. The filtered transfer functions, shown in red, are equivalent to point **i** to **i**, or a loop transfer function.

After HEPI structure was fully assembled, we did not take note of the initial position of these two modes, and it was unclear the assembled state is stress/deformation free (we did use a lot of shims). Therefore, there was no clear stress free or zero-deformation reference point, making controlling these two modes at DC meaningless.

We later discovered very low frequency oscillation in the over-constrained DOFs in some tanks (see Section5.3). How this oscillation affects the payload motion in other DOFs and the detector as a whole was not well understood, and controls for these modes were disabled.

Similarity among BSC tanks

Among the BSC tanks the transfer functions of equivalent actuator-sensor pairs bear great resemblance, hence the position sensor filter, geophone sensor filter, and the compensator filter

designs for other tanks do not vary much. Unfortunately, the amount of variation is enough to require hand-tuning.

3.2.1 Feed-forward

In doing feed-forward one commands the system at the error point of the position sensor loop (point **b** of Figure 3.8) to cancel the effects of ground motion. The goal is to quiet the payload supported by HEPI (point **m** Figure 3.8).

According to Equation 3.1,

$$\frac{m}{Gr} = \frac{TF_{gb} + TF_{gh}G_p - G_s(G_p/S_p)}{1 + G_g + G_p}.$$

Assuming the only noise source is from the ground, one can minimize $\left|\frac{m}{Gr}\right|$ by letting,

$$G_s = \frac{S_p(TF_{gb} + TF_{gh}G_p)}{G_p}. \qquad \text{(Equation 3.4)}$$

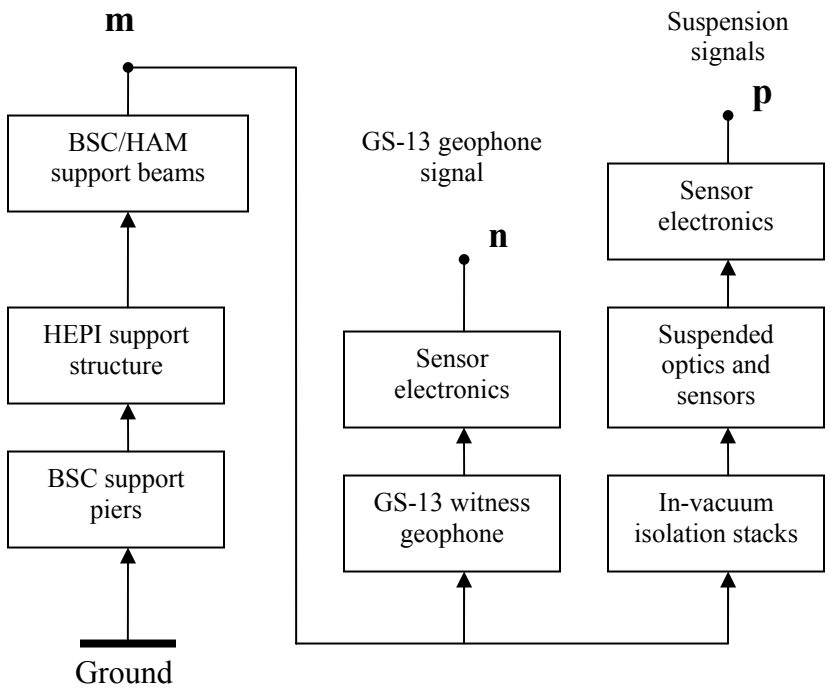

Figure 3.14. Using the GS-13 geophone to gather BSC and HAM feed-forward data. This figure is an extension to Figure 3.8.

The desired STS-2 filter F_s is then

$$F_s = \frac{G_s}{S\,M_s} = \frac{S_p(TF_{gb} + TF_{gh}\,G_p)}{S\,M_s\,G_p}. \qquad \text{(Equation 3.5)}$$

TF_{gh} can be difficult to measure due to the mechanical complexity, however the TF_{gb}+$TF_{gh}G_p$ term can be resolved by doing the following two things while the position and geophone sensor loops are closed and the signal is cut-off right after point **j** : (1) driving at point **k** and measuring the payload motion signal at point **m**, which ideally would yield

$$\frac{m}{k} = \frac{M_s\,(G_p/S_p)}{1 + Gg + G_p}, \qquad \text{(Equation 3.6)}$$

and, (2) measuring the ground signal **j** to point **m** transfer function, which ideally would be

$$\frac{m}{j} = \frac{TF_{gb} + TF_{gh}G_p}{S\,(1 + G_g + G_p)}. \qquad \text{(Equation 3.7)}$$

The ratio between the two

$$\frac{k}{j} = \frac{S_p\,(TF_{gb} + TF_{gh}G_p)}{S\,M_s\,G_p}, \qquad \text{(Equation 3.8)}$$

is exactly the desired F_s.

The payload motion signal, **m**, is measured by a pair of witness GS-13 geophones placed separately on the two support beams (see Figure 3.2 and schematic diagram Figure 3.14). They can be oriented in the X ,Y, or Z directions as desired. A pair is needed so that after the signal from the two geophones is combined, the rotational motion signal may be cancelled out, leaving only a linear motion payload signal. Since the signal at point **b,** where one drives HEPI, has a dimension of displacement, and the GS-13 geophone and the STS-2 seismometer measure acceleration and velocity, respectively, one expects the data gathered for Equation 3.6 and 3.7 should have strong f^2 and f dependence. As a result the data for Equation 3.8 should have strong 1/f dependence. In reality the data deviates somewhat from 1/f dependence, since according to

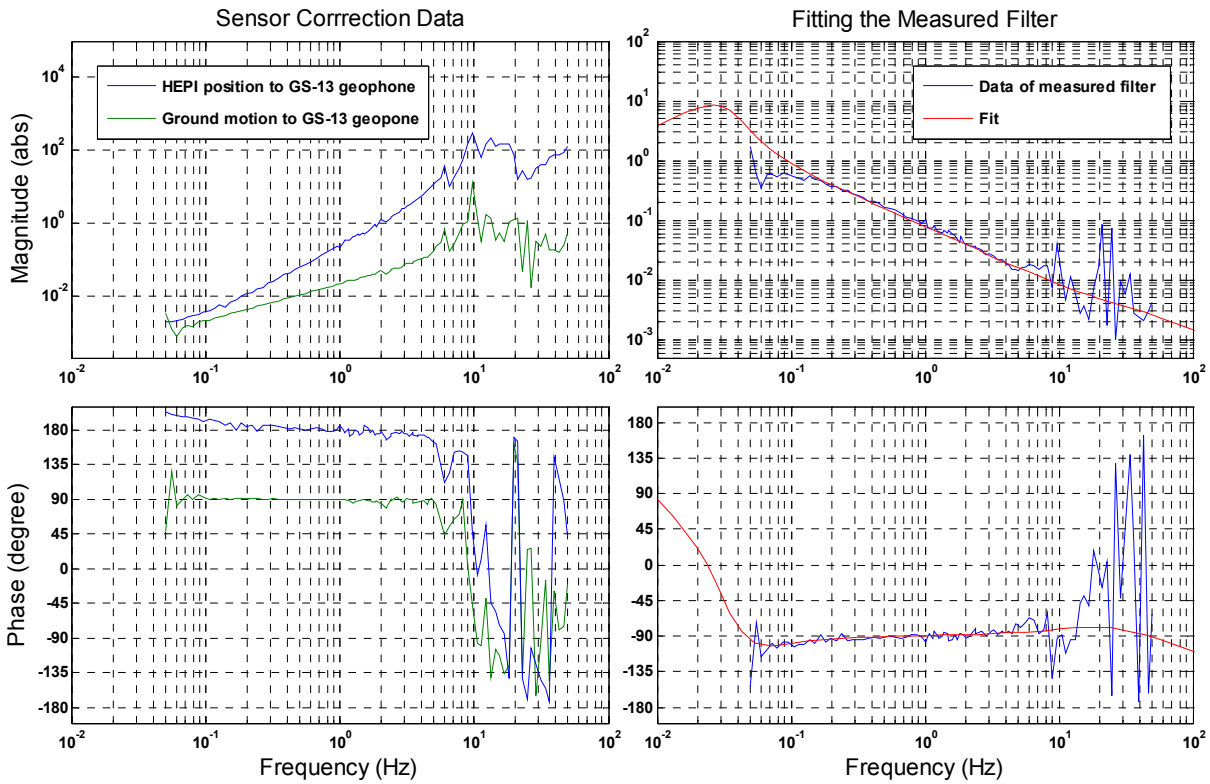

Figure 3.15. Measuring the ETMX X DOF STS-2 filter. Transfer functions shown in left panels are data for Equation 3.6 and 3.7. Right two panels, the ratio between the two transfer functions is the STS-2 filter sought after, or Equation 3.8. Also shown in red is a manual fit to the data.

Equation 3.8 it bears the signatures of STS-2 response S, loop transfer function $G_{p,}$ and transfer functions TF_{gb} and TF_{gh}. For example see Figure 3.15.

Empirically the ground motion signal below 0.1Hz is contaminated by ground tilt and low-frequency thermal effects. To avoid the tilt-contaminated ground signal being feed-forwarded into the system and generate unwanted payload motion, we high pass the signal below 0.1Hz with a roughly f dependence curve. Fitting the data between 0.1 and 10Hz perfectly with an IIR filter would be challenging, partially because we are making the fit the inverse of the STS-2 response (a real physical response) above 0.1Hz while forcing it to high pass below 0.1Hz. If we were to inverse the STS-2 response below 0.1Hz, there would be a pair of complex zeros at 0.0083Hz (Figure 3.7), below which the signal is low passed.

We pursued a different strategy to filter out the tilt-contaminated ground signal. We used an FIR high pass pre-filter (Figure 3.16), designed by W.Hua [31], before the STS-2 filter in the signal chain. Such a filter has a f^2 roll-off below 0.04Hz, and between 0.1 and 1Hz the gain is one and the phase is zero. Together with the STS-2 filter, the signal below 0.04Hz rolls off roughly as f^3, and because of STS-2's own response, the signal below 0.0083Hz rolls of as f^5. Assuming the tilt component is $1/f^2$ proportional to the horizontal signal, below 0.04Hz it is still attenuated as f, and below 0.0083Hz as f^3. The signal is not altered between 0.1 and 1Hz, and the STS-2 filter we designed in Figure 3.15 remains effective. These two properties come with a price of a bump between 0.04 and 0.1Hz, and the bump manifest itself in the ground to suspended optics transfer function (see Section 3.3), posing challenges to interferometer length control. FIR was chosen for the high pass pre-filter, because even to generate a filter close to such shape with an IIR filter would require an impractically large number of poles and zeros. The $1/f^2$ proportionality of the tilt motion signal to the horizontal motion signal is derived in Section 3.4.1.

The STS-2 Z direction signal is not filtered by the high pass FIR filter before it is filtered by the STS-2 filer $\mathbf{F_s}$, because for small ground tilt angle the effect is less on a seismometer test mass in the Z direction. The tilt induces an extra force that is proportional to the tilt angle on the seismometer test mass in the horizontal direction, but proportional to the tilt angle squared in the vertical direction.

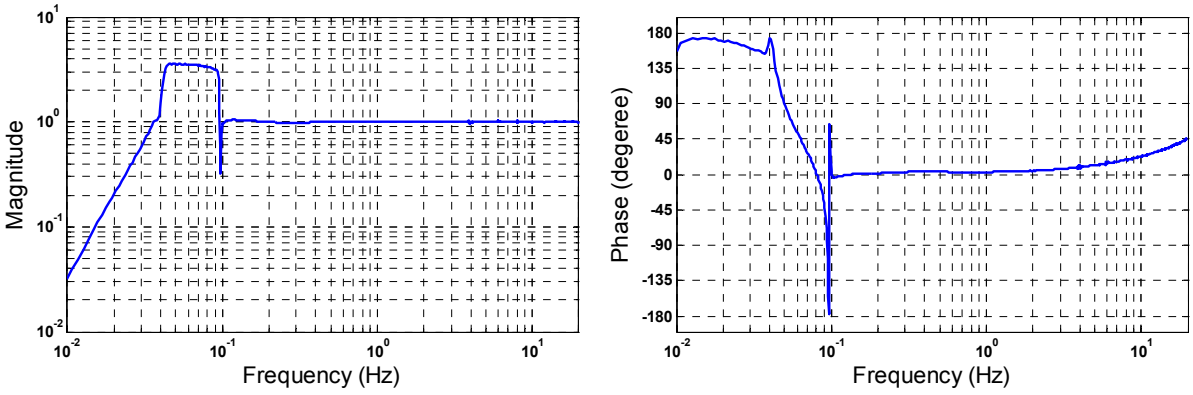

Figure 3.16. FIR high pass filter.

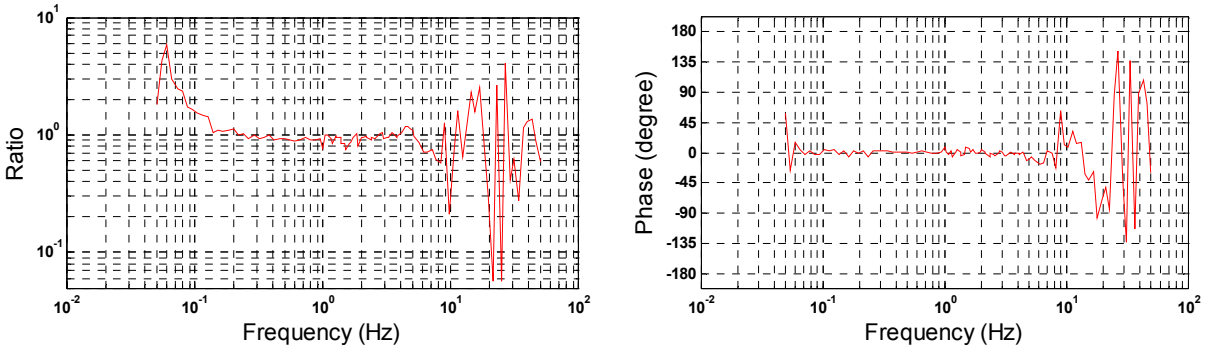

Figure 3.17. Ratio between the fit and the measured STS-2 filter for ETMX X DOF. This is another limiting factor of how well feed-forward performs.

How well can we expect feed-forward to perform? Define ε as the ratio of the fit over the measured STS-2 filter k/j (Figure 3.17), and the fit described as,

$$\frac{\varepsilon\, k}{j} = \frac{\varepsilon\, S_p\,(TF_{gb} + TF_{gh} G_p)}{S\, M_s\, G_p}, \qquad \text{(Equation 3.9)}$$

then,

$$G_s = \frac{\varepsilon\, S_p\,(TF_{gb} + TF_{gh} G_p)}{G_p}. \qquad \text{(Equation 3.10)}$$

One can evaluate the ground to payload transfer function,

$$\frac{m}{Gr} = \frac{(TF_{gb} + TF_{gh} G_p)\,(1-\varepsilon)}{1 + G_g + G_p} = \frac{m\, S\,(1-\varepsilon)}{j}. \qquad \text{(Equation 3.11)}$$

3.2.2 The Resonant Gain Filter Technique

The resonant gain filter (RGF) technique is widely used in LIGO system controls. The basic idea is the following: at the desired frequency where the loop gain is G_l, elevate the control gain by another factor of G_r, so that the total disturbance suppression factor becomes, $1 / (1 + G_l\, G_r)$. If it were added to the geophone sensor feedback loop in HEPI, the effect would be to more effectively suppress the payload motion. On BSC tanks, the RGFs are added to the position and geophone sensor filters. On HAM tanks, we did not implement these filters, due to the difficulties we encountered when adding geophone sensors to the feed back (see Section 3.4).

A RGF consists of a pair of complex poles and a pair of complex zeros, located at the same frequency but with different damping factors. Mathematically it can be expressed as,

$$Rg = \frac{s^2 + 2\beta_2\omega_0 s + \omega_0^2}{s^2 + 2\beta_1\omega_0 s + \omega_0^2}, \qquad \text{(Equation 3.12)}$$

where β_1 and β_2 and are the damping factor of the paired pole and zeros, $\omega_0=2\pi f_0$, and f_0 is the frequency at which the filter is implemented. The filter will have exact height of $G_r = \beta_2 / \beta_1$ and width characterized by β_1. As the height increases β_1 gets more accurately proportional to the full width at half maximum (FWHM) of the filter. An example of this filter is depicted in Figure 3.18. A RGF introduces a rapid gain and phase change just before and after frequency f_0, but sufficiently far away from f_0 the gain and phase are not affected. This property is desirable because at the frequency other than where the filter implemented, the control loop gain and phase is not altered, and hence control loop stability is maintained. At the resonant gain frequency since the gain is high, according to Equation 3.3, the system remain stable. It is possible to have the height G_r less than one, in such case the RGF resembles a notch filter (Figure 3.18). In fact, at above 1Hz where the performance of feed-forward start to degrade, RGFs of $G_r << 1$ were implemented in the position sensor feedback loops at the stack mode frequencies, to give the geophones full control authority. See Figure 3.19.

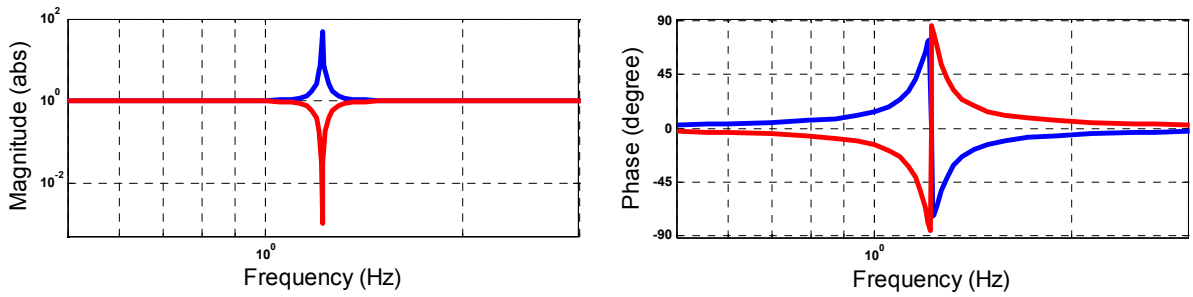

Figure 3.18. A pair of RGFs at 1.2Hz. Blue trace shows one with height of 50 and width of 0.001, red trace with height of 0.001 and width of 0.05.

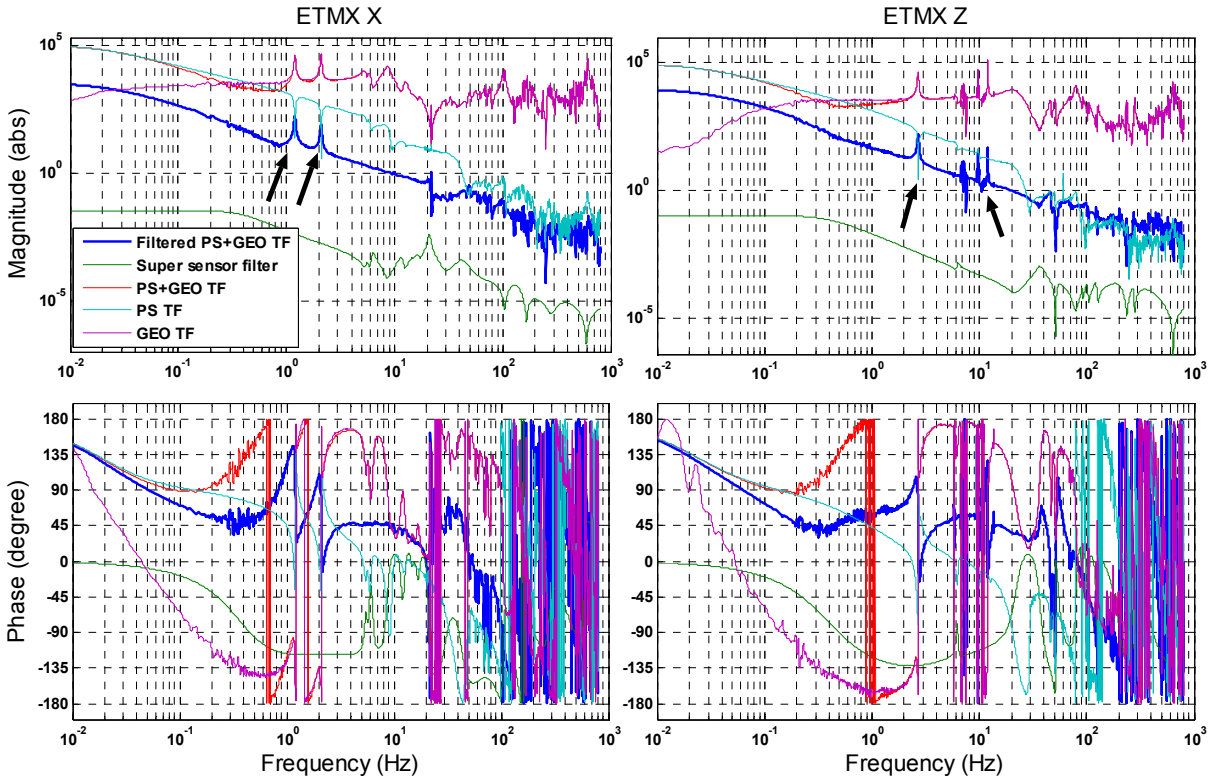

Figure 3.19. Example of RGFs implemented in the ETMX tank. Indicated by the bold black arrows, are the1.2Hz and 2.1Hz RGFs in the X DOF, and 2.7Hz and 12Hz in the vertical DOF. Loop stability is maintained by obeying Equation 3.3.

We experimented implementing RGFs at the low order mechanical resonant frequencies of the payload supported above the BSC HEPI structure. For any LLO suspended large optic, the low order mechanical resonances are the pendulum (~0.76Hz), side pendulum (~0.73Hz), pitch (~0.63Hz), yaw (~0.5Hz), bounce (~12Hz), and roll (~18Hz) modes. The typical low order stack modes are the 1.2Hz and 2.1Hz horizontal, and the 2.7Hz vertical modes.

Typical RGFs we tested at the pendulum, side pendulum, pitch, yaw modes have height of 100 and $\beta_1 = 2.5\times10^{-5} \sim 10\times10^{-5}$ in the horizontal geophone sensor loop. They performed well (Figure 3.20), but it was later realized they impair interferometer cavity length control in a way that is still not fully understood. It was speculated that engaging the RGFs increases the coupling from HEPI horizontal motion to suspended optics pitch motion. For example, see [32].

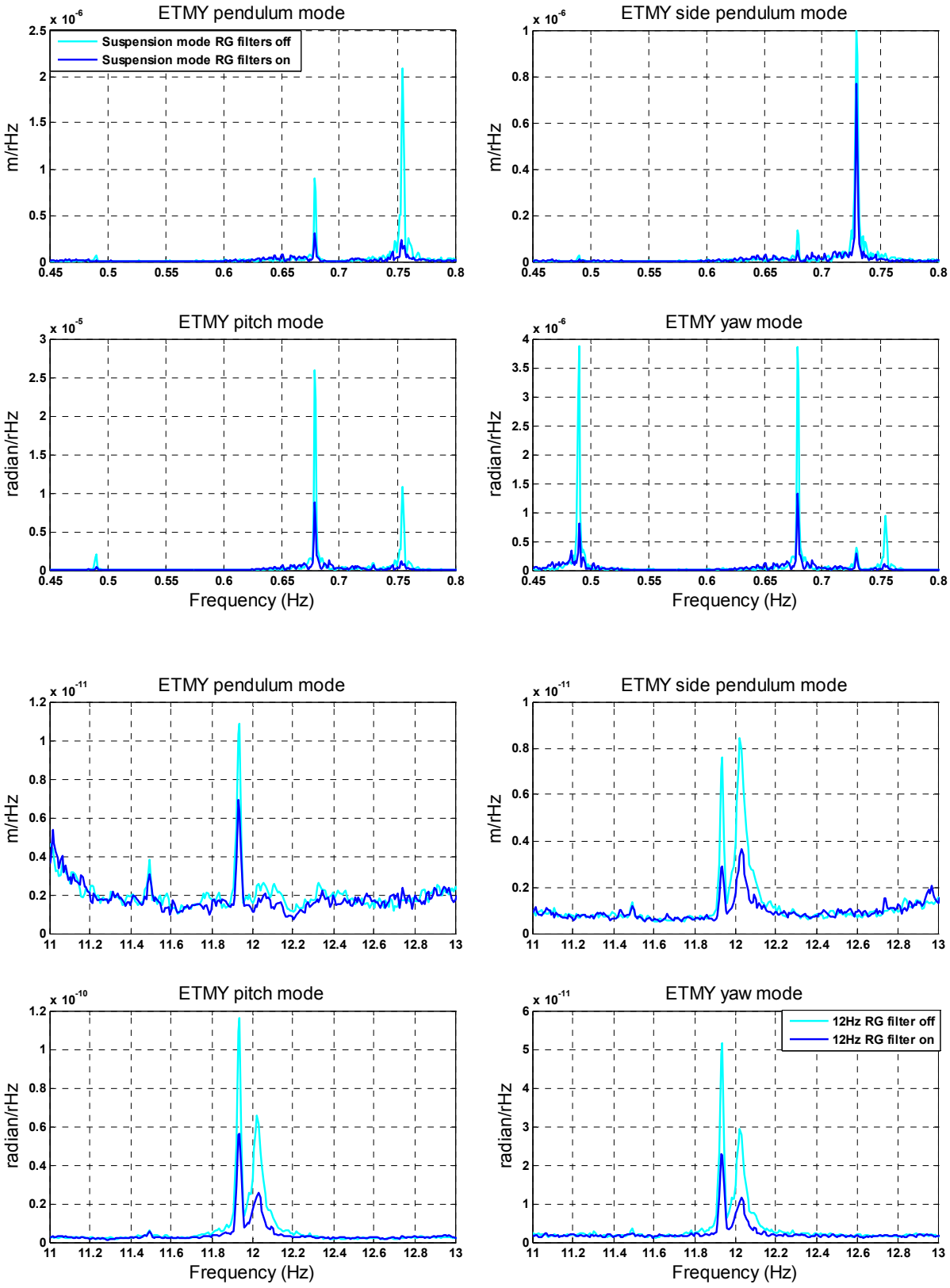

Figure 3.20. Experimenting RGFs at the ETMY test mass pendulum (0.756Hz), side pendulum (0.730Hz), pitch (0.678Hz), yaw (0.490Hz), and bounce (12.03Hz) suspension modes. Local damping of the test mass was disabled when doing this test.

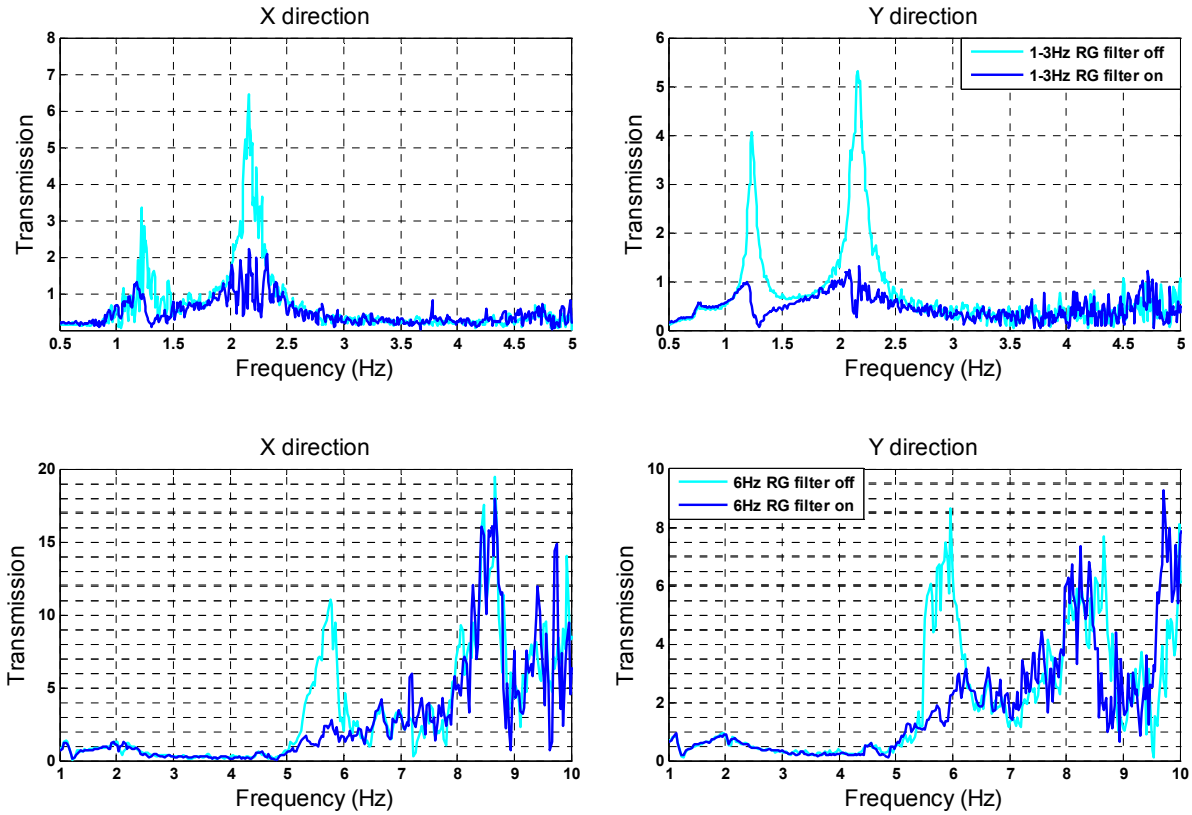

Figure 3.21. Experimenting RGFs to reduce the ground to optics table transmission at the ITMX primary, secondary, and 3rd stack modes at 1.24, 2.16, and 5-7Hz.

Typical RGFs we tested at the 12Hz suspension bounce mode have height of 50 and $\beta_1 = 5\times10^{-4}$ in the vertical geophone sensor loop, and performed quite well. It is possible to implement RGF at this relatively high frequency, because typically this mode only has a width of less than 0.1Hz. The gain and phase change caused by a RGF of this width is small at the ugf and will not affect loop stability. We gauge the RGF implemented by looking at the pendulum, side pendulum, pitch, and yaw mode signals, since there is no sensor that directly measures test mass bounce. Discovered in May, 2006, the ETMY suspension bounce mode exhibits double resonant peaks. This is most likely due to the slight difference in the lengths and spring constants of the suspension wires on each side of the test mass was large enough to cause the resonant frequencies to be distinguishable. We implemented a double RGF to suppress it (Figure 3.20).

For the stack modes, typical RGFs we tested have height of 10 and β_1 =0.01 in the geophone sensor loop, and height of 0.001 and β_1 =0.05-0.1 in the position sensor loop. Decent suppression is obtained from the filters between 1 and 3Hz (see Figure 3.21). Although it is achievable to implement RGF at the third stack mode around 5-7Hz, it is less well studied and in some tanks the suppression effect is marginal. Often, adjacent to the frequency where it is implemented the noise gets worse slightly. It is increasingly difficult to implement RGF of this quality beyond the third stack mode due to insufficient control loop gain.

For S5 run we only operated the filters at the 1.2, 2.1Hz horizontal and 3Hz vertical stack modes and also the 12Hz suspension bounce modes. The filters were able to reduce the 1-3Hz rms ground to optics table transmission roughly by a factor of 1.8 to 3.2 in the X and Y direction, and 1.1 to 1.8 in the Z direction. Bounce mode motion were reduced by a factor 1.4-2.5 in some tanks. Table C.1 in Appendix C lists the precise resonant frequencies where the filters were implemented [33]. Table C.2 lists the rms noise suppression obtained from the filters on all BSC tanks during S5 run.

3.3 Isolation Performance of Basic Symmetric Chamber

We evaluate the isolation performance of HEPI in the X, Y, and Z DOFs by measuring the transmission from the ground to the support cross beam, whose motion is sensed by the HEPI geophones, and the transmission from the ground to optics table, whose motion is sensed by the suspended optic signals. Performance in the RX, RY, and RZ DOFs is measured in angular motion by the HEPI geophones, suspended optic signals, and the optical lever signals. See Figure 3.22. HEPI performance does not vary much among different BSCs, due to their high degree of structural and HEPI control configuration resemblance. Performance of all BSC tanks is tabulated in Table C.3-C.5 in Appendix C.

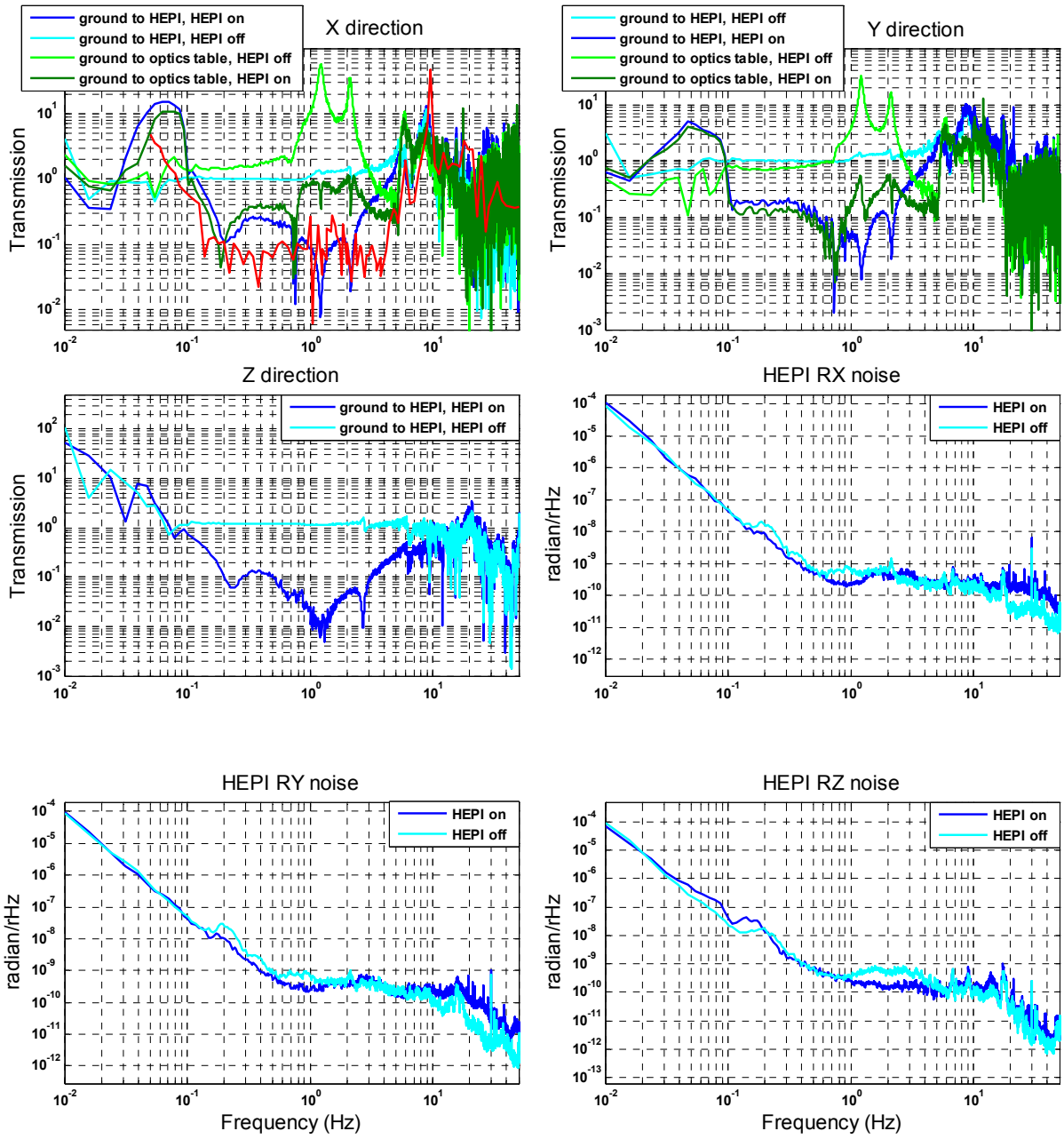

Figure 3.22. Isolation performance of ETMX during the S5 run. Prediction for the ground to HEPI transmission in the X direction, is plotted in red trace, according to Equation 3.11, but not considering the implemented RGFs. Note in X and Y direction, the cancellation effect of the first and second stack modes and the RGFs implemented at these modes. The net effect is that little to none isolation is provided by HEPI and the isolation stacks altogether in the 1-3Hz band. Also a clearly visible feature in the horizontal ground to optics table transmission, and in the angular motion of the optic, is the excess noise in the sub-0.1Hz region due to the implemented high pass FIR filter described in Section 3.2.1.

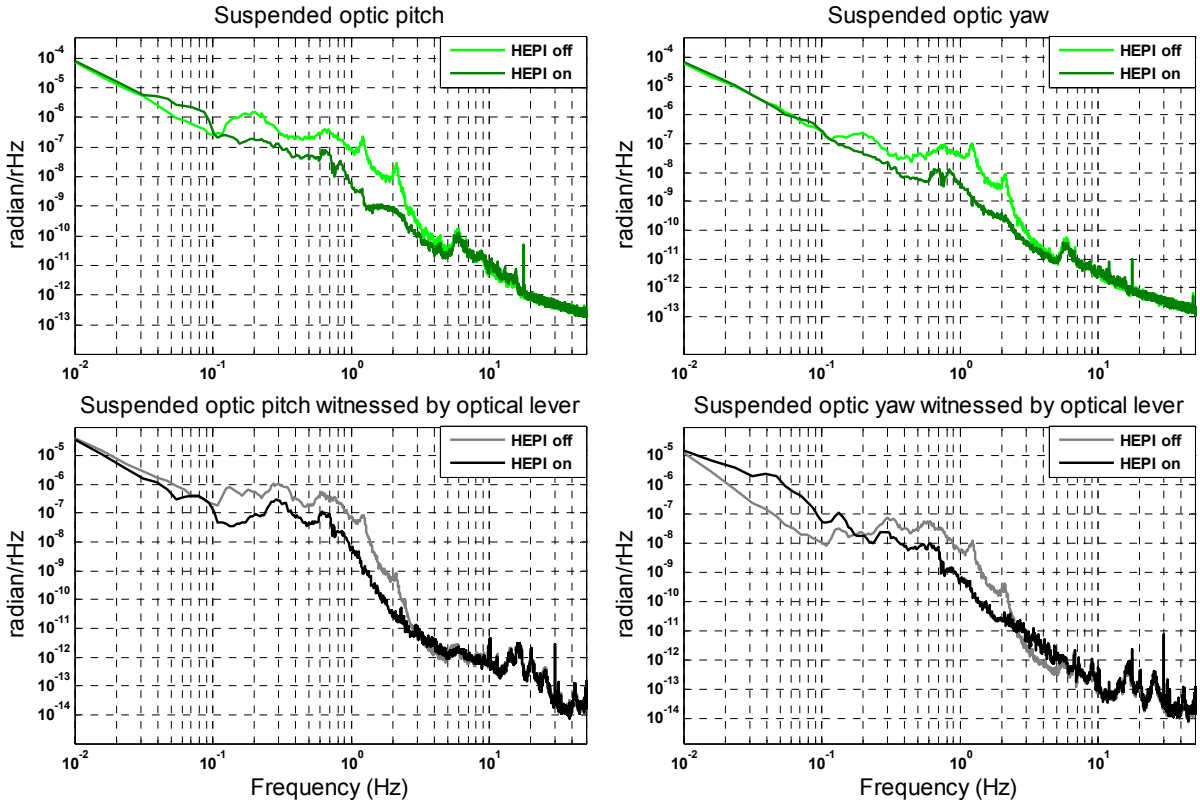

Figure 3.22 continued.

3.4 Control Scheme of HEPI on Horizontal Access Modules (HAM)

We obtained the system identification data and determined the actuator normalization factors for the HAMs in the same fashion as in the BSCs. Modal sensor signals and actuator signals are also processed in the same way.

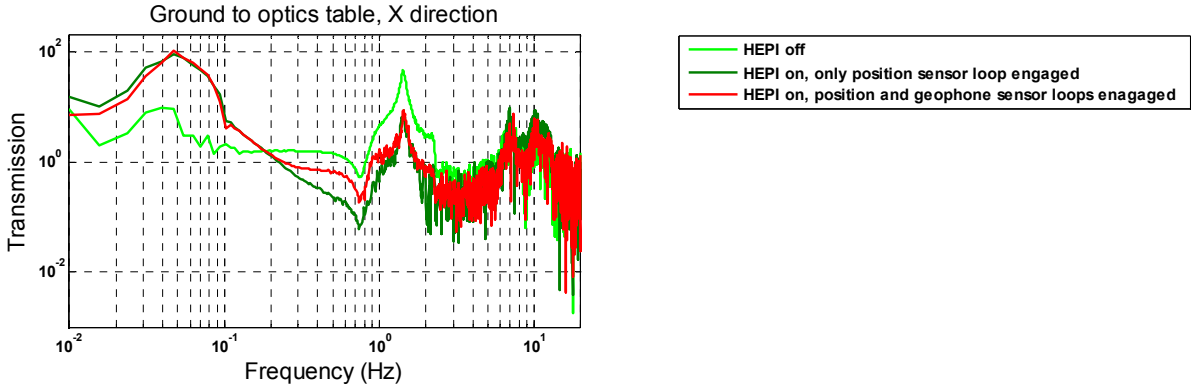

Figure 3.23. Isolation performance of HAM1 in the beamline direction, showing serious compromise below the microseism band due to tilt in the RY DOF.

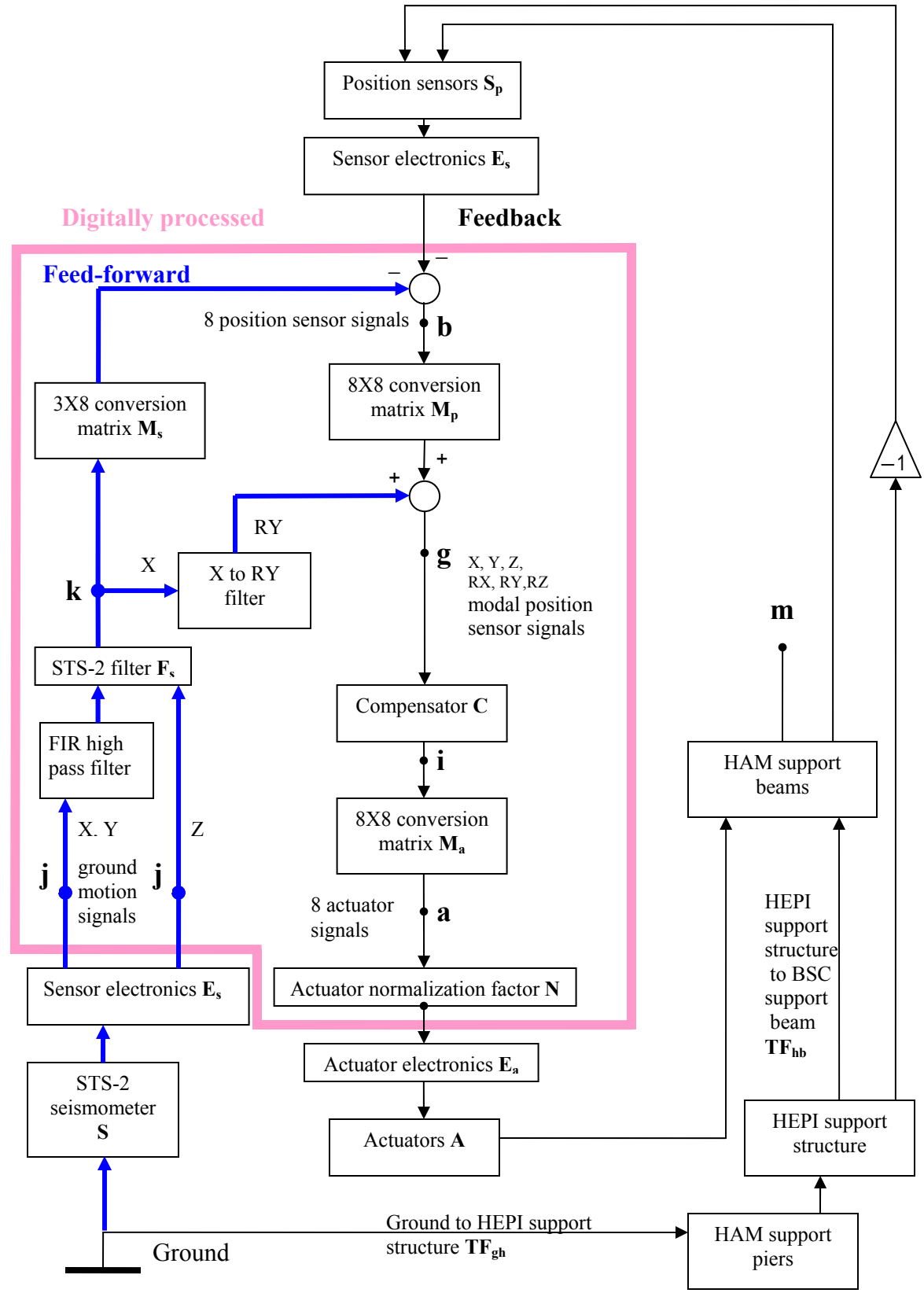

Figure 3.24. Schematic diagram of HAM HEPI system.

Employing the same control scheme used in the BSCs on the HAMs does not yield performance close to that seen in the BSCs. We discovered a tilt motion is induced [34, 35, 36] when the support payload is actuated in the beamline direction (X direction for HAM1~3 and Y for HAM4). The L-4C geophones sense the tilt motion, and incorporating them in the feed-back loop introduces extra noise. Also see Chapter 5 on this issue. Falling back to a more conservative plan that utilizes only the position sensors in the feedback and also feed-forward yields better results. See Figure 3.23. A tilt correction path (X to RY for HAM1~3 and Y to RX for HAM4) is added parallel to the feed-forward path rectify the tilt problem, see Figure 3.24 above and Section3.4.1.

Two types of control schemes were employed on the HAMs, the control of translational DOFs, X,Y, and Z, and of rotational DOFs, RX, RY, and RZ.

X, Y, and Z DOFs

For these DOFs, we utilize the position sensors in the feedback, and feed-forward to suppress payload motion.

Similar to BSCs, but dropping the G_g term in Equation 3.1, the ground motion to support beam motion transfer function is,

$$\frac{m}{Gr} = \frac{TF_{gb} + TF_{gh} G_p - G_s(G_p/S_p)}{1 + G_p}. \qquad \text{(Equation 3.13)}$$

System stability is still described by Equation 3.3, but with G_g=0, and G= G_p,

$$\frac{1}{1+G} < \infty .$$

Again we allow ~45 degree of phase margin at and below the unity gain frequency (ugf), and a factor of 3 of gain margin above the ugf.

The compensator design for the HAMs is slightly different partially due to the fact the HAM stacks are different to the BSCs. Below 10Hz the modes that can be easily compensated are the

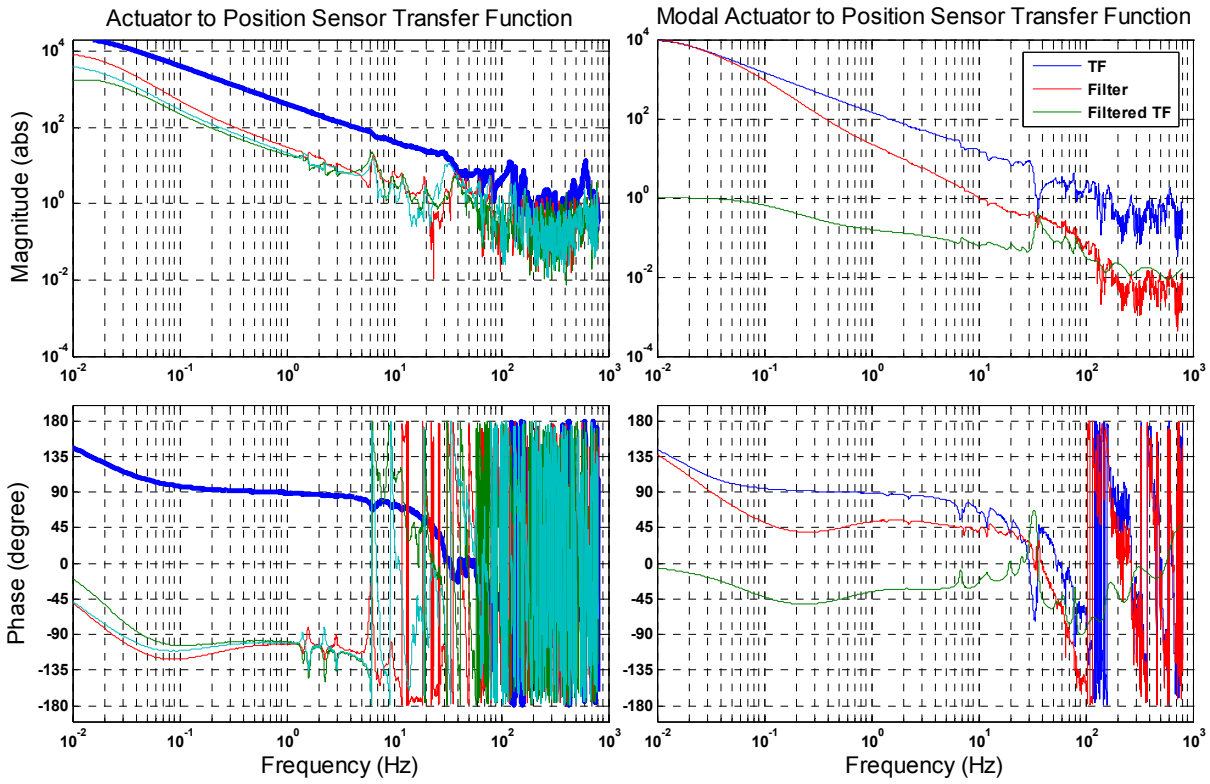

Figure 3.25. Left two panels: HAM1 H1 actuator to horizontal position and geophone sensor transfer functions. Also see Figure 3.24, the transfer functions obtained here is equivalent to driving at point **a** and measuring the response at point **b**, while breaking the loop immediately after **b**. Transfer functions of co-located actuator-sensor pairs have highest response, shown as bolded blue traces. Right two panels: X DOF modal horizontal actuator to position sensor transfer function. The equivalent transfer functions obtained here is from point **i** to **g**, while breaking the loop immediately after **g**. The transfer function is then reshaped by the compensator, shown in green. The filtered transfer function, shown in red, is equivalent to point **i** to **i**, or a loop transfer function.

beamline direction transfer modes at roughly 1.5, 2.3, 7.2, 7.7, and 10Hz, the transverse to the beamline direction horizontal-horizontal transfer modes at roughly 1.6, 2.8, 7.3, 8, and 10Hz, and the vertical-vertical transfer modes at roughly 3.2 and 7.8Hz. As in the BSCs, at 20 to 60 Hz, the actuator bellow expansion mode, actuator tripod compression mode, and support beam flexing modes are still present [37]. Probably fewer problems arise from the support pier mode, because the HAM support piers are far shorter, and therefore stiffer than the BSC ones. It is still very hard to compensate perfectly above 20Hz, so we conservatively set the ugf at around 10Hz, and attenuate the signal above 60Hz (Figure 3.25).

RX, RY, and RZ DOFs

These DOFs are controlled only by the position sensor feed-back loops, with loop design principles identical to the RX and RY DOFs in the BSCs.

HO, VO DOFs

These two modes are left uncontrolled.

3.4.1 Feed-forward

While feed-forward in the Y and Z direction were carried out in the same fashion as in the BSCs, feed-forward in the X required a correction in the RY that is linearly proportional to the amount actuated in X.

Refer to Equation 3.13, one minimizes the ground motion to support beam motion transfer function $\left|\frac{m}{Gr}\right|$ by letting,

$$G_s = \frac{S_p(TF_{gb} + TF_{gh}G_p)}{G_p}. \qquad \text{(Equation 3.14)}$$

The desired STS-2 filter F_s is then

$$F_s = \frac{G_s}{S M_s} = \frac{S_p(TF_{gb} + TF_{gh}G_p)}{S M_s G_p}. \qquad \text{(Equation 3.15)}$$

Again with the feedback loops closed and the signal cut-off right after point **j**, one obtain the STS-2 filter F_s by, (1) driving at point **k** and measuring the payload motion signal at point **m**, which ideally would yield

$$\frac{m}{k} = \frac{M_s (G_p/S_p)}{1 + G_p}, \qquad \text{(Equation 3.16)}$$

and, (2) measuring the ground signal **j** to point **m** transfer function, which ideally would be

$$\frac{m}{j} = \frac{TF_{gb} + TF_{gh}G_p}{S(1 + G_p)}. \qquad \text{(Equation 3.17)}$$

The ratio between the two

$$\frac{k}{j} = \frac{S_p\,(TF_{gb} + TF_{gh}G_p)}{S\,M_s\,G_p}, \qquad \text{(Equation 3.18)}$$

is exactly the desired F_s.

When gathering the data for Equation 3.16, one expects that the data should have a strong f^2 dependence since the GS-13 geophone measures acceleration and we are driving at point **k** which is in unit of displacement. But in fact below 1Hz the data starts to deviate from f^2. This behavior is also confirmed by HEPI's L-4C geophone and the suspended optic signals (Figure 3.26). This behavior can be explained by assuming all the witnesses, namely GS-13, L-4C, and the suspended optic, are all simple driven damped oscillators, and adding simple tilt term that is proportional to the amount of X drive in HEPI. This will add an additional term that is $1/f^2$ times the original tilt-free HEPI X to witness instrument transfer functions.

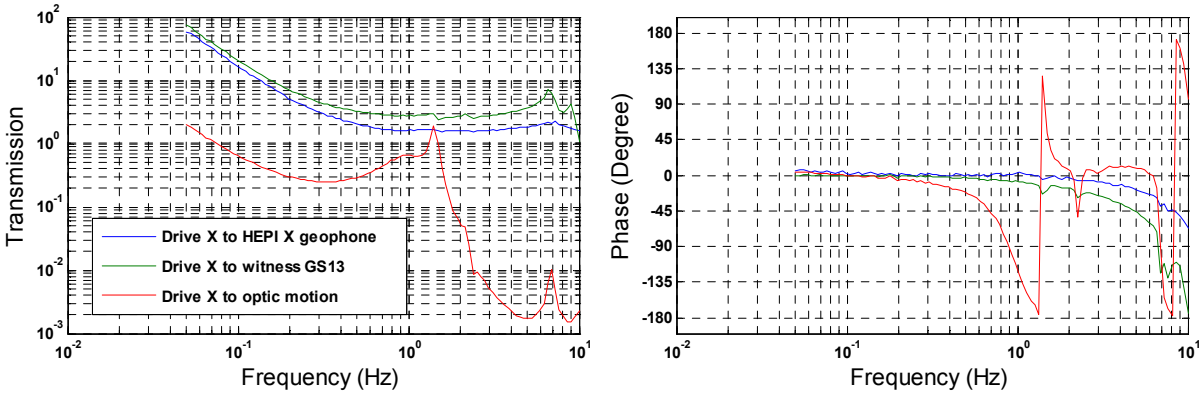

Figure 3.26.Measured transfer function of driving HAM1 X DOF to various witness sensors. Visible at below 0.5Hz, which is below the lowest suspension and stack resonant modes, the magnitude of the transmission deviates from a constant and increases as it goes to lower frequency, while the phase remains at close to zero, is where the tilt effect dominates. Without the tilt effect, the test masses in the witnesses would have followed the drive, and the magnitude of the transmission should have been constant.

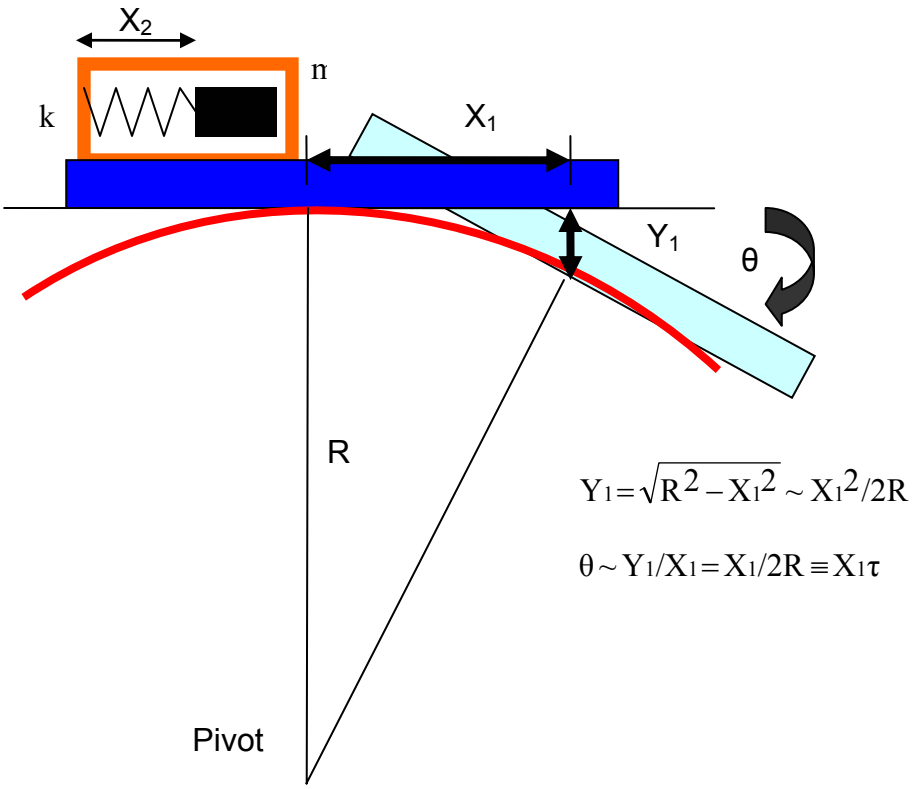

Figure 3.27. A simple model to explain the extra tilt signal observed. Assuming the HAM support table rotates about a fixed pivoting point at a fixed radius of R when actuated in the X direction. The amount of tilt θ is proportional to X_1 if X_1 is small.

Based on the model depicted in Figure 3.27, one can estimate the transfer function of HAM HEPI support beam motion to various witness sensor signal as follows. Assume the sensor is a simple damped spring-mass system, with test mass m, damping b, and spring constant k. The motion of the support beam X_1, motion of the test mass in the sensor X_2. The amount of tilt $\theta = \tau$ X_1. The tilt induces an extra force on the test mass along the spring axis, and hence an extra mθ term in the equation of motion:

$$m\ddot{X}_2 + b(\dot{X}_2 - \dot{X}_1) + k(X_2 - X_1) - m\tau X_1 = 0. \qquad \text{(Equation 3.19)}$$

Solving the equation by Laplace Transform,

$$\frac{X_2}{X_1} = \frac{bs + k + m\tau}{ms^2 + bs + k}. \qquad \text{(Equation 3.20)}$$

Since the witness sensors measure $X_2 - X_1$,

$$\frac{X_2 - X_1}{X_1} = \frac{m(\tau - s^2)}{m s^2 + b s + k}. \qquad \text{(Equation 3.21)}$$

The ground motion to sensor signal transfer function has an extra $\frac{m\tau}{m s^2 + b s + k}$ term which is $1/f^2$ proportional to the tilt-free solution $\frac{-m s^2}{m s^2 + b s + k}$.

Rewrite Equation 3.21 in generalized form:

$$TF(X \rightarrow GS13X)_{real\ word} = TF(X \rightarrow GS13X)_{ideal} + TF(X \rightarrow RY) * TF(RY \rightarrow GS13X), \qquad \text{(Equation 3.22)}$$

where $\frac{X_2 - X_1}{X_1}$ corresponds to $TF(X \rightarrow GS13X)_{real\ word}$, $\frac{-m s^2}{m s^2 + b s + k}$ to $TF(X \rightarrow GS13X)_{ideal}$, $\frac{m}{m s^2 + b s + k}$ to $TF(RY \rightarrow GS13X)$, and τ to $TF(X \rightarrow RY)$.

The first term in the parenthesis denotes the drive, while the second the sensor. For example $TF(X \rightarrow GS13X)$ represents the transfer function of driving X to GS-13X sensor. The subscripts denote either the 'real world' situation where there is cross coupling between different DOFs, or 'ideal' situation where cross coupling is absent.

Placing the GS-13 sensors vertically (Figure 3.3) on both HAM support beams while driving HEPI in X allows one to measure the extend of tilt effect. One can derive similar equation as Equation 3.22,

$$TF(X \rightarrow GS\text{-}13RY)_{real\ word} = TF(X \rightarrow GS\text{-}13RY)_{ideal} + TF(X \rightarrow RY) * TF(RY \rightarrow GS\text{-}13RY). \qquad \text{(Equation 3.23)}$$

$TF(X \rightarrow GS13X)_{real\ word}$, $TF(X \rightarrow GS\text{-}13RY)_{real\ word}$, $TF(RY \rightarrow GS13X)$, and $(RY \rightarrow GS\text{-}13RY)$ are measurable quantities. $TF(X \rightarrow GS\text{-}13RY)_{ideal}$ is zero based on the assumption that cross coupling is zero between different DOF in ideal world. Following this the $TF(X \rightarrow GS13X)_{ideal}$

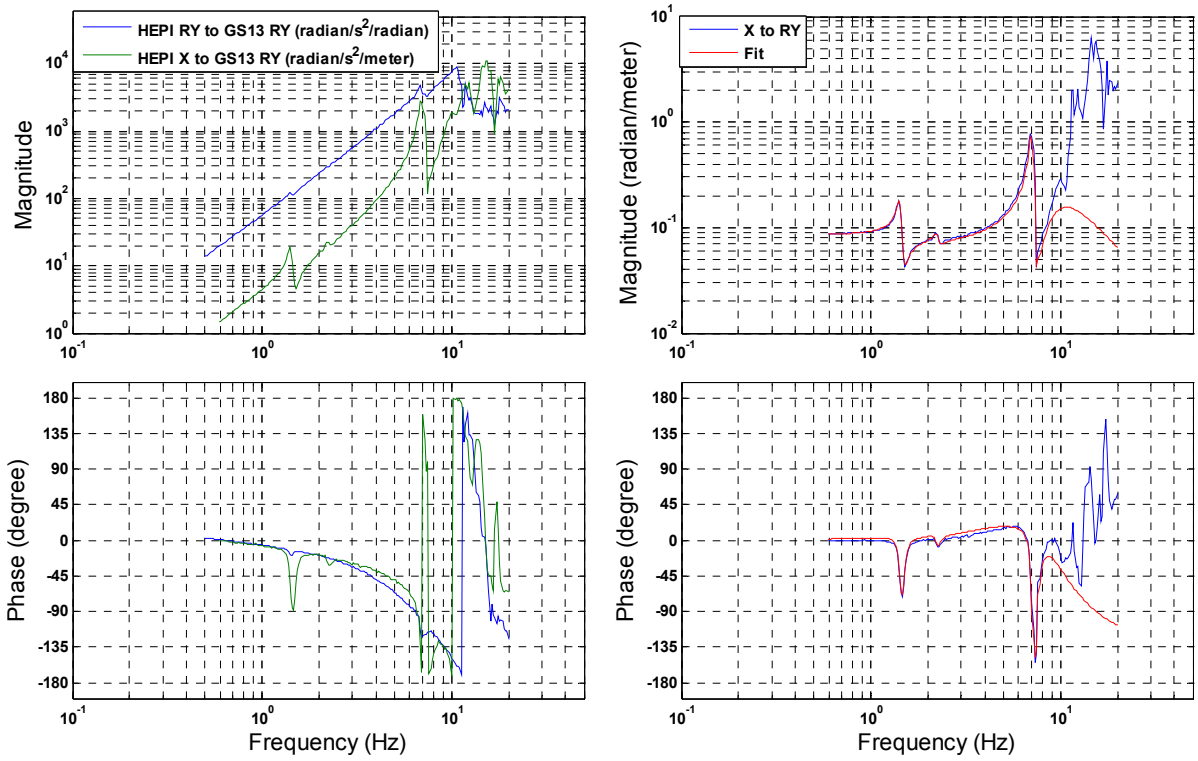

Figure 3.28. Measuring the HAM1 STS-2 X to RY correction filter. Left two panels show the transfer functions of HEPI X to GS-13 RY geophone (Equation 3.23), and the HEPI RY to GS-13 RY. Right two panels, the ratio between the two transfer functions, TF(X→RY), is the X→RY correction filter sought after in Figure 3.24. Also shown in red is the fit to the data. As expected in the model in Figure 3.27, the correction approaches constant at below 1Hz, below all stack resonant modes. The fit only attempts to match the data to the lower stack modes below 10Hz.

and TF(X→RY) terms can be resolved, see Figure 3.28. One further assumes the reverse of TF(X→RY), which is TF(RY→X), is zero to first order, so that driving RY does not yield similar pair of equations as above and adds additional unknown variables to the system.

Once $TF(X\rightarrow GS13X)_{ideal}$ and TF(X→RY) terms are resolved, $TF(X\rightarrow GS13X)_{ideal,}$ which represents the data for Equation 3.16, along with data collected for Equation 3.17, can be used to resolve the STS-2 filter Fs described in Equation 3.18, while TF(X→RY) is the tilt correction filter to be inserted into the X to RY filter in Figure 3.24. See Figure 3.29 for the resolved STS-2 filter data, and Figure 3.30 for closeness of the fit.

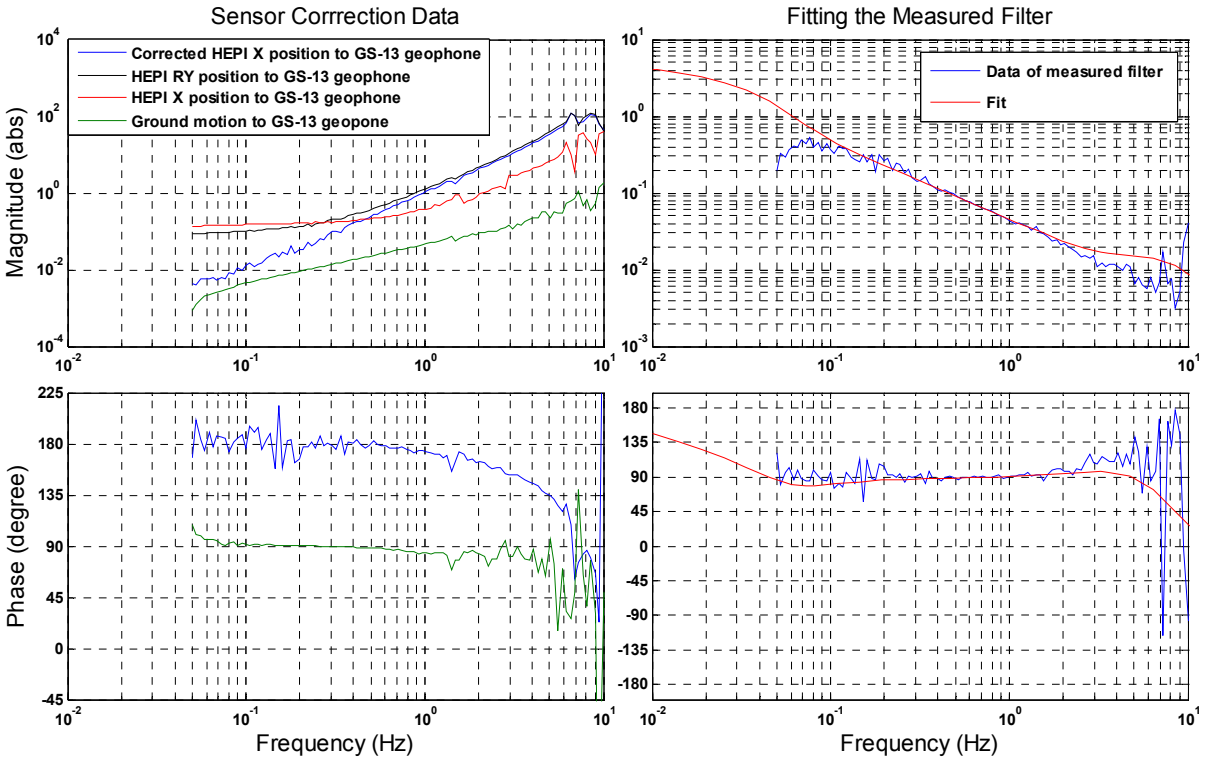

Figure 3.29. Measuring the HAM1 X DOF STS-2 filter. Left two panels show the transfer functions of driving HEPI X to GS-13 geophone (Equation 3.22), HEPI RY to GS-13, ground to GS-13 (Equation 3.17), and corrected HEPI X to GS-13 (Equation 3.16). Right two panels, the ratio between the ground to GS-13 geophone and corrected HEPI X to GS-13 geophone transfer functions is the STS-2 filter sought after (Equation 3.18). Also shown in red is the fit to the data.

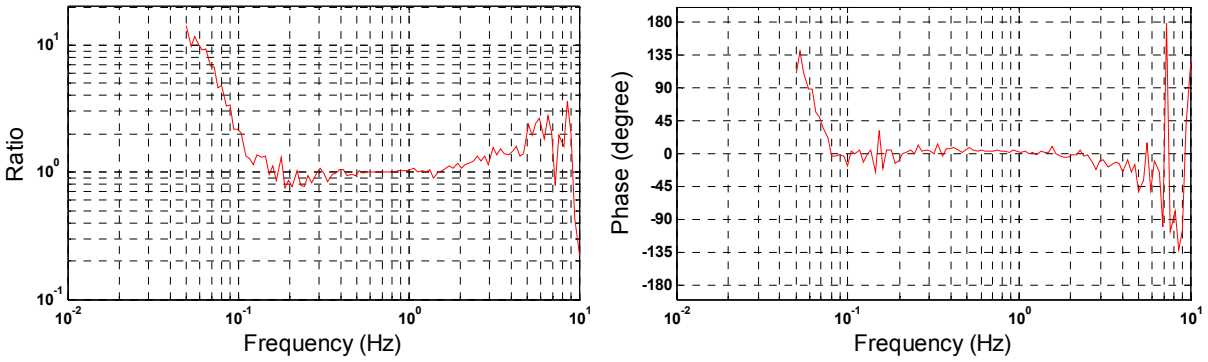

Figure 3.30. Ratio between the fit and the measured STS-2 filter after tilt correction is made for HAM1 X DOF. This can be used to predict the isolation performance, according to Equations 3.9 through 3.11, but with G_g=0.

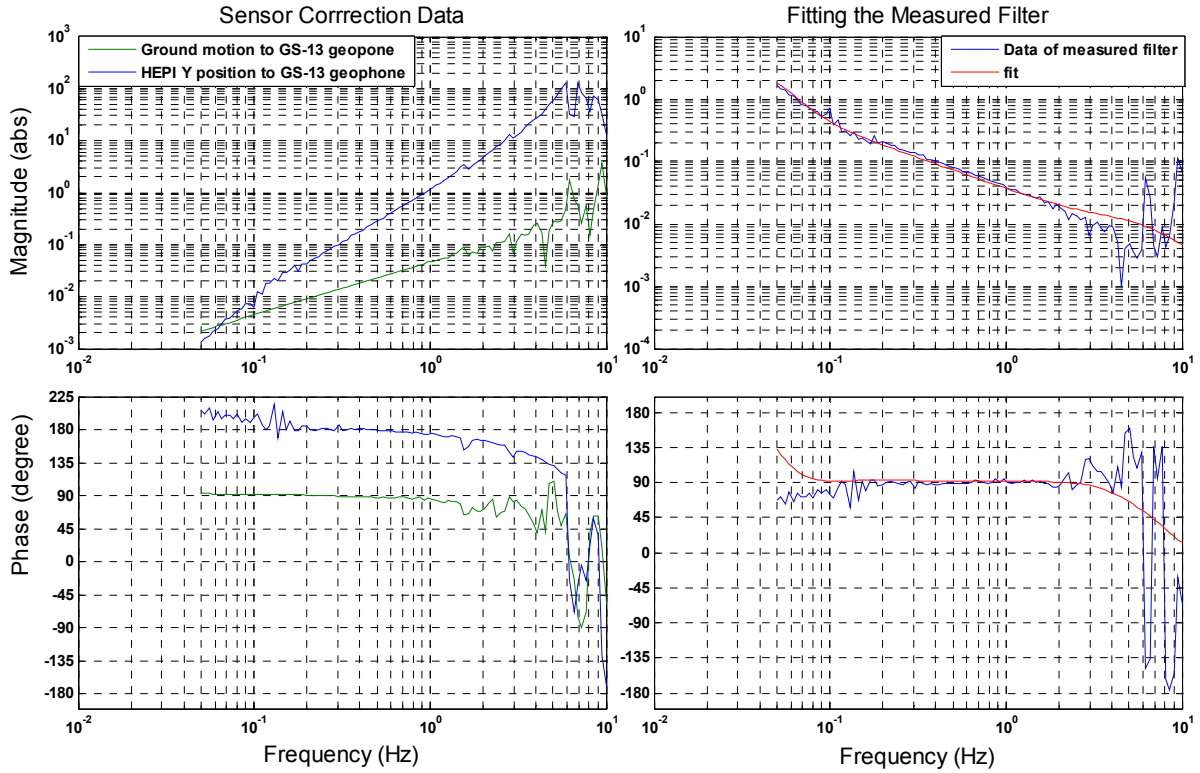

Figure 3.31a. Measuring the HAM1 Y DOF STS-2 filter. Data indicates no tilt behavior in this DOF as seen in the X DOF.

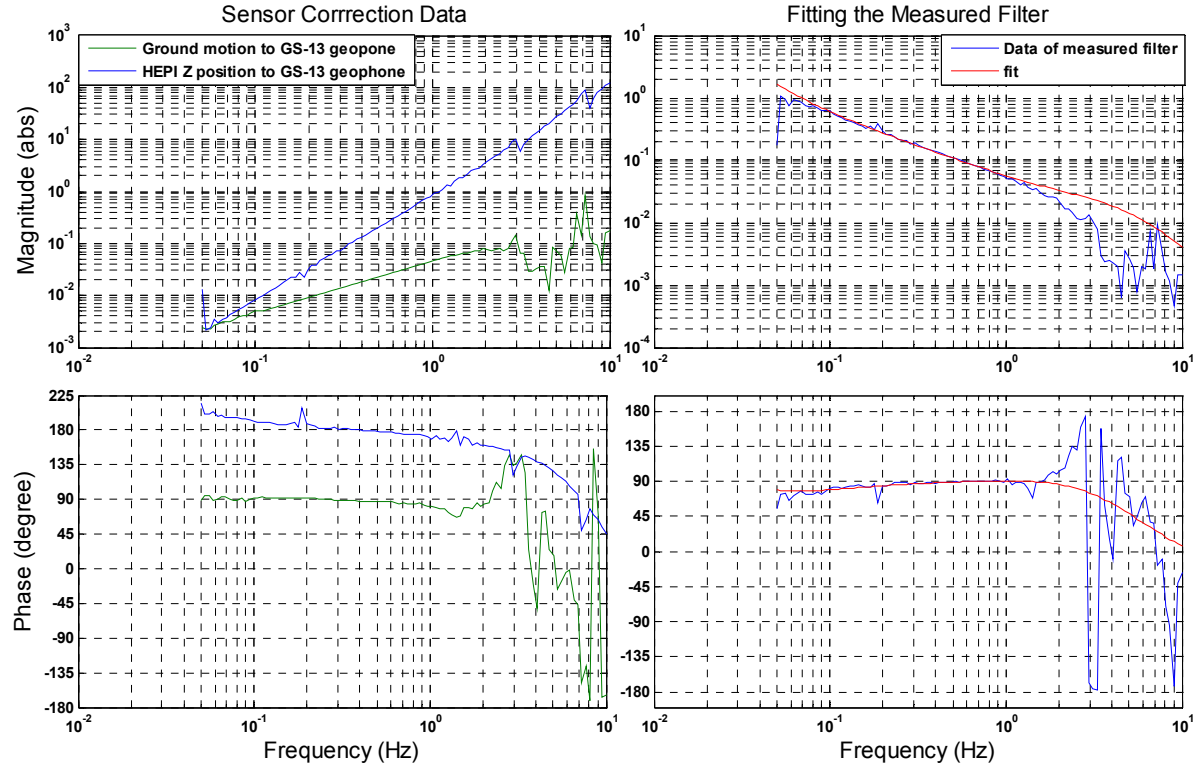

Figure 3.31b. Measuring the HAM1 Z DOF STS-2 filter. Data indicates no tilt behavior in this DOF as seen in the X DOF.

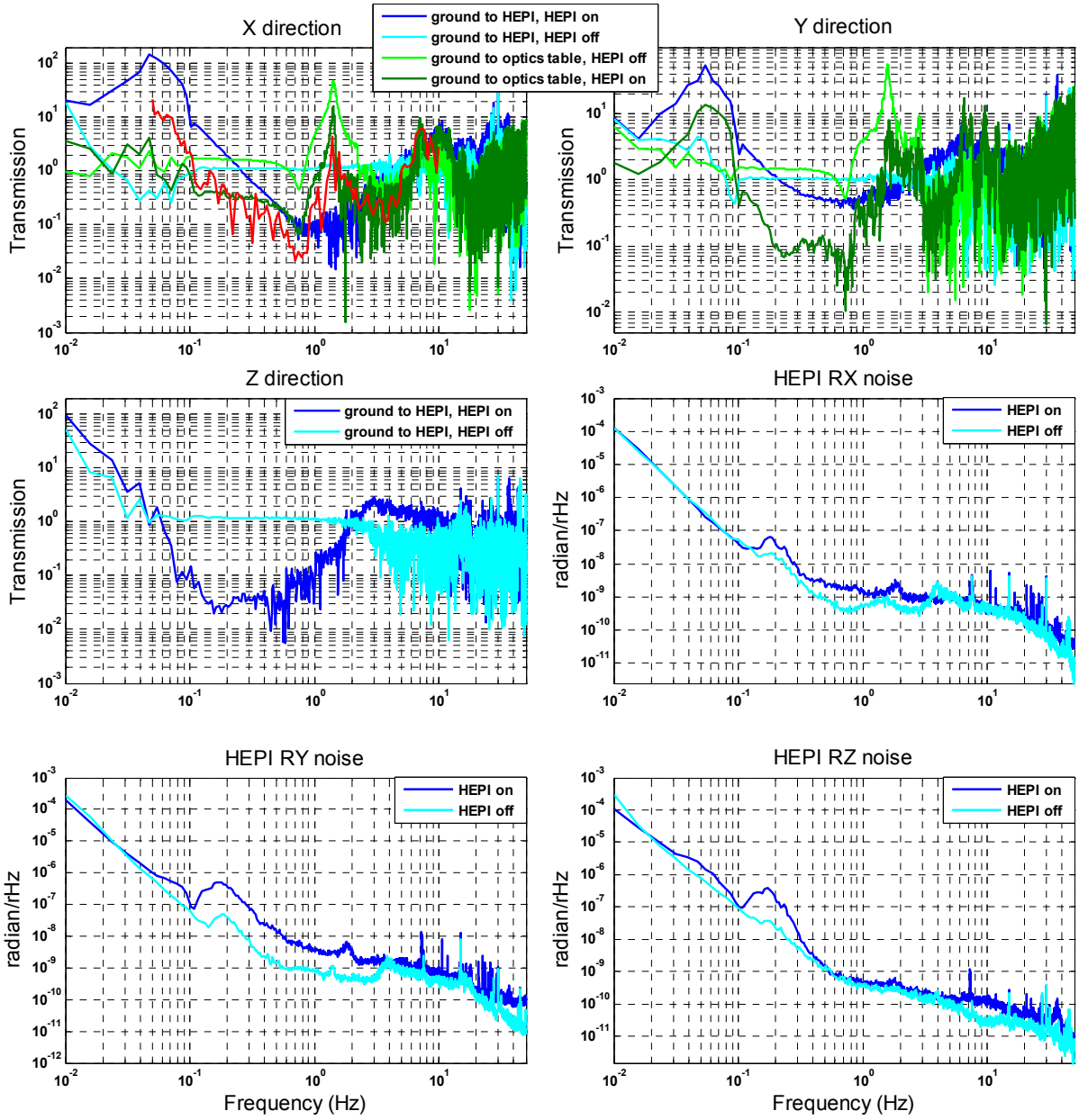

Figure 3.32. Isolation performance of HAM1 during the S5 run. The red trace in the X direction window is plotted according to Equation 3.11, but with G_g=0. Sine L-4C geophones were not used in the feedback control, the first two stack modes lying between 1-3Hz was not able to be suppressed using the resonant gain technique, and is clearly visible in the ground to optics table transmission in the X and Y directions. Performance curves involving the use of L-4C geophones should no longer be trusted in the X, Y, RY, and RZ DOFs in these plots but used as reference only, since quieting the optics with the tilt correction at the HEPI support table obviously will sacrifice noise performance at this level.

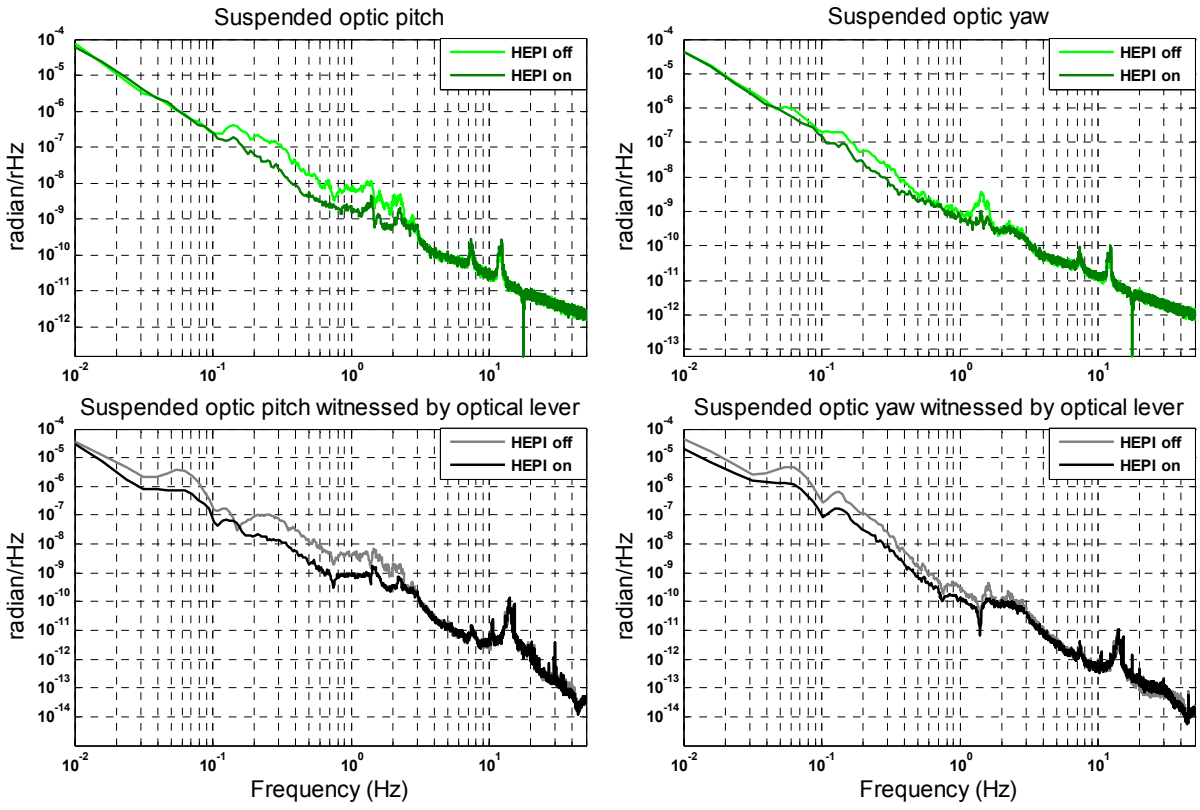

Figure 3.32 continued.

The result we gathered indicates the amount of tilt is ~0.1 radian per meter of x drive below 4Hz (Figure 3.28). Using this number, and assuming the HAMs need to move maximally to ~0.1mm in the X direction [38], without the tilt correction drive, this would cause 10^{-5} radian of tilt or 0.015mm equivalent vertical motion at each end of the support beam.

We did not observe any significant tilt behavior in the feed-forward data in the Y and Z directions, see Figure 3.31. Below 0.1Hz, the feed-forward strategy we employed for the HAMs in X and Y directions is identical to that of BSCs.

3.5 Isolation Performance of Horizontal Access Module

Isolation performance of HAMs is gauged in a fashion similar to what was done in the BSCs. See Figure 3.32. Performance of all HAM tanks is tabulated in Table C.3-C.5 in Appendix C.

CHAPTER 4: COMPARISON OF SEISMIC ISOLATION AT LHO AND LLO IN S5

We compare the performance of seismic isolation at two sites by looking at the percentage of time the LHO 4km and LLO detectors is capable of attaining science mode under different seismic noise conditions. The goal of this study is part of a larger effort to understand quantitatively how isolation obtained from HEPI contributes to the increase in LLO duty cycle, in terms of isolation factor in each band. The comparison requires optimistic assumption that the two interferometers are identical except for their seismic isolation system. For simplicity only 0.1-0.3Hz and 1-3Hz horizontal minute-rms velocity data from the corner station at each site was used in the study, since these are the two primary bands HEPI was designed to target, and also there has been no archived 0.03-0.1Hz corner station ground motion data at LHO to date. The comparison is not a strictly controlled experiment as two variables, the ground condition and the presence or absence of HEPI, are different from site to site. However this is one of the comparisons available that is closest to being objective, as it is currently impossible to do a with/without HEPI comparison at the same site and time.

See Figure 4.1. Upper two panels compare the velocity distribution of two bands during the entire S5 run. Lower two panels show the percentage of time the interferometers were in science mode for a given ground condition. Calculating the percentage values eliminates one variable mentioned above, which is the variation in the ground condition at both sites, and allows a closer comparison. Because the number of samples in a velocity bin decreases as one moves the bin to higher velocity along either axis, the reliability of the percentage value for the velocity bin also decreases. White color represents such ground condition was absent (blue color in upper two panels) during the entire S5 run, hence the percentage calculation is not possible. A number of non-white island bins lie beyond the continuous percentage distribution profiles, representing rare occasions when the interferometers experienced very large ground disturbance.

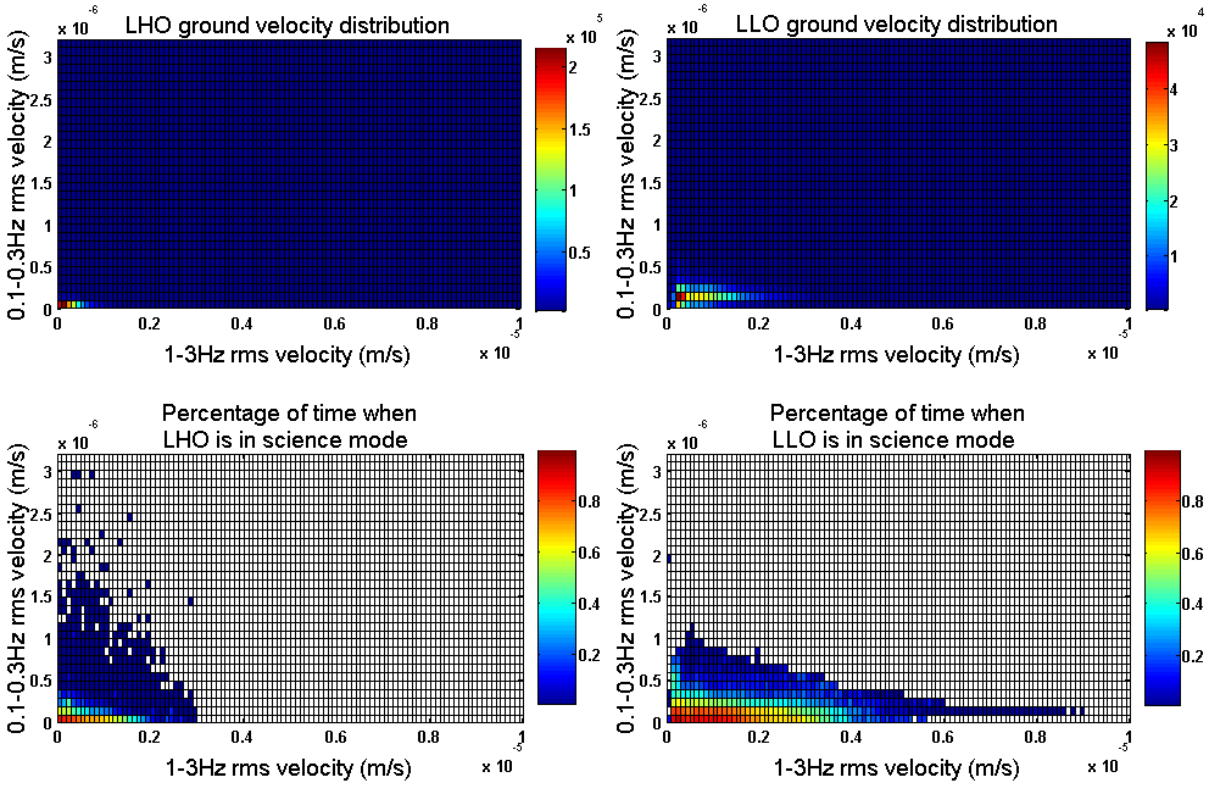

Figure 4.1. Statistical study of LHO and LLO science mode under S5 ground conditions.

Result shown here suggests the velocity at which LLO can maintain at least 50% science mode is roughly twice as much as that of LHO in either band. This conclusion is rather crude and more studies are required.

It is interesting to know what LHO's duty cycle would be with HEPI installed. We first assume for a given velocity bin, the estimated percentage of time when the LHO is in science mode is the greater percentage value observed at the two sites during the S5 run (Figure 4.2). LHO's duty cycle can then be derived by multiplying the estimated LHO percentage (Figure 4.2) with the LHO ground velocity distribution (upper left panel of Figure 4.1), summing over all the resulting bins, and dividing by the total number of minutes (which is the sum of all the bins in the upper left panel of Figure 4.1). This delivers 86.2% duty cycle, or 8.3% increase from LHO S5 run, or about a full month of additional science data per year.

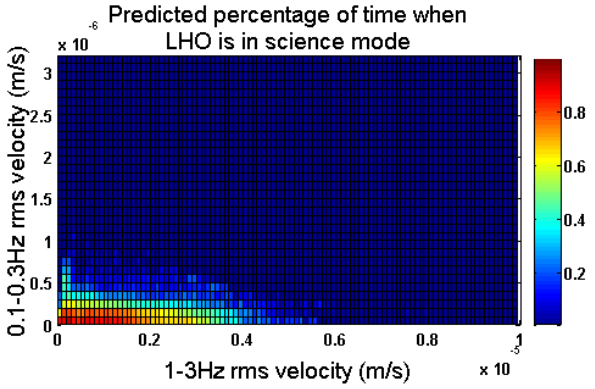

Figure 4.2. Estimated percentage of time when LHO would have been in science mode if it had been fitted with HEPI for S5 run. Zero values were padded in regions where no data is available from both sites.

Similar studies can be done at a more detailed level. One can extend the study to include the 0.03-0.1Hz band. One then has three seismic noise bands as independent variables, and the percentage of time the interferometer is in science mode as dependent variable. An example would be comparing LLO S3 (without HEPI) and S5 (with HEPI). This is possible since LLO has always archived the 0.03-0.1Hz band data since the beginning of S3. Unfortunately this faces one difficulty as S3 only last for two months, and the number of samples in each velocity bin decrease drastically as one adds another velocity axis.

CHAPTER 5: FUTURE POSSIBLE HEPI IMPROVEMENTS AND CONCLUSION

5.1 Incorporating Geophone Signals into the Feedback Loop in BSC RX and RY DOFs

As described in Section 3.2, we only used the position sensors in the feed-back loop in RX and RY DOFs, based on the consensus that the ground motion is much quieter in RX and RY than in the X, Y, and Z DOFs. Later, the data we gathered from the HEPI RX and RY modal geophone sensors somewhat confirmed this. It is estimated the horizontal optics table motion induced by HEPI RX and RY motion is more than a factor of ten below that from HEPI X and Y. See Figure 5.1. This is calculated by considering that the distance between the payload attachment plate on the vertical actuator (F in Figure 3.6a) and the optics table is ~67cm, that the structure in-between is a rigid body, and that HEPI RY motion directly translates to optics table motion in X. The tilt-horizontal stack transfer function was not considered, but even it is the effect is not expected to exceed a factor of ten.

We tested incorporating geophone signal into the RX and RY DOFs feedback control on ETMX tank, using the standard control scheme used in X, Y, and Z DOFs, i.e. setting the frequency where the position and geophone sensor loop transfer functions have equal magnitude to be 0.5Hz. Such plan was motivated by the fact that in most BSC and HAM chambers, HEPI offers little to no isolation in these DOFs, and in some cases the noise is enhanced when it is engaged (Table C.3).

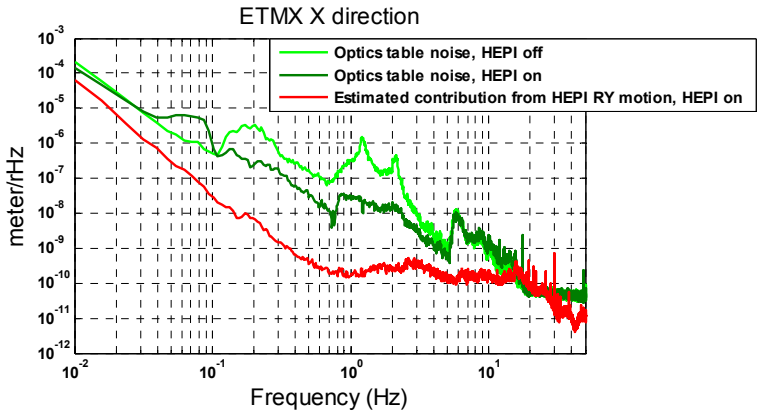

Figure 5.1 Estimate of contribution to X motion at the optics table from HEPI RY motion.

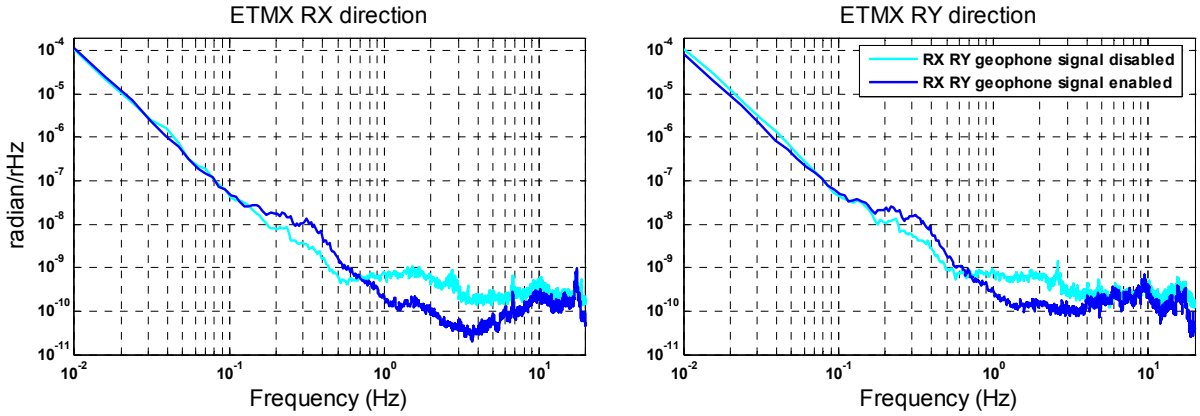

Figure 5.2. Isolation performance of ETMX RX and RY DOFs, with the geophone signals incorporated into the feed-back loop.

In our test the noise is greatly reduced above 1Hz, but the noise is enhanced below 1Hz (Figure 5.2). This is not too surprising as these DOFs lack feed-forward, and the performance is described by Equation 3.2. To improve, it is worth trying using the geophones only. However, this posses some challenges as the geophone noise below ~0.5Hz needs to be rejected fast enough, while the loop gain is maintained at a decent ~1/f $^{1.5}$ relationship between 1~10Hz. Another alternative requires measuring the angular DOF motion of the ground, possibly by a tilt meter, or two ground seismometers (G in Figure 3.2), and feed-forward their signal into the system.

Revisiting BSC RZ DOF

From what we learned from the RX and RY DOFs, incorporating the geophones to the feedback adds noise to the system below 1Hz. It is likely the RZ DOF would exhibit the same behavior if it were a stand-alone loop, i.e. without the X and Y loops engaged. The fact we are getting a reduced RZ motion in some tanks below 1Hz may very well originated from quieter X and Y motion and through the X→RZ and Y→RZ coupling, but not from better RZ loop design. Further testing is required to test this hypothesis. Also it is worth point out when comparing the RZ motion at the HEPI level and suspended optic (Figure 3.22), the HEPI noise is one to two

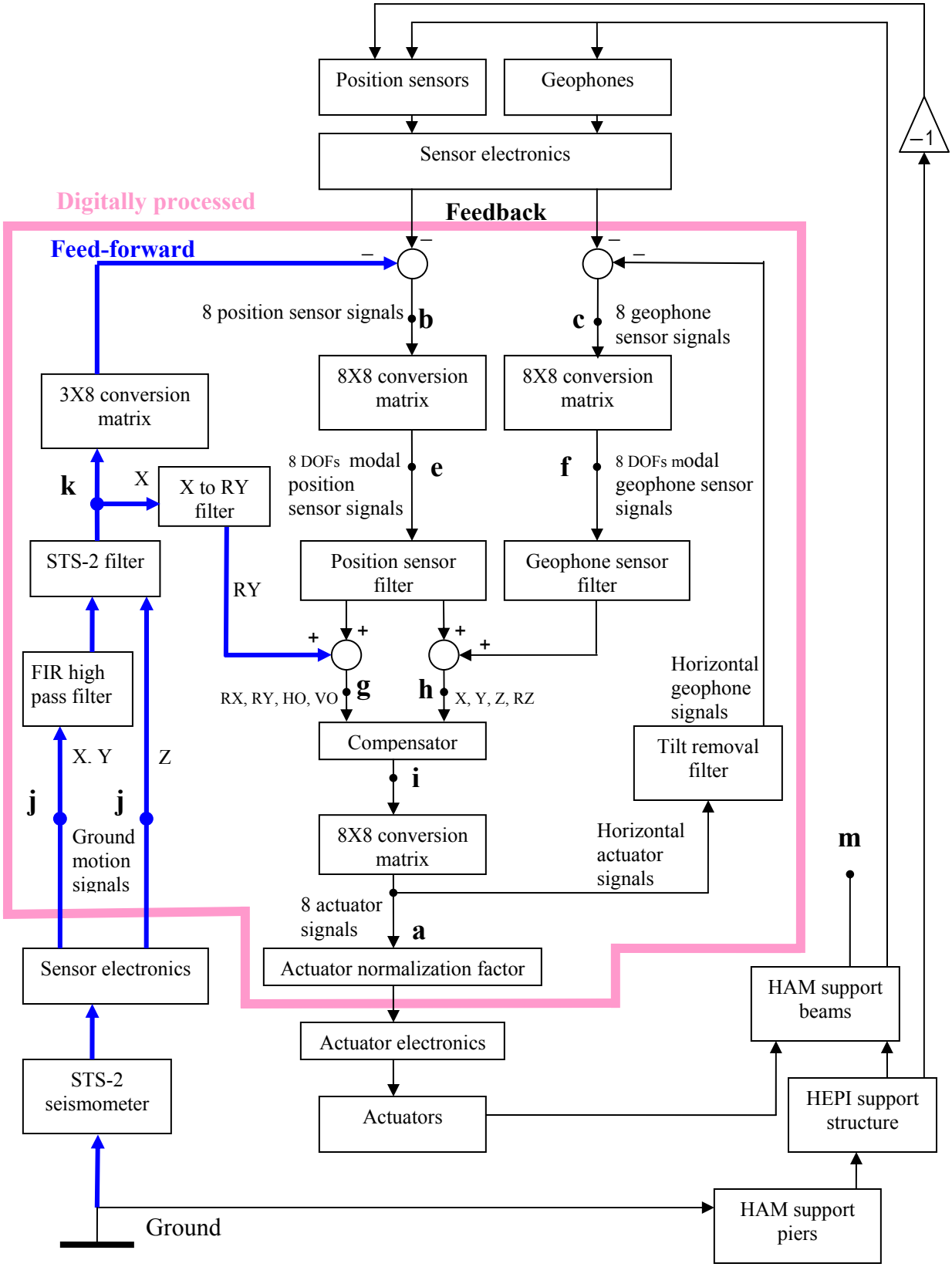

Figure 5.4. Schematic diagram of HAM HEPI system with tilt removal path for the horizontal actuator to horizontal geophone sensor transfer functions.

orders of magnitude below the suspended optic noise from 0.1 to 10Hz. It is likely the RZ motion seen in the suspended mass mostly comes from X→RZ and Y→RZ coupling, but not from the RZ motion at the HEPI level.

5.2 Incorporating Geophone Signals into the HAM Feed-Back Loop

As discussed in Chapter 3, incorporating the geophones into HAM HEPI feedback control adds noise to the system. It is necessary to first remove the tilt component in the actuator to geophone transfer functions before they are used in the feed back loop, see Figure 5.4. We calculated the amount of tilt signal needed to be removed, and generated a filter to remove the tilt signal based on a Matlab function fminsearch (see Appendix B). After the tilt signal is removed, the geophones are used in the same manner as in the BSCs (Figure 3.8). Isolation performance in

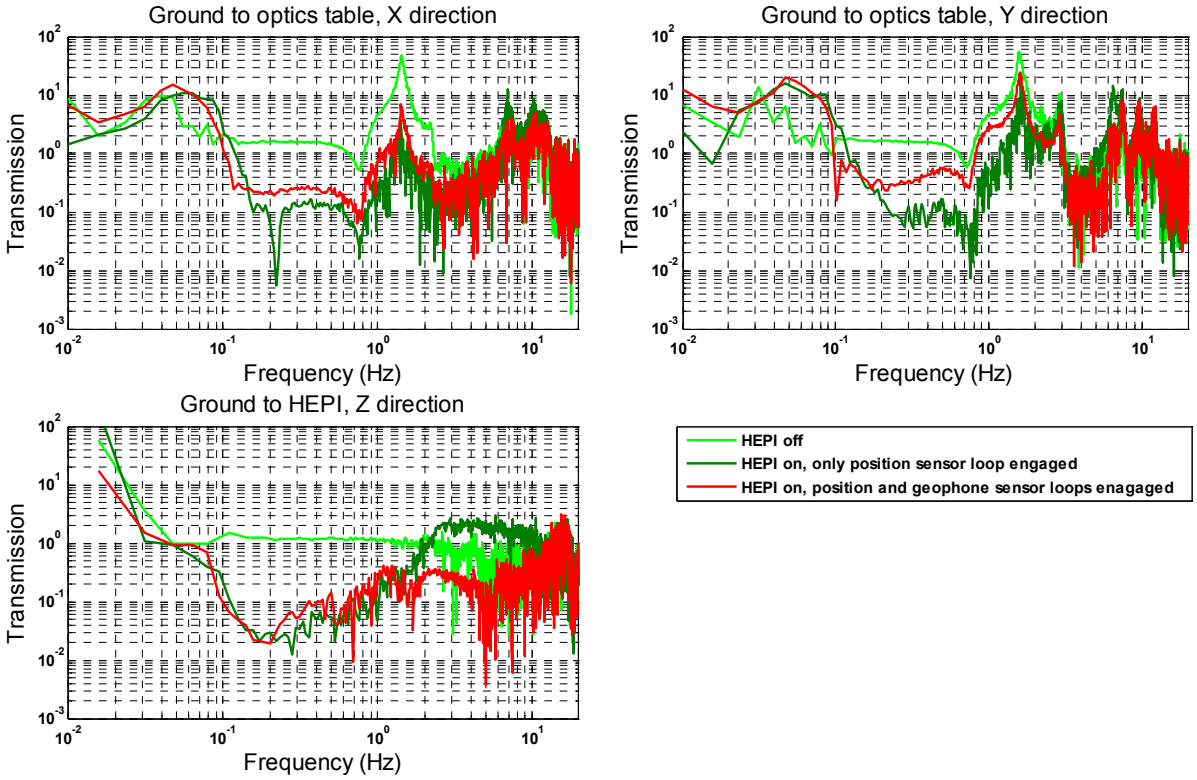

Figure 5.5. Comparison of isolation performance of HAM1 from different control scheme. Engaging the geophone loops does not improve the isolation performance in the X and Y directions. The Z direction, however, improves greatly in the 1-10Hz region. Data shown here is from separate measurement, different from shown in Figure 3.32.

the X and Y directions obtained from this scheme is still inferior to the scheme in which only the position sensors are used, see Figure 5.5.

We do not have a full model to explain the excess noise yet, and more detail study is required. Comparing to the BSC suggests that the noise may originate from the geometry and softness of the HAM support beam, i.e., the horizontal actuator line of force is above the in-vacuum support beam, the cross-section of the HAM cross beam is only fraction of that of the BSC, and the distance between the two support beams in the X direction is only about half of their length (Figure 3.5), making the support structure intrinsically easier to tilt in the RY direction. It is believed re-designing the support beam by reducing the horizontal-tilt cross coupling and its overall structural stiffness will improve the performance-a plan that is now being carried out [39], but out of the scope of this thesis and will not be discussed any further.

5.3 Very Long Term HO and VO DOFs

It was discovered the over-constrained modes of BSC exhibited oscillatory behavior on June .14, 2005 (Figure 5.6). Fearing their motion will propagate into main detector control signal, over-constrained loops were disabled on Dec. 24, 2005. The oscillation is most likely due to insufficient phase margin at the lower unity gain frequency. For a loop with ~$1/f^{1.5}$ below unity gain frequency at ~10Hz, and ~f below 0.01Hz, the lower unity gain frequency can be

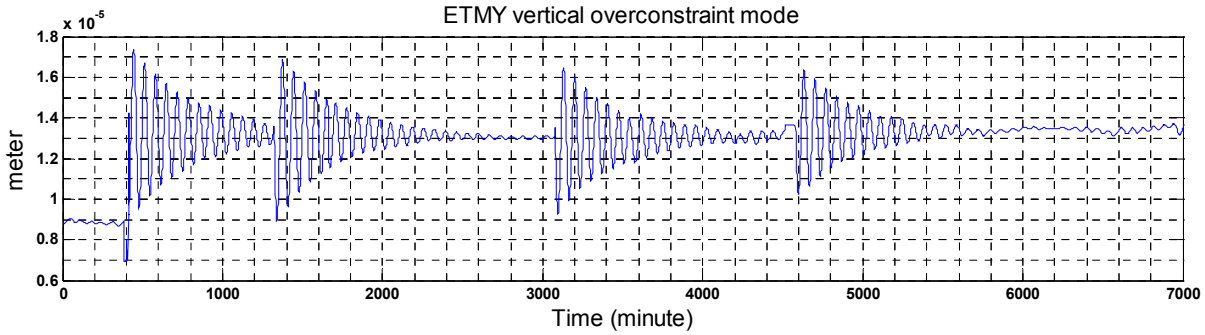

Figure 5.6. Very long period oscillation seen in ETMY vertical over-constrained mode, with period of ~70 minutes, decay time of ~1500 minutes, and ~0.01mm maximum equivalent vertical motion at the ends of the support beams.

projected to ~10^{-5}Hz and accounted for the observed period. The low frequency high pass can be improved, however without any system identification data below 0.01Hz it is not trivial to accurately predict the phase margin at lower loop unity gain frequency.

In order to lock these two modes down to DC, the HEPI-support beam interface will need to be improved, so each time a HEPI unit is installed there is no over-constraining or stress built-up at the interface. Once the installation is complete, one finds the stress-free reference position of these modes by taking the long term average of the position sensor readings when HEPI is not yet engaged, and lock to that position once HEPI in engaged.

5.4 High Stiffness and High Loop Gain System

As discussed in Section 3.2, higher geophone loop gain suppresses the payload motion better until the noise level of the geophones and their electronics is reached. Doing this requires several tasks. The various (anti-)resonances at ~20-60Hz need to be either damped or moved to higher frequency (more rigid system), as from our experience it is often difficult to compensate them properly in the software if their quality is too high. To name a few: Support beam flexing mode (10-20Hz) can be improved by adding enforcements, possibly by bridging the two beams or adding structural triangles. Support pier vibration mode (20-30Hz) can be addressed by adding structural short to the ground. The actuator tripod compression mode (50-60Hz) can be improved by stiffer tripod legs, or replacing the tripod by a better interface. The first two would probably benefit from some form of damping mechanism as well.

The system identification data in the ~10-100Hz region needs to be better resolved (although in some cases the data is well resolved up to 100Hz). To achieve this involves (but not limited to) making finer frequency scan, more averages, and maintaining data coherence during the data collecting process. The compensator design can then be more accurate and more phase margin is available when setting the control loop gain at higher frequency. As a bonus the resonant gain filter technique can be implemented for higher resonant modes.

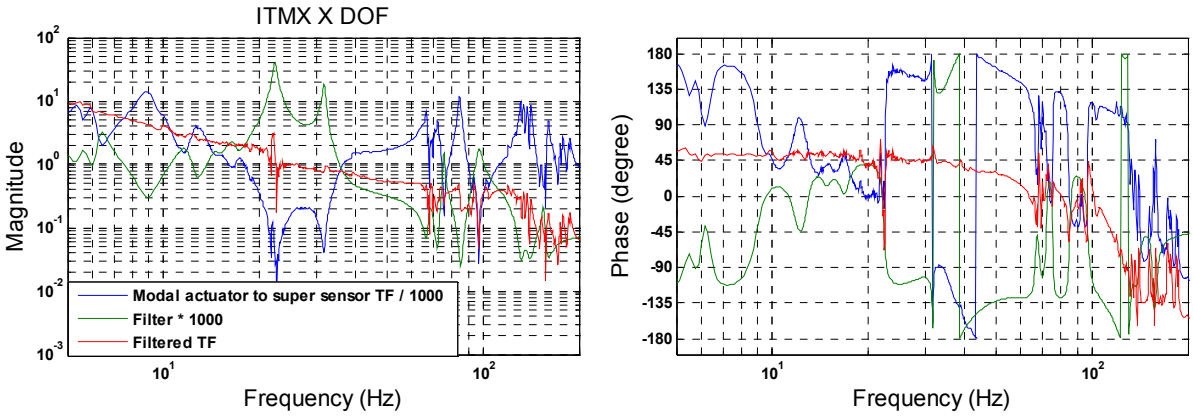

Figure 5.7. Attempting to set the unity gain to 25Hz in the ITMX X DOF immediately faces the (supposedly) support pier anti-resonance at 22Hz that is dominated by noise and hard to compensate. Once that is fixed, resonant features as high as 30Hz can be properly compensated, and the overall loop gain increases by a factor of ~4. The Modal actuator to super sensor transfer function and its filter are scaled to fit in this plot.

5.5 Feed-Forward Below 0.1Hz

To start this discussion requires a more accurate definition of the term 'slab' as the 'ground' mentioned in previous sections. The slab is the concrete foundation on which the entire interferometer is built, and the ground is actually the soil beneath it.

As discussed in Section 3.2.1 and 3.3, the FIR high pass filter in the feed-forward path rejects the slab tilt noise below 0.04Hz at a cost of a bump between 0.04 and 0.1Hz region, and as a result the suspended optic noise at 0.04-0.1Hz is enhanced in many DOFs. It is very desirable to relocate this bump to lower frequency.

To achieve this, a better understanding of ground to slab coupling and removing the tilt component from the sensed horizontal motion are required. If the tilt is coupled to horizontal slab motion in a dependent way depicted in Figure 3.27 (where the blue support table is now replaced by the slab), Equation 3.21 provides the method for removing the tilt. A tilt-free horizontal signal is a factor of $s^2/(s^2 \pm \tau)$ of the sensed horizontal motion. The ± sign in the denominator depends on the sign of tilt radius R, i.e., tilting up or down for a given horizontal motion. In the + case, the problem essentially becomes finding the tilt radius or the relative strength of the tilt τ. In the

– case, the factor is unstable, and a separate instrument (perhaps a tilt meter) is required to resolve the tilt. If the slab tilt and horizontal slab motion are independent, then the above discussion does not apply and a separate instrument is always needed. More challenges lay ahead if different parts of the slab tilts differently (as might be the case in the corner station). Given the slab thickness of ~76cm and length of ~90m, it is questionable if the slab behaves as a rigid body.

Suppose a successful tilt removal allows one to relocate the bump of the FIR high pass filter down half a decade to roughly 0.0083Hz (the STS-2 low frequency pole frequency) to 0.03Hz, then below 0.0083Hz the STS-2 response and the FIR filter alone already provide f^3 attenuation to the horizontal slab motion, and f attenuation to any residual tilt motion. As a result the f high pass component in the STS-2 filter will no longer be necessary, which makes fitting the measured STS-2 filter data easier.

5.6 Conclusion

HEPI is an active isolation system, whose main components consist of off-load springs, position and geophone sensors, ground seismometers, and hydraulic actuators. The geophone sensor feedback loops alone provide noise suppression, while the position sensor feedback loops work with the feed-forward signals sensed by the ground seismometers to provide isolation. All feedback control loops and feed-forward paths follow simple single-input-single-output scenario, except the beam-line direction feed-forward path for the HAMs. Both types of feedback loops were implemented in the BSCs. Resonant gain filters implemented in the geophone feedback control loops allow addition suppression of the lowest frequency mechanical resonant modes within the seismic isolation system. Only the position sensor loops were implemented in the HAMs, due to the softness of the HAM support beam and the strong horizontal-to-tilt coupling property of the entire eternal pre-isolator structure. The horizontal-to-tilt problem in the HAMs was addressed by adding an extra tilt correction path, parallel to the beam-line direction

horizontal feed-forward path to compensate. The current HEPI is roughly optimized in the 0.1-3Hz region, this is done with the expense of ground noise enhancement below 0.1Hz. Above 3Hz isolation performance starts to degrade due to insufficient loop gain and good quality feed-forward signal. Overall HEP provides a factor of few to few ten suppression in the 0.1-3Hz band. The performance level among different tank and DOF is not uniform, and is worth further investigation.

We have examined the recent seismic noise records at LLO and LHO from Oct. 1, 2003 to Oct. 1, 2006, using two types of seismometers. The registered seismic noise at both sites had decreased but the amount was insignificant, and could likely be short-term fluctuation. Base on the data we have so far, it is clear that the LLO seismic environment has been consistently noisier than that of LHO, from 0.1 to 3Hz, by a factor of 2.4 to 9.0, and is expected to continue behaving in similar manner in the future. Long term trend can not be deduced without further study. Careful recalibration of the instruments as well as their supporting signal readout electronics is inevitably necessary for accurate long-term measurement. HEPI has been and still will be valued for the isolation it provides. Should the future seismic level remain the same, HEPI should be able to support LLO in delivering at least a duty cycle at the S5 standard.

We also performed a top level comparison of the isolation performance of the two LIGO sites during S5. We derived that the ground velocity at which LLO can maintain at least 50% science mode is roughly twice as much as that of LHO in the 0.1-0.3Hz and 1-3Hz bands. From the result we further estimated that with HEPI installed, LHO's duty cycle would be 86.2%.

Finally, a number of improvements can be made to HEPI. These includes, but not limited to: incorporating the geophone feedback loops to the rotational DOFs of HEPI, incorporating the geophone feedback loops in HAM to suppress higher frequency noise, structural reinforcement and better system identification data for high gain system design, and resolving the sub-0.1Hz

ground tilt noise and removing it from the horizontal feed-forward signal in order to do sub-0.1Hz seismic isolation.

REFERENCES

[1] P. Linsay, A Study of a Long Baseline Gravitational Wave Antenna System (Original LIGO Proposal), 1983.

[2] E. Ponslet, Transfer Function and Drift Measurements on the BSC First Article Stack, LIGO Project Internal Document, T980129-00-D.

[3] J. A. Giaime, Studies of Laser Interferometer Design and a Vibration Isolation System for Interferometric Gravitational Wave Detectors, PhD Thesis, 1995.

[4] J. Giaime, P. Saha, D. Shoemaker, and L. Sievers, A Passive Vibration Isolation Stack for LIGO: Design, Modeling and Testing, Rev. Sci. Instrum: 67, 1996.

[5] E. J. Daw et al, Long-term Study of the Seismic Environment at LIGO, Class. Quantum Grav.: 21 No 9, 2255-2273, 2004.

[6] C. Hardham, Quiet Hydraulic Actuators for LIGO, PhD Thesis, 2005.

[7] B.Lantz, LIGO Project LASTI Elog, http://emvogil-3.mit.edu/ilog/pub/ilog.cgi?group=lasti&task=view&date_to_view=04/04/2003&anchor_to_scroll_to=2003:04:04:13:45:53-blantz

[8] Abbott B et al, Phys. Rev. D 76 042001, 2007

[9] Abbott B et al, Phys. Rev. D 77 022001, 2008

[10] Abbott B et al, LIGO Project Internal Document, P080095-04-Z, 2009

[11] Abbott B et al, Phys. Rev. D 77 062002, 2008

[12] Abbott B et al, LIGO Project Internal Document, P080024-03-Z, 2008

[13] Abbott B et al, Class. Quantum Grav. 24 5343–5369, 2007

[14] Abbott B et al, ApJ 659 918, 2007

[15] Abbott B et al, Phys. Rev. D 76 082003, 2007

[16] G. Streckeisen AG., Portable Very-broad-band Tri-axial Seismometer.

[17] Güralp Systems Ltd, CMG-40T Triaxial Broadband Seismometer.

[18] J. Zweizig, Data Monitoring with the LIGO DMT, LSC Meeting at Hanford, August 15-17, 2000.

[19] K. Riles, Status of DMT Software Tasks, LSC Meeting at Hanford, August 15-17, 2000.

[20] S. Wen, Report on LLO and LHO Seismic Environment for the Past Three Years, LIGO Project Internal Document T070036-00-H.

[21] Kaman Instrumentation Operations, DIT-5200 Non-Contact Displacement Measuring System.

[22] Sercel Incorporated, Mark Products L-4 Seismometer.

[23] Geotech Instruments LLC, Portable Short-period Seismometer Model GS-13.

[24] R. Abbott et al, Seismic Isolation Enhancements for Initial and Advanced LIGO, Class. Quantum Grav: 21 No 5, 2004.

[25] Discussion with D. Coyne.

[26] R. Mittleman, J. Phinney, K. Masons, LIGO Project LASTI Elog, http://emvogil-3.mit.edu/ilog/pub/ilog.cgi?group=lasti&task=view&date_to_view=02/15/2002&anchor_to_scroll_to=2002:02:21:11:37:13-richard

[27] R. Mittleman, LIGO Project LASTI Elog, http://emvogil-3.mit.edu/ilog/pub/ilog.cgi?group=asti&task=view&date_to_view=04/29/2005&anchor_to_scroll_to=2005:04:29:13:28:53-richard

[28] D. Coyne, LIGO Project LASTI Elog, http://ilog.ligo-la.caltech.edu/ilog/pub/ilog.cgi?group=detector &date_to_view=04/30/2004&anchor_to_scroll_to=2004:04:30:04:03:19-coyne

[29] R. Mittleman, LIGO Project LASTI Elog, http://emvogil-3.mit.edu/ilog/pub/ilog.cgi?group=lasti&task=view&date_to_view=03/27/2003&anchor_to_scroll_to=2003:03:27:17:44:44-richard

[30] R. Mittleman, LIGO Project LASTI Elog, http://emvogil-3.mit.edu/ilog/pub/ilog.cgi?group=lasti&task=view&date_to_view=01/14/2005&anchor_to_scroll_to=2005:01:14:17:42:19-richard

[31] W. Hua, Low Frequency Vibration Isolation and Alignment System for Advanced LIGO, PhD Thesis, 2005.

[32] S. Waldman, LIGO Project LLO Elog, http://ilog.ligo-la.caltech.edu/ilog/pub/ilog.cgi?group=detector&date_to_view=11/30/2006&anchor_to_scroll_to=2006:12:01:00:03:16-waldman

[33] M. Landry and D. Ottaway, Summary of Mechanical Resonances in the LIGO Hanford Interferometers, LIGO Project Internal Document, T000020-00-W.

[34] R. Mittleman, LIGO Project LASTI Elog, http://emvogil-3.mit.edu/ilog/pub/ilog.cgi?group=lasti&task=view&date_to_view=01/21/2005&anchor_to_scroll_to=2005:01:21:13:58:13-richard

[35] L. Ruet, LIGO Project LASTI Elog, http://emvogil-3.mit.edu/ilog/pub/ilog.cgi?group=lasti&task=view&date_to_view=05/17/2004&anchor_to_scroll_to=2004:05:14:21:58:28-lruet

[36] R. Mittleman, LIGO Project LASTI Elog, http://emvogil-3.mit.edu/ilog/pub/ilog.cgi?group=lasti&task=view&date_to_view=01/11/2005&anchor_to_scroll_to=2005:01:11:16:36:42-richard

[37] L. Ruet, LIGO Project LASTI Elog, http://emvogil-3.mit.edu/ilog/pub/ilog.cgi?group=lasti&date_to_view=08/26/2005&anchor_to_scroll_to=2005:08:26:13:14:32-lruet

[38] S. Wen, LIGO Project SEI Elog, http://ligo.phys.lsu.edu:8080/SEI/662

[39] A. Stein, LIGO Project SEI Elog, http://ligo.phys.lsu.edu:8080/SEI/1281

[40] R. Schofield, LIGO Project Webpage, http://jupiter.ligo-wa.caltech.edu/~roberts/SciMon Camp PEM.html

[41] J. Giaime, LIGO Project LLO Elog, Dec. 24, 2004, 03:30:46, http://ilog.ligo-la.caltech.edu/ilog/pub/ilog.cgi?group=detector&date_to_view=12/23/2004&anchor_to_scroll_to=2004:12:23:21:30:46-giaime

[42] J. A. Nelder and R. Mead, A Simplex Method for Function Minimization, Computer Journal 7: 308–313, 1965.

APPENDIX A: DATA ISSUES AND METHODS USED IN THE SEISMIC NOISE STUDY

A.1 Data Quality

There was no raw LLO STS-2 data From March 2004 to July 2004, during which HEPI was installed. Constructing velocity percentile curves from the time period, Oct. 1, 2003 to Oct. 1, 2004, will have no sample from these months. This is the reason that only two years of LLO STS-2 data was used in this study. Table A.1 lists the number of available minute-rms data points per year.

Physical locations of the data are LDAS tape archives at both sites. Specifically, under directories,

LLO STS-2: /archive/frames/dmt/LLO/LLO_SEI_blrms, subdirectories /L-M-780 to /L-M-843.

LLO Guralp: /archive/frames/dmt/LLO/New_Seis_Blrms, subdirectories /L-M-749 to /L-M-843.

LHO Guralp: /dmt/New_Seis_Blrms, subdirectories /H-M-749 to /H-M-843.

The exact DMT seismic channel names stored in the tape archives have changed few times during the time period inspected, even though the physical quantity they represent remained the same. Table A.2, A.3, and A.4 summarize the channel name changes from Oct. 1, 2003 to Oct. 1, 2006 (GPS time 749001613 to 843696014). LLO Guralp channels are the only ones that have remained unchanged during this period.

In this study, data quality suffers from two major problems. The first is intentional and un-natural disturbances near the seismometers, such as commissioning activities and heavy construction machinery moving onsite the observatories. At the time of this study, detail record of times when these events occurred was already impossible to reconstruct. This study does not exclude any data that might pertain to those times. The second is data drop-outs (or zero data points) or unrealistic high values (>=2^{30} counts, or saturated ADC counts squared) in the minute-

Table A.1. Number of available raw data points per year. A full-year of data would have 525600 points. Numbers in the parenthesis indicate the percentage of data available per year.

	LLO STS-2	LLO Guralp	LHO Guralp
Oct 1 2003 to Oct 1 2004	-	480480 (91.4%)	477660 (90.9%)
Oct 1 2004 to Oct 1 2005	420960 (80.1%)	403500 (76.8%)	515940 (98.2%)
Oct 1 2005 to Oct 1 2006	518340 (98.7%)	507480 (96.6%)	522660 (99.4%)

Table A.2. Naming convention of LLO STS-2 channels. {station}=LVEA, or ETMX, or ETMY. {direction}=X or Y. {band}=0p03-0p1, or 0p1-0p2, or 0p2-0p35, or 0p35-1, or 1-3.

GPS time	LLO STS-2
780624013 to 813376800	L1:SEI-{station}_STS-2_{direction}_{band}Hz.rms
813376800 to 843696014	L1:DMT-BRMS_SEI_{station}_STS-2_{direction}_{band}Hz.rms

Table A.3. Naming convention of LLO Guralp channels. {station}=LVEA, or EX, or EY. {direction}=X or Y or Z. {band}= 0.1-0.3, or 0.3-1, or 1-3, or 3-10, or 10-30.

GPS time	LLO Guralp
749001613 to 843696014	L0:PEM-{station}_SEIS{direction}_{band}Hz.rms

Table A.4. Naming convention of LHO Guralp channels. {station}=LVEA, or EX, or EY, or MX, or MY. {direction}=X or Y or Z. {band1}= 0.1-0.3, or 0.3-1, or 1-3, or 3-10, or 10-30. {band2}= 0.1_0.3, or 0.3_1, or 1_3, or 3_10, or 10_30.

GPS time	LHO Guralp
749001613 to 812836800	H0:PEM-{station}_SEIS{direction}_{band1}Hz.rms
812836800 to 812840400	H0:DMT-BRMS_PEM-{station}_SEIS{direction}_{band2}Hz.rms
812840400 to 843696014	H0:DMT-BRMS_PEM_{station}_SEIS{direction}_{band2}Hz.rms

Table A.5. The percentage of bad data.

	LLO STS-2	LLO Guralp	LHO Guralp
Oct 1 2003 to Oct 1 2004	-	16.5%	1.3%
Oct 1 2004 to Oct 1 2005	0.6%	3.6%	0.5%
Oct 1 2005 to Oct 1 2006	0.3%	0.3%	0.6%

rms data generated by LIGO DMT error. The percentage of raw data contaminated by data drop-outs or unrealistic high values is listed in Table A.5. Times when these occurred are excluded from this study.

Table A.6. Calibration factor. velocity bin size and number of bins used in this study.

	LLO STS-2	LLO Guralp	LHO Guralp
Calibration factor (m/s)	4.36E-04	7.63E-03	7.60E-03
Histogram bin size (m/s)	1.00E-03	1.00E-02	1.00E-02
Number of bins	14280	25002	25002

Another potential data quality issues is the slow drift in the calibration of the seismometers. We did not know weather such drift was present and we assumed the calibration remained constant in the study.

A.2 Method

The DMT seismic data stores the ADC output counts squared. The first step of the analysis is to take the square root of the raw data and apply the calibration factor shown in Table A.6. Documentation of the calibration factor can be found in [40, 41].

For each channel, cumulative normalized histograms were constructed with bin size and number of bins (which cover 0 to 32768 ADC counts) shown in Table A.6. Cumulative normalized histograms multiplied by 100 are then the velocity percentile curves. 50th, 75th, 90th, 95th rms-velocity percentiles were then derived from the x value (or velocity) of where the y=50, y=75, y=90, y=95 lines intersects the curves in the velocity percentile curves.

APPENDIX B: MATLAB SCRIPT USED TO REMOVE THE TILT COMPONENT OF ACTUATOR TO HORIZONTAL GEOPHONE SENSOR TRANSFER FUNCTION SIGNAL

The script utilizes the matlab function fminsearch which is based on Nelder-Mead Simplex search method [42]. In this case the search is merely one-dimensional. First, the script searches for a best model transfer function to fit the data. Then, it searches for the best amount of tilt that should be removed so the tilt-deducted data matches the model most closely.

```
%This loads a set of frequency response data for HAM1.
MC1_D_Actuator_Transferfunctions_frd.mat
[HAM1_ACT_GH_TFall,freq]=frdata(MC1_FRDATA(9:12,1:4));

%Cycles through every pair of actuator-sensor transfer function data.
for n=1:4%actuator   H1-H4
for    m=1:4;     %sensor, H1-H4
     HAM1_AH_GH_TF=squeeze(HAM1_ACT_GH_TFall(m,n,:));
    if m==n %co-located actuator-sensor pair

%These are the initial guess for the gain of the tilt removal filter and the
%actuator to geophone transfer function model.
        par1=.1;par2=3500; %par1=filter gain, par2=model gain
    else
        par1=30;par2=-500;
    end

%This step search for best fit to the actuator to geophone transfer function
data by adjusting the model gain.
[par_2]=fminsearch(@Fit_AH_GH_TF_Model,par2,options,HAM1_AH_GH_TF,freq);

%This step gives the error of the fit.
[HAM1_AH_GH_TF_FitError,HAM1_AH_GH_TF_Model_freqresp]=Fit_AH_GH_TF_Model(par_
2,HAM1_AH_GH_TF,freq);

%This step search for best tilt removal filter by adjusting its gain.
[par_1]=fminsearch(@design_correction_filter_AH_GH_v2,par1,options,HAM1_AH_GH
_TF,par_2,HAM1_AH_GH_TF_Model_freqresp,freq);

%This step gives the error between the model and the real signal after tilt
is removed.
[HAM1_AH_GH_AveError,HAM1_AH_GH_correction_filter_freqresp,HAM1_AH_GH_TF_corr
ect_freqresp]=...

design_correction_filter_AH_GH_v2(par_1,HAM1_AH_GH_TF,par_2,HAM1_AH_GH_TF_Mod
el_freqresp,freq);

%Construct a matrix which is the magnitude of tilt for each actuator-sensor
pair.
if (n==1)&(m==1)
    GAIN_AH1_GH1=-par_1*(-par_2)/(1e3*2*pi)^2;
end
tilt_matrix(4+n,4+m)=(-par_1*(-par_2)/(1e3*2*pi)^2)/GAIN_AH1_GH1;
```

```
%%%%%%%%%%%%%%%%%%%%%%%%%%%%%%%%%%%%%%%%%%%%%%%%%%%%%%%%%%%%%%%%%%%%%%%%%%%%
%function that calculates the error of fitting the actuator to geophone
transfer function model to actual data.
Function
[FitError,AH_GH_TF_Model_freqresp]=Fit_AH_GH_TF_Model(par2,AH_GH_TF,freq)

%Actuator to geophone transfer function model, with zeros and poles given
from %spec sheet, and gain as adjustable parameter.
AH_GH_TF_Model=zpk([0,0],[-(1.65)-(6.24)*i,-(1.65)+(6.24)*i],-par2);
AH_GH_TF_Model_freqresp=squeeze(freqresp(AH_GH_TF_Model,2*pi*freq));

%Calculates the mean error. Selected frequency range to do the fit is 0.8-5Hz
%where the signal is not contaminated by tilt.
Error=100*abs(AH_GH_TF-AH_GH_TF_Model_freqresp)./abs(AH_GH_TF_Model_freqresp);
index=find(freq<=5&freq>=0.8);
FitError=mean(Error(index));

%function that calculates the error between the actuator to geophone transfer
%function model and actual data after the tilt component is removed.
function
[AveError,correction_filter_freqresp,AH_GH_TF_correct_freqresp]=design_correc
tion_filter_AH_GH2(par1,AH_GH_TF,par_2,AH_GH_TF_Model_freqresp,freq)

%Tilt component is the model plus extra two poles.
correction_filter=zpk([-1000*2*pi -1000*2*pi],[-(1.65)-(6.24)*i,-
(1.65)+(6.24)*i],-par1*(par_2)/(1e3*2*pi)^2);
correction_filter_freqresp=squeeze(freqresp(correction_filter,2*pi*freq));

AH_GH_TF_correct_freqresp=AH_GH_TF-correction_filter_freqresp;

%%Calculates the mean error after the correction. Selected frequency range is
%0.05-2Hz.
Error=100*abs(AH_GH_TF_correct_freqresp-
AH_GH_TF_Model_freqresp)./abs(AH_GH_TF_Model_freqresp);
index=find(freq<=2&freq>=0.05);
AveError=mean(Error(index));
```

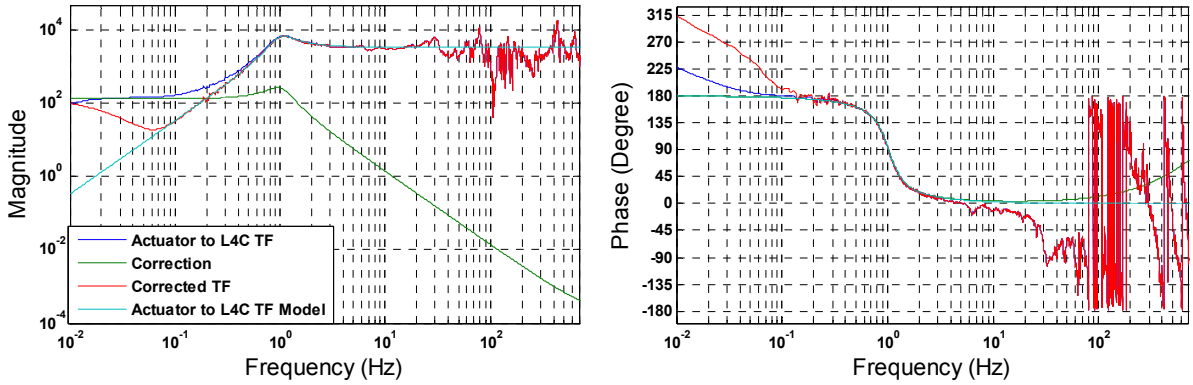

Figure B.1. Removing the tilt component in the HAM1 H1 actuator to H1 L-4C geophone transfer function at the sub-0.1Hz region. Below 0.01Hz the result starts to deviate from the model.

APPENDIX C: BAND-LIMITED RMS SEISMIC ISOLATION PERFORMANCE DURING THE S5 RUN

Table C.1. RGFs implemented on BSC tanks during S5 run.

Tank	Horizontal stack (Hz)	Vertical stack (Hz)	Suspension bounce (Hz)
BS	1,18, 2.12	2.7	12.575
ITMX	1.24, 2.16	2.7	11.865
ITMY	1.21, 2.16	2.7	11.89
ETMX	1.22, 2.15	2.7	12.01
ETMY	1.22, 2.14	2.7	12.03, 11.94

Table C.2 Rms noise suppression benefiting from the RGFs on BSC tanks during S5 run. The X, Y direction in BS chamber is omitted in this table since the test mass is suspended 45 degree from the beam direction and direct measurement was not performed. First numbers in each cell represents when HEPI system is turned on, second number in the parenthesis represents when HEPI is turned off, and the third number in the square bracket is the amount of reduction. Noise is reduced when the third number is greater than one (blue-colored).

* Measuring the factor of reduction in rms motion in the pendulum, side pendulum, pitch, and yaw modes, at frequency ranged between the half-maximum frequencies of bounce mode.

* * The two numbers pertain to the double resonant peaks mentioned in Section 3.2.2.

	Rms suppression						
Tank	1-3Hz transmission			Suspension bounce mode *			
	Ground to optics table		Ground to HEPI				
	X	Y	Z	Pendulum	Side pendulum	Pitch	Yaw
BS			0.08 (0.14) [1.78]	1	1	1.4	1.4
ITMX	0.83 (1.68) [2.02]	0.64 (1.63) [2.54]	0.06 (0.08) [1.38]	1.6	1	1.4	1.4
ITMY	0.20 (0.64) [3.20]	1.63 (4.94) [3.04]	0.02 (0.02) [1.11]	1.6	1.9	2	2
ETMX	0.57 (1.14) [2.02]	0.42 (0.97) [2.30]	0.14 (0.19) [1.34]	1	1	1	1
ETMY	0.43 (0.80) [1.86]	0.98 (1.80) [1.84]	0.04 (0.05) [1.19]	1.6, 1 * *	2.2, 2.5	2.4, 2.1	2.5, 2.1

Table C.3. Band-limited rms noise transmission from ground (sensed by STS-2 seismometer) to HEPI (sensed by L-4C geophones) in the X, Y, and Z direction. Also listed is the angular motion in the rotational DOFs measure by the HEPI geophones. On BSCs, noise is primarily reduced between 0.1-3Hz in the X, Y, and Z DOFs. In other DOFs and other bands, the results are rather mixed. Similar results on HAMs except the X and Y DOFs in the 0.1-0.3Hz band, due to the HAM tilting problem.

Tank	DOF	Frequency Band					
		0.03-0.1Hz	0.1-0.3Hz	0.3-1Hz	1-3Hz	3-10Hz	10-30Hz
BS	X	9.43(1.15)[0.12]	0.43(1.18)[2.72]	0.04(1.16)[27.78]	0.10(1.28)[12.20]	6.62(5.69)[0.86]	4.57(1.90)[0.42]
	Y	4.56(1.32)[0.29]	0.21(1.18)[5.55]	0.05(1.16)[21.47]	0.08(1.32)[16.26]	5.88(9.22)[1.57]	2.42(1.90)[0.78]
	Z	2.62(1.53)[0.58]	0.21(0.93)[4.48]	0.02(0.88)[45.32]	0.05(1.04)[21.01]	0.51(0.96)[1.87]	1.23(0.63)[0.52]
	RX	[1.25]	[1.63]	[3.32]	[8.20]	[1.68]	[0.77]
	RY	[1.13]	[6.85]	[10.72]	[5.29]	[2.01]	[0.86]
	RZ	[0.98]	[0.35]	[0.44]	[4.42]	[2.07]	[0.27]
ITMX	X	4.77(0.98)[0.21]	0.27(1.20)[4.43]	0.15(1.18)[8.04]	0.13(1.25)[9.42]	8.18(8.65)[1.06]	3.53(3.17)[0.90]
	Y	12.78(1.33)[0.10]	0.43(1.19)[2.75]	0.14(1.18)[8.56]	0.15(1.30)[8.50]	4.90(9.89)[2.02]	3.06(2.14)[0.70]
	Z	2.27(2.90)[1.28]	0.10(1.29)[13.42]	0.07(1.20)[18.10]	0.07(1.14)[17.03]	0.35(1.16)[3.26]	1.77(1.04)[0.59]
	RX	[1.05]	[0.84]	[0.58]	[1.36]	[1.49]	[0.86]
	RY	[1.05]	[0.78]	[0.71]	[1.56]	[1.47]	[1.13]
	RZ	[0.74]	[0.99]	[1.39]	[6.31]	[1.69]	[0.42]
ITMY	X	6.52(1.48)[0.23]	0.24(1.07)[4.50]	0.23(1.02)[4.37]	0.15(1.35)[9.19]	8.45(6.55)[0.78]	3.33(2.29)[0.69]
	Y	3.51(1.14)[0.33]	0.14(1.04)[7.59]	0.07(0.99)[14.07]	0.04(1.35)[36.14]	5.57(9.16)[1.65]	3.29(2.30)[0.70]
	Z	3.61(2.01)[0.56]	0.10(1.22)[12.25]	0.01(1.20)[95.27]	0.02(1.16)[52.64]	0.60(1.13)[1.89]	1.96(0.74)[0.38]
	RX	[1.34]	[1.89]	[2.07]	[1.48]	[1.48]	[0.96]
	RY	[0.97]	[1.83]	[2.59]	[1.89]	[1.25]	[1.29]
	RZ	[0.62]	[1.42]	[2.92]	[8.40]	[0.67]	[0.17]
ETMX	X	11.42(0.89)[0.08]	0.52(1.03)[1.97]	0.18(1.00)[5.45]	0.18(1.29)[7.33]	4.21(3.68)[0.88]	1.62(0.94)[0.58]
	Y	3.26(0.91)[0.28]	0.19(1.01)[5.41]	0.10(0.99)[9.95]	0.18(1.29)[7.21]	4.16(3.75)[0.90]	2.41(1.82)[0.75]
	Z	3.74(3.59)[0.96]	0.30(1.22)[4.09]	0.08(1.20)[15.47]	0.04(1.19)[30.72]	0.32(1.07)[3.34]	0.98(0.76)[0.77]
	RX	[1.03]	[0.65]	[0.59]	[1.14]	[1.25]	[4.09]
	RY	[0.99]	[0.62]	[0.53]	[1.06]	[1.33]	[7.09]
	RZ	[2.21]	[1.62]	[0.97]	[0.33]	[1.18]	[2.33]

Table C.3 Continued.

ETMY	X	2.86(1.01)[0.35]	0.15(1.12)[7.43]	0.07(1.09)[15.08]	0.12(1.34)[10.92]	5.78(5.00)[0.86]	1.63(1.39)[0.85]
	Y	9.09(0.97)[0.11]	0.39(1.08)[2.76]	0.09(1.06)[12.11]	0.24(1.26)[5.33]	4.08(3.62)[0.89]	1.59(0.95)[0.59]
	Z	1.34(1.30)[0.97]	0.25(1.28)[5.21]	0.04(1.25)[29.65]	0.04(1.18)[33.57]	0.46(1.22)[2.66]	2.20(1.13)[0.51]
	RX	[1.28]	[0.26]	[0.25]	[0.50]	[0.53]	[0.37]
	RY	[1.12]	[0.41]	[0.36]	[1.05]	[0.55]	[0.50]
	RZ	[1.00]	[0.89]	[1.94]	[4.00]	[0.53]	[0.32]
HAM1	X	84.76(0.58)[0.01]	3.42(1.11)[0.32]	0.25(1.09)[4.31]	0.24(1.19)[4.94]	2.71(1.27)[0.47]	3.48(2.18)[0.63]
	Y	27.87(2.62)[0.09]	1.57(1.05)[0.67]	0.50(1.03)[2.05]	0.97(1.08)[1.11]	3.06(0.97)[0.32]	1.78(1.27)[0.72]
	Z	2.26(1.40)[0.62]	0.05(1.20)[25.62]	0.07(1.17)[16.46]	1.33(0.95)[0.71]	1.47(0.44)[0.30]	0.82(0.62)[0.75]
	RX	[1.03]	[0.60]	[0.38]	[0.41]	[1.09]	[0.73]
	RY	[0.76]	[0.11]	[0.09]	[0.19]	[0.57]	[0.56]
	RZ	[0.60]	[0.18]	[0.53]	[0.72]	[0.54]	[0.49]
HAM2	X	72.87(0.70)[0.01]	2.77(0.94)[0.34]	0.20(0.87)[4.28]	0.21(1.23)[5.93]	2.62(1.25)[0.48]	2.88(2.07)[0.72]
	Y	23.98(1.05)[0.04]	0.98(0.89)[0.91]	0.41(0.82)[2.02]	0.99(1.16)[1.18]	2.77(1.07)[0.39]	1.73(1.33)[0.77]
	Z	1.82(1.60)[0.88]	0.09(1.25)[14.03]	0.08(1.19)[14.17]	1.28(1.10)[0.86]	1.22(0.70)[0.57]	0.91(0.75)[0.83]
	RX	[0.71]	[0.48]	[0.68]	[0.89]	[0.87]	[1.27]
	RY	[0.40]	[0.12]	[0.13]	[0.54]	[1.18]	[1.71]
	RZ	[0.05]	[0.38]	[1.72]	[2.97]	[0.64]	[0.68]
HAM3	X	83.76(0.88)[0.01]	2.94(1.17)[0.40]	0.18(1.10)[6.06]	0.48(1.20)[2.47]	2.52(1.39)[0.55]	4.32(1.68)[0.39]
	Y	33.38(1.16)[0.03]	1.45(1.10)[0.76]	0.55(1.04)[1.90]	0.77(1.16)[1.49]	2.44(1.16)[0.48]	3.05(1.68)[0.55]
	Z	0.96(1.61)[1.68]	0.11(1.29)[11.56]	0.07(1.26)[17.98]	0.56(1.09)[1.95]	2.22(0.79)[0.36]	1.03(0.78)[0.76]
	RX	[0.58]	[0.59]	[1.10]	[0.93]	[0.77]	[1.41]
	RY	[0.64]	[0.11]	[0.08]	[0.43]	[0.71]	[1.34]
	RZ	[0.06]	[0.61]	[4.13]	[2.35]	[0.52]	[0.73]
HAM4	X	23.40(0.94)[0.04]	1.16(0.93)[0.80]	0.54(0.89)[1.66]	0.89(1.17)[1.32]	3.45(1.44)[0.42]	3.08(2.27)[0.74]
	Y	52.20(1.03)[0.02]	2.94(1.00)[0.34]	0.27(0.95)[3.56]	0.13(1.23)[9.15]	3.00(1.16)[0.39]	2.88(2.27)[0.79]
	Z	1.16(1.51)[1.30]	0.06(1.18)[20.41]	0.05(1.15)[21.05]	0.53(1.14)[2.14]	1.89(0.92)[0.49]	1.05(0.96)[0.92]
	RX	[0.81]	[0.13]	[0.13]	[0.30]	[0.78]	[0.61]
	RY	[1.12]	[1.29]	[1.29]	[0.71]	[0.90]	[0.68]
	RZ	[0.18]	[0.45]	[1.35]	[2.29]	[0.46]	[0.69]

Table C.4. Band-limited rms noise transmission from ground (sensed by STS-2 seismometer) to the optics table (sensed by OSEM sensors). Numbers in each cell are arranged in the same fashion as in Table C.1. The X, Y direction in BS chamber is omitted in this table since the optic is suspended 45 degree from the beam direction and direct measurement was not performed.

Tank	DOF	Frequency Band					
		0.03-0.1Hz	0.1-0.3Hz	0.3-1Hz	1-3Hz	3-10Hz	10-30Hz
ITMX	X	7.04(1.43)[0.20]	0.40(1.71)[4.28]	0.31(4.23)[13.72]	0.89(22.25)[25.06]	6.64(7.99)[1.20]	3.79(4.54)[1.20]
	Y	7.80(1.62)[0.21]	0.63(2.49)[3.92]	5.02(52.60)[10.49]	1.93(53.51)[27.75]	5.79(10.30)[1.78]	2.82(2.52)[0.89]
ITMY	X	3.53(1.62)[0.46]	0.36(1.40)[3.88]	1.08(3.21)[2.98]	0.76(15.19)[20.08]	5.54(5.44)[0.98]	2.55(2.48)[0.97]
	Y	6.04(1.69)[0.28]	0.21(1.61)[7.47]	0.47(4.20)[8.92]	0.57(20.08)[35.22]	6.34(8.25)[1.30]	3.76(2.59)[0.69]
ETMX	X	7.94(1.41)[0.18]	0.38(1.49)[3.91]	0.49(4.29)[8.79]	0.74(17.29)[23.26]	3.36(3.40)[1.01]	1.37(0.95)[0.69]
	Y	2.82(0.50)[0.18]	0.13(0.73)[5.51]	0.09(1.62)[18.25]	0.31(8.11)[26.06]	1.79(1.87)[1.05]	1.34(0.95)[0.71]
ETMY	X	5.53(1.21)[0.22]	0.24(1.32)[5.46]	0.19(3.36)[18.09]	0.77(15.93)[20.68]	3.76(4.23)[1.13]	1.71(1.60)[0.94]
	Y	5.19(1.28)[0.25]	0.30(1.51)[5.08]	0.25(4.04)[16.22]	1.17(18.79)[16.13]	3.90(3.68)[0.95]	1.80(1.12)[0.62]
HAM1	X	5.69(1.06)[0.19]	0.18(1.49)[8.28]	0.17(1.69)[9.93]	1.17(11.22)[9.61]	3.25(1.56)[0.48]	2.09(0.92)[0.44]
	Y	9.75(3.89)[0.40]	0.38(1.58)[4.21]	0.13(1.67)[12.49]	3.27(14.39)[4.40]	4.70(1.47)[0.31]	2.36(1.03)[0.44]
HAM2	X	5.43(1.10)[0.20]	0.16(1.62)[9.82]	0.13(1.79)[13.89]	0.84(16.42)[19.54]	3.44(1.70)[0.49]	1.68(1.08)[0.65]
	Y	13.60(1.88)[0.14]	0.23(1.61)[7.04]	0.12(1.67)[14.44]	2.16(15.08)[6.99]	4.34(1.76)[0.41]	0.86(0.64)[0.75]
HAM3	X	15.70(1.67)[0.11]	0.31(1.96)[6.24]	0.81(3.81)[4.73]	2.88(10.57)[3.68]	4.44(2.23)[0.50]	2.17(1.44)[0.66]
	Y	8.14(1.63)[0.20]	0.20(1.34)[6.77]	0.11(2.03)[17.64]	0.94(8.65)[9.21]	2.70(1.38)[0.51]	1.59(1.77)[1.12]

Table C.5. Band-limited rms noise reduction in the pitch and yaw DOF, witness by the OSEM sensors and the optical levers. Numbers in each cell are arranged in the same fashion as in Table C.1.

Tank	DOF	Frequency Band					
		0.03-0.1Hz	0.1-0.3Hz	0.3-1Hz	1-3Hz	3-10Hz	10-30Hz
BS	PITCH	[0.40]	[2.19]	[20.44]	[50.87]	[1.61]	[1.14]
	YAW	[0.75]	[3.88]	[17.79]	[53.58]	[1.66]	[1.63]
	OPLEV PITCH	[0.10]	[2.28]	[5.23]	[6.12]	[3.22]	[1.12]
	OPLEV YAW	[0.22]	[2.76]	[4.30]	[6.24]	[4.11]	[1.08]
ITMX	PITCH	[0.97]	[4.70]	[7.76]	[20.49]	[1.98]	[1.57]
	YAW	[0.86]	[1.25]	[7.93]	[21.01]	[2.25]	[1.90]
	OPLEV PITCH	[0.55]	[4.57]	[7.49]	[22.21]	[1.02]	[1.00]
	OPLEV YAW	[0.35]	[2.05]	[7.71]	[12.37]	[1.05]	[0.93]
ITMY	PITCH	[0.59]	[6.19]	[6.52]	[26.21]	[1.35]	[1.86]
	YAW	[0.75]	[1.39]	[3.77]	[8.88]	[1.15]	[1.64]
	OPLEV PITCH	[1.15]	[4.09]	[6.52]	[9.18]	[1.05]	[0.96]
	OPLEV YAW	[0.18]	[0.63]	[3.16]	[7.02]	[1.40]	[1.10]
ETMX	PITCH	[0.59]	[5.39]	[5.02]	[32.33]	[1.72]	[0.71]
	YAW	[1.04]	[1.98]	[5.96]	[23.34]	[1.52]	[0.82]
	OPLEV PITCH	[1.37]	[3.68]	[5.81]	[19.81]	[0.91]	[0.97]
	OPLEV YAW	[0.06]	[1.90]	[6.17]	[18.06]	[0.48]	[0.83]
ETMY	PITCH	[0.84]	[2.07]	[6.01]	[20.21]	[0.82]	[0.82]
	YAW	[0.97]	[1.53]	[3.77]	[23.59]	[1.07]	[0.83]
	OPLEV PITCH	[1.16]	[4.41]	[11.20]	[24.60]	[4.82]	[3.40]
	OPLEV YAW	[0.87]	[2.49]	[6.52]	[27.97]	[3.17]	[1.20]
HAM1 MMT3	PITCH	[0.86]	[2.23]	[4.88]	[3.52]	[0.88]	[0.69]
	YAW	[1.25]	[1.97]	[2.39]	[2.51]	[0.96]	[0.71]
	OPLEV PITCH	[4.25]	[4.59]	[5.27]	[3.76]	[0.98]	[0.98]
	OPLEV YAW	[3.59]	[3.43]	[2.70]	[1.78]	[1.28]	[1.09]
HAM2 MMT2	PITCH	[0.28]	[0.97]	[1.19]	[5.82]	[0.90]	[0.80]
	YAW	[0.56]	[0.68]	[0.68]	[8.40]	[0.95]	[0.99]
	OPLEV PITCH	N/A	N/A	N/A	N/A	N/A	N/A
	OPLEV YAW	N/A	N/A	N/A	N/A	N/A	N/A
HAM3 RM	PITCH	[0.13]	[7.68]	[4.84]	[3.19]	[1.08]	[1.41]
	YAW	[0.83]	[1.42]	[4.80]	[3.20]	[1.01]	[0.87]
	OPLEV PITCH	[4.25]	[4.59]	[5.27]	[3.76]	[0.98]	[0.98]
	OPLEV YAW	[3.59]	[3.43]	[2.70]	[1.78]	[1.28]	[1.09]

VITA

Shyang Wen received the Bachelor of Science degree in physics from National Taiwan University in 1998. He decided to join LIGO after reading several special reports on gravitational wave research from *Scientific American* in the late 90's. Having a broad interest in physics, engineering, and biology, he hopes to continue pursuing these interests in the future.